C. elegans and CRISPR/Cas gene editing to study BAP1 cancer-related mutations and cisplatin chemoresistance

Carmen Martínez Fernández

TESI DOCTORAL UPF / 2020

Thesis supervisor

Dr. Julián Cerón Madrigal

Modeling Human Diseases in *C. elegans* Group.

Gene, Disease, and Therapy Program. IDIBELL.

Department of Experimental and Health Sciences

Para aquellos que aún perviven en el amor, la alegría y la perseverancia.

Acknowledgments

En primer lugar, quiero agradecer a mis padres, María del Mar y Fran, por darme vuestro amor y apoyo incondicional en todas las decisiones que he tomado en estos 27 años. Y a mi hermana, Helena, por tener el corazón más grande del planeta, a juego con sus labios y su frente, y tenerme siempre en él. No os lo digo, pero os quiero mucho.

A mi familia, porque sois la mejor que me ha podido tocar: a mi abuelo Paco, a mi abuela Carmen y mi a abuela Maru. A vosotros, Caki y Padrino, titos y titas. A mis primos, primitas y primito =)

Os quiero mucho a todos!

Mención especial a Julián, ¡lo hemos conseguido!. Gracias por el apoyo. Gracias por la motivación que desprendes, aunque a veces sea difícil de encontrar. Gracias también por echarme del país y por dejarme empezar a aprender contigo. No ha sido fácil, pero sin duda, volvería a repetir.

A Curro, Karinna, Xènia y Montse, porque fuisteis mis primeros labmates. Esos nunca se olvidan.

A la segunda ronda, David, Dimitri, LLuís y Jeremy. ¡Lo que une Cerón lab, no lo separará nae!

En especial, quería agradecer a XS, Mex y Dim. Habéis sido más que amigos, habéis sido la familia que no he tenido en el día a día en estos años. Creo que no podría haber tenido más suerte. Espero, nos reunamos de nuevo, porque seguro hay muchos Yunpengs deseando conocernos.

A vosotros, que nos hemos encontrado en el camino y también habéis llegado para quedaros: Leire, David, Nat, las del Rin Romántico…

A mis Malagueños en la distancia, o no tanto: a Ana (Montreal) y a Carlos (en la calle de al lado), a los Colegas Atómicos (Málaga-Berlín), Marina, Julia. Siempre es un placer volver y encontrarnos y saber que en el fondo nada ha cambiado. ¡Nos vemos en las bolas!

A Ale Moles, porque sin tu alegría no lo habría conseguido. Y a ti…te quiero al que más.

ABSTRACT

ABSTRACT

Model organisms and gene-editing strategies are fundamental to address a variety of scientific questions from basic science to biomedical research. Here, we reinforced the use of two powerful tools, the experimental system *Caenorhabditis elegans* and the CRISPR/Cas gene-editing technology, to model cancer-related mutations and investigate cisplatin-based chemoresistance.

We have established a model to study BAP1 cancer predisposition syndrome-related mutations in the BAP1 ortholog *ubh-4*. By exploring distinct *ubh-4* alleles, we have discovered a synthetic interaction between *ubh-4* and *rpn-9*, an essential regulatory subunit involved in proteasome assembly. Moreover, we suggest a cooperating role between these genes in the ubiquitin-mediated proteostasis at meiotic prophase.

In addition, we have exploited *C. elega*ns to study the toxicity of cisplatin-based therapies in different ways. First, by studying the impact of glucose and lipid metabolism on cisplatin toxicity. Then, we have described the harmful effect of cisplatin in mitochondrial functions. Finally, we have established a method to investigate the cisplatin-induced neurotoxicity by using an automated worm tracking system and discovered a protective role of dopamine.

RESUMEN

Los organismos modelo y las estrategias de edición genética son fundamentales para desentrañar incógnitas en ciencias de la vida, desde la investigación básica hasta investigación aplicada a la biomedicina. En este estudio, reafirmamos la importancia del uso de dos potentes herramientas, el sistema experimental *Caenorhabditis elegans* y la tecnología de edición genética CRISPR/Cas, para modelar mutaciones relacionadas con cáncer e investigar la quimiorresistencia al cisplatino.

Hemos modelado mutaciones asociadas al síndrome de predisposición tumoral BAP1, en *ubh-4*/BAP1. Explorando el efecto de distintos alelos mutantes de *ubh-4*, hemos descubierto una interacción sintética entre *ubh-4* y *rpn-9*, el cual codifica para una subunidad reguladora esencial para el ensamblaje del proteasoma. Además, proponemos que la cooperación funcional de dichos genes está implicada en la degradación de proteínas mediada por el sistema ubiquitina-proteasoma durante la profase meiótica.

También hemos investigado la respuesta generada por la terapia con cisplatino en *C. elegans*. Por una parte, hemos demostrado que la toxicidad inducida por el cisplatino puede modularse alterando el metabolismo glucídico y lipídico. Por otro lado, hemos observado que esta droga genera disfunción mitocondrial. Finalmente, mediante un sistema automatizado, hemos puesto a punto un método para evaluar el efecto neurotóxico del cisplatino en el nemátodo y hemos encontrado que la dopamina posee un efecto protector.

PREFACE

Precision medicine is particularly relevant in cancer. Thus, the description of individuals' genetic landscape is essential to unravel cancer susceptibility and propose personalized anticancer therapies. Particularly, we have focused on BAP1 cancer predisposition syndrome, and chemoresistance to cisplatin-based therapies.

Caenorhabditis elegans has been successfully used as an experimental system since the 1970s, providing several advantages over other models. Here, we have taken advantage of its power as a genetic tool, together with CRISPR/Cas technology, to generate several transgenic lines, including cancer-related mutants and endogenous reporters. Additionally, *C. elegans* is a well-established system to investigate neuromodulatory pathways *in vivo*, and the effect of genotoxic drugs in a pluricellular context.

Based on our expertise in *C. elegans* gene editing by CRISPR/Cas, we mimicked missense mutations related with BAP1 cancer predisposition syndrome and, particularly, with malignant pleural mesothelioma. Thanks to *C. elegans* hermaphroditism and the viability of BAP1-related alleles, we were able to analyze the sub-cellular implications of these mutations in an isogenic population. Moreover, using RNAi, partial inactivation of functionally related genes revealed a possible therapeutic target for BAP1 affected tumors.

Our lab has previously employed *C. elegans* to understand the cytotoxicity induced by cisplatin. Here, we have further

exploited this model using semi-automated platforms such as Seahorse, providing information about *C. elegans* respirometry, and the Tierpsy Tracker automated tracking system for evaluating behavioral features. The latter was kindly provided by André Brown (Institute of Clinical Sciences, Imperial College London). Conveniently for neurotoxic studies, we generated a set of dopamine signaling-related mutants, which resulted in a system for studying cisplatin-induced neuronal damage. All the above will help us to answer fundamental questions regarding cisplatin therapeutic use.

During my PhD, I have been funded by the European Cooperation in Sciences and Technology (COST) Mission with a GENIE Short Term Mission (STSM) grant to perform an internship at Carina Holmberg's laboratory at Medicum, University of Helsinki (Helsinki, Finland) and by the Deutscher Akademischer Austauschdienst (DAAD) for a 6-months internship Short-Term Grant at Sebastian Honnen's laboratory at Toxicology Institute, Heinrich Heine Universität (HHU) (Düsseldorf, Germany).

KEY WORDS

C. elegans

CRISPR/Cas

ubh-4

rpn-9

Ubiquitin Proteasome system

RNA interference

Meiosis

Cisplatin

Glucose

sbp-1

Mitochondrial dysfunction

Catechol-*O*-methyltransferase

Dopamine

Neurotoxicity

Behavior

TABLE OF CONTENTS

LIST OF FIGURES AND TABLES

FIGURES

TABLES

INTRODUCTION

1. Animal models in biomedical research

Animals models have been used to address a variety of scientific questions, from basic science to the development of novel vaccines or therapies, throughout human history. The earliest written records of animal experimentation date to 2000 BC when Babylonians and Assyrians documented surgery and medications for humans and animals. It was only in 304 BC, in the ancient Greece, when animal experimentation led to a scientific demonstration (Maurer and Quimby, 2015).

Conceptually, a model in biomedical research is a system in which a homolog or analog process to the subject being modelled happens or can be mimicked, generally, a human process. Animal models represent only a fraction, but there are many types of models: *in vitro* assays, mathematical models, or computer simulations. It is important to note that a model serves as a substitute, and it is not necessarily identical to the subject of interest. Thus, not only vertebrate models are useful in human research, soil and marine invertebrates or insects have contributed to achieve important discoveries in genetics and molecular biology. As a representative example in 2002, the Nobel Prize in Physiology or Medicine was awarded jointly to Sydney Brenner, H. Robert Horvitz and John E. Sulston for their discoveries concerning genetic regulation of organ development and programmed cell death by establishing and using the nematode *Caenorhabditis elegans* as an experimental model system.

Many of the most common human diseases such as cancer or obesity are complex, often polygenic, with multiple interacting environmental influences. These types of pathologies require the use of many-to-many modeling, which results from the analysis of a process in an organism or organisms where each component of that process is evaluated at several hierarchical levels, e.g., system, organ, tissue, cell, and subcellular levels. Many-to-many modeling requires joining the strength of multiple model systems. In this context, high-throughput techniques such as sequencing, transcriptomics and proteomics have facilitated this process (Barré-Sinoussi and Montagutelli, 2015; Maurer and Quimby, 2015).

2. Platinum-based compounds as first-line cancer treatment

Cancer is a generic term for a large group of diseases and the leading cause of death worldwide with 9.8 million cases in 2018. Among the most common cancers, it has been highlighted lung and breast cancer (with 2.09 million cases), and colorectal cancer (with 1.80 million) cases in 2018, according to the World Health Organization. Cancer-related deaths are rising due to increased life expectancy, overweight and incorporation of exogenous toxic substances (Perera, 1997). Early detection, including early diagnosis and screening, is essential to reduce cancer mortality in order to identify individuals with abnormalities suggestive of specific cancer who have not developed any symptoms.

Cis-Diammine Dichloride Platinum (CDDP), also known as cisplatin, is the most commonly drug used in cancer treatment followed by its analogs oxaliplatin and carboplatin (Amable, 2016). Cisplatin is widely prescribed as a first-line treatment including testicular, ovarian, cervical, bladder, head and neck, and small cell lung cancers (SCLCs) (Chen and Kuo, 2010). In addition, CDDP is the platinum derivative with the highest therapeutic efficacy in a series of solid tumors. The most remarkable example is testicular cancer in which cisplatin provides the cure for over 95% of the patients (Jemal et al., 2008; Maluccio et al., 2007). Cisplatin undergoes equation when entering the cell, becoming more reactive to interact with cellular targets: DNA, RNA and proteins. Thus, cisplatin acts both in the nucleus and the cytoplasm.

Among the cisplatin cytotoxic consequences, the most prevalent are the formation of DNA (mono-, intrastrand- and interstrand-) cisplatin-adducts and the production of reactive oxygen species leading to homeostasis imbalance and ultimately, provoking apoptosis (Amable, 2016; Kelland, 2007; Wang and Lippard, 2005). There are two problems associated with cisplatin usage in the clinic: (1) Toxic side-effects such as nephrotoxicity, and neurotoxicity (hearing loss and peripheral neuropathy), the last being the most significant dose-limiting toxic effect, and (2) Resistance to therapy, being the major obstacle the chemoresistance acquired by tumors during cycles of therapy (Kelland, 2007; Wang and Lippard, 2005).

3. *Caenorhabditis elegans* to study cisplatin response and mimic human cancer mutations

3.1. *C. elegans* biology

Caenorhabditis elegans is a soil nematode introduced as a model organism for the first time by Sydney Brenner to study development and neurobiology (Brenner, 1974). *C. elegans* present a series of advantages over *in vitro* or cellular models. First, it is easy to maintain in the laboratory, generally in solid media, on a diet of *Escherichia coli.* Second, this nematode presents a short generation time, that is temperature dependent, from egg to adult worm within 3 days at 22ºC (**Figure 1**). A single self-fertilizing hermaphrodite can produce about 300 descendants, allowing a large-scale production of animals daily. Third, its small size (around 1 mm adult animal) facilitates the performance of assays including big populations, different genetic backgrounds, and many conditions at a time in multi-well plates without requiring ample spaces neither wasting big amounts of reagent or drug. Fourth, is a sophisticated multicellular animal and thanks of its transparent body, we can optically distinguish cell types and tissue structures, and also processes at cellular level using fluorescent markers. Fifth, it is a sophisticated multicellular animal: although the adult hermaphrodite has only 959 somatic cells, these form many different organs and tissues including muscle, hypodermis (skin), intestine, reproductive system, glands, and a nervous system containing 302 neurons.

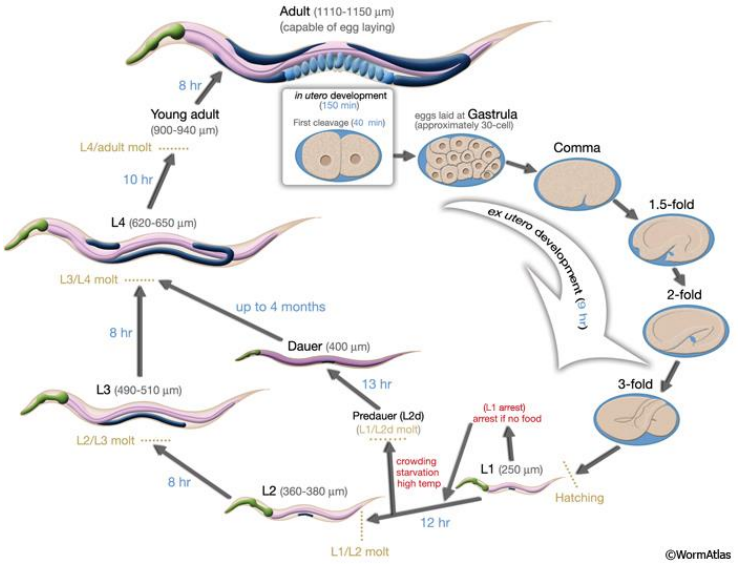

Figure 1: Life cycle of *C. elegans* hermaphrodite at 22ºC. The different developmental stages from fertilization to adulthood are represented. The numbers in blue depict the duration of each phase, and the worm length at each stage is indicated in micrometers (µm). Reproduced from WormAtlas.

3.2. *C. elegans* relevance as a model organism

C. elegans presents several features that make it a powerful tool for the pharmaceutical industry and human diseases studies:

3.2.1. Genetic conservation between human and *C.elegans*

C. elegans homologs have been identified for 60-80% of human genes (Kuwabara and O'Neil, 2001; Lai et al., 2000; O'Reilly et al., 2014; Sonnhammer and Durbin, 1997). Thus, modeling human diseases and discovering new drug targets is often possible in the nematode. Despite high sequence

conservation between human and *C. elegans* gene families, it is not always is possible to assign orthologs between both species due to functional divergence during evolution. If a gene duplicated after two species diverged during evolution, then more than one orthologue exists in at least one of the two species; these are called inparalogues. Inparalogues have one-to-many or many-to-many relationships and are grouped into orthologue clusters (Remm et al., 2001). The functional role of the original ancestor gene is often split up among inparalogues. For example: both pro-apoptotic and pro-survival functions provided by human BAX and BLC2 proteins respectively, are contained in *C. elegans* CED-9 (Hengartner and Horvitz, 1994; Jagasia et al., 2005).

3.2.2. The complete *C. elegans* neuronal connectome has been explored

The nervous system is by far the most complex one of *C. elegans*, with 302 neurons plus 56 glial cells and about 8800 synapses (6400 chemical, 1500 neuro-muscular synapses and 900 gap-junctions). Particularly important is that single neuron can be tracked and its functionality can be investigated in the living animal (White JG, Southgate E, Thomson JN, Brenner S 1986). Moreover, many human neurotransmitter and neuromodulator signaling pathways are conserved in *C. elegans.* Therefore, studies of neurodegenerative diseases and neuronal signaling in the human brain are possible using this model.

3.2.3. Powerful genetic tool

(i) Forward genetics

Genetics analyses were broadly used in the last century. In classical or forward genetics, the genome of an organism is randomly mutagenized. Mutants with the desired phenotype are collected and used to identify and characterize genes involved in the process of interest (Kaletta and Hengartner, 2006).

(ii) Reverse genetics

Nowadays, new genome-editing methods in model organisms are evolving at an extraordinary speed. That is the case of CRISPR technology, which allows genetic engineering of a target genes.

Genome editing by CRISPR/Cas

Clustered regularly interspaced short palindromic repeats (CRISPR) are repetitive elements that were initially identified in bacterial and archaeal genomes (Ishino et al., 1987; Mojica et al., 1993). This technology has had a revolutionary impact in life sciences and is still transforming genome editing (Makarova et al., 2015; Mojica and Montoliu, 2016; Mojica et al., 2005). In fact, Emmanuelle Charpentier and Jennifer A. Doudna have been awarded the Nobel Prize in Chemistry 2020 for the discovery and application tool of “CRISPR/Cas9 scissors” to life sciences. CRISPR elements are part of an

adaptative immune system against invading viruses and conjugating plasmids (Bolotin et al., 2005; Mojica et al., 2005; Pourcel et al., 2005). Six types of CRISPR systems has been identified (Makarova et al., 2015; Shmakov et al., 2017). In the case of type II (**Figure 2**), foreign DNA sequences are incorporated into the microorganism genome in the adaptation phase. These sequences are expressed in form of small mature CRISPR RNAs (crRNAs). crRNAs are combined with a trans-activating RNA (tracrRNA) to guide the host CRISPR-associated endonucleases (Cas9 in type II system) towards foreign DNA which will be degraded. The use of CRISPR/Cas9 has expanded from human and mouse cell lines (Cong et al., 2013; Mali et al., 2013) to many organism, including *C. elegans* (Friedland et al., 2013).

(iii) RNA interference (RNAi)

RNAi is a phenomenon discovered in *C. elegans* (Fire et al., 1998) which was extremely relevant in biology research and awarded to the investigators the Nobel Prize in Physiology or Medicine in 2006. They revealed that double stranded RNA (dsRNA) molecules could inhibit the expression of homologous genes in a specific manner. RNAi-mediated knockdown of genes in *C. elegans* can be reached by (1) directly injecting dsRNA), (2) by soaking animals in a solution containing dsRNA, or (3) by feeding the nematode with bacteria that produce dsRNA. A brief overview of RNAi pathway is illustrated in **Figure 3**.

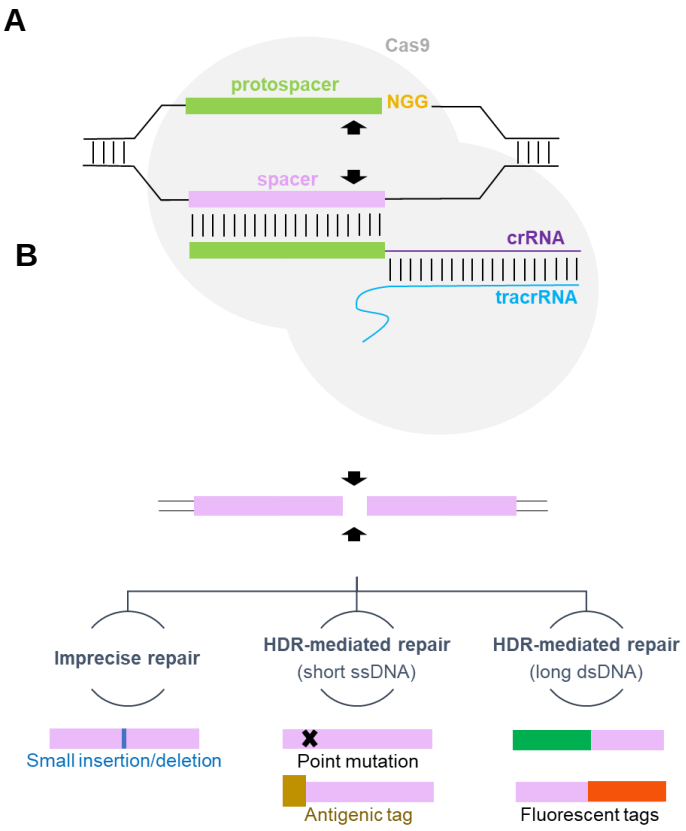

Figure 2: CRISPR/Cas9 reagents and possible outcomes depending on the DSB repair mechanism. A. Schematic representation of an RNP complex (Cas9 + crRNA + tracrRNA) bound to a target gene. Vertical black lines represent base pairs. Black arrows indicate Cas9 cut sites. The PAM sequence (NGG) is colored in yellow. **B.** Possible repair outcomes of a Cas9-induced DSB. Imprecise repair occurs if no repair template is supplied, resulting in small insertions or deletions that often change the reading frame. Short ssDNA repair templates can be used to introduce point mutations or short antigenic tags. Long dsDNA molecules can be used to introduce fluorescent tags at the 5' or the 3' end of a gene.

There are two genome-wide RNAi feeding libraries consisting of thousands of bacterial clones that produce dsRNAs against most *C. elegans* genes and were built using different approaches. One library was constructed at Julie Ahringer's lab by cloning 500–2,500-bp long genomic DNA fragments containing exons and introns (Kamath et al., 2003). The other library was generated at Marc Vidal's lab by cloning full-length open reading frames (ORFs) from cDNA libraries, and thus it is also known as the ORFeome-RNAi library (Rual et al., 2004).

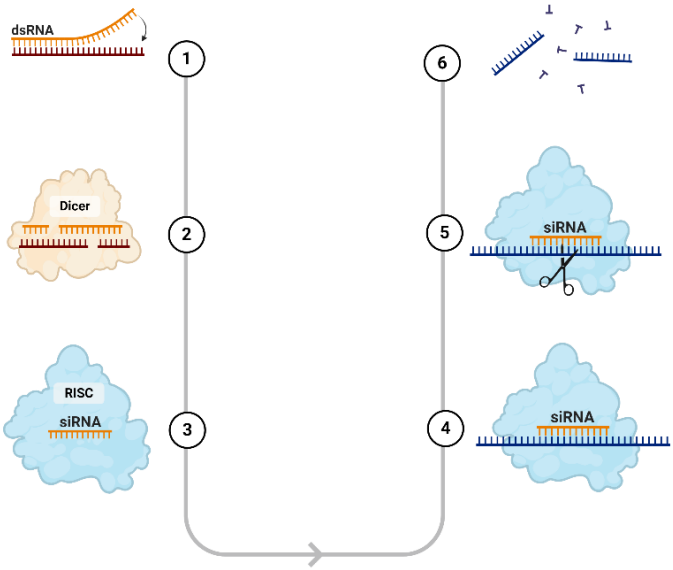

Figure 3: Schematic representation of gene silencing by RNAi. Once exogenous dsRNAs with a minimal fragment length (100 base pairs) are formed or internalized in the cells (**1**) they enter the conserved RNAi pathway. In the cytoplasm of the cell, dsRNA attaches to the enzyme Dicer digesting the dsRNA to smaller fragments, typically 21-23 nucleotides (**2**). The antisense strand is transferred and associates onto the RISC protein (**3**). This enables the homologous mRNA transcript to bind the antisense strand (**4**). This results in cleavage (**5**) and degradation of the mRNA (**6**)

thus suppressing protein synthesis (Fire et al., 1998). Created with Biorender.com.

4. Overview of the ubiquitin-proteasome system

Proteolysis is the enzymatic process by which proteins are broken down into smaller polypeptides or amino acids through the hydrolysis of peptide bonds. However, this degradation can also occur through non-enzymatic methods such as by the action of mineral acids or heat. Proteolysis has multiples roles on the cellular maintenance such as providing amino acids to the cell (Silk, 1974) or prevent the accumulation of abnormal or misfolded proteins (De Strooper, 2010). The ubiquitin-proteasome system (UPS) is the major intracellular protein degradation system. The UPS consists of many factors that include E3 ubiquitin ligases, ubiquitin hydrolases, ubiquitin and ubiquitin-like molecules, and proteasomes. The UPS acts both in the nucleus and cytoplasm, and its intracellular distribution depends on the cell type and tissue.

Besides its proteolytic activity, which provides a tight control of the intracellular protein degradation and turnover, the proteasome complex also possesses: ATPase/helicase activity, important for both unfolding the target protein and chromatin remodeling; RNAse activity, which may help to control splicing and mRNA levels; and deubiquitinase activity, required for clearing ubiquitin from the target protein for its subsequent degradation (Grigoreva et al. 2015). Proteasome is implicated in multiple cellular pathways such as cell cycle

(regulating cyclin levels), apoptosis (tightly regulating caspase amount) and differentiation and development (controlling gene expression and degrading cell cycle regulatory proteins) (Konstantinova et al., 2008). The function of the proteasome in the cell is very complex, and modulation of proteasome activity by regulating proteasome composition and abundance is fundamental for proper cell functioning and viability (Rousseau and Bertolotti, 2018). Furthermore, cells adjust proteasome-mediated degradation to their needs by regulating proteasome abundance through the coordinated expression of proteasome subunits and assembly chaperones. Central to the regulation of proteasome assembly is TOR complex 1 (TORC1), which is a key regulator of cell growth and stress. Proteasome assembly and the regulation of proteasomal degradation are integrated with cellular physiology (Rousseau and Bertolotti, 2018). Misregulation of proteasome function contributes to human diseases such as cancer or neurodegenerative disorders.

5. UPS in *C. elegans*

5.1. Structural subunits of the proteasome complex

The ubiquitin-proteasome system is the major proteolytic system in the cell carrying out the selective and efficient hydrolysis of normal or damaged proteins. As I mentioned above, its function is essential for the cellular maintenance,

controlling the levels of key regulatory proteins, and for cellular viability. Thus, these complexes are subjected to a tightly organized regulation, mainly, through post-translational modifications. Since the proteasome genes are evolutionarily conserved, the role of many of them has been dissected in model organisms, including *Caenorhabditis elegans*. Below, I describe the structural organization of *C. elegans* proteasome complexes and summarize the role of the major players in the UPS pathway, highlighting those relevant in this study.

5.1.1. 20S proteasome (proteasome core)

In all eukaryotes and in some prokaryotes, 20S proteasomes are large protein complexes of approximately 700 kDa. A 20S proteasome is a cylindrical structure containing four stacked rings, named 2α (formed by α-type subunits 1-7, located in the outer part) and 2β (formed by β-type subunits 1-7, located in the inner part). Each ring is made by seven different protein subunits conforming a central pore. A linear representation of the 20S final structure is shown in **Figure 4**. There are located three proteolytic active sites in the interior surface of each inner ring. As these sites are found on the interior surfaces, the protein will be entering the central pore through the “gate” formed by the two outer rings, prior to be degraded (Marshall and Vierstra 2019; Papaevgeniou and Chondrogianni 2014; Tanaka 2009).

i) α-Type subunits in C. elegans

α-Type proteasomal subunits set up the two outer rings of the core and have structural and regulatory roles. They conform a gate by which the access of the substrate is regulated through allosteric interactions. Significant homology has been found throughout the seven *C. elegans* α-type subunits compare to the human ones (**Results, Table 3**). These subunits have an essential role for the core and loss of activity in α-type subunit causes detrimental effects in humans and *C. elegans* (DeRenzo et al., 2003; Xu et al., 2003).

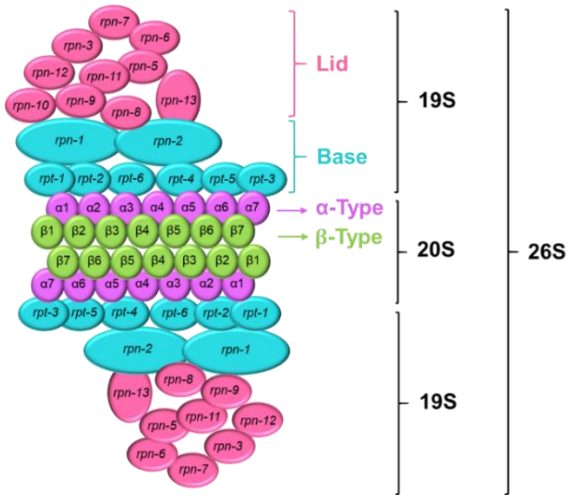

Figure 4: Schematic model of the *C. elegans* 26S proteasome. 26S complex is formed by two regulatory particles 19S and one core particle 20S. Structure subunit forms are represented by colors and detailed subunit proteins by coding gene name. Rings conforming the 20S core and 19S structure are represented linearly. Adapted from KEGG database (Kanehisa, 2019; Kanehisa and Goto, 2000; Kanehisa et al., 2019).

ii) β-Type subunits in C. elegans

β-Type subunits perform the degradation of polypeptides and proteins since they enclose the proteolytic part of the 20S core particle. β1, β2 and β5 subunits possess three different proteolytic activities: caspase-like, trypsin-like and chymotrypsin-like activity, respectively. β-Type subunits in *C. elegans* also present high similarity with the human ones (**Results**, **Table 3**) and depletion of β-type subunits leads to mild and lethal effects in the nematode (Green et al., 2011; Simmer et al., 2003).

5.1.2. 19S (regulatory complex)

The 19S carries out the recognition of the ubiquitinated substrates for subsequent deubiquitination and translocation into the catalytic core complex to be degraded into peptides. This regulatory particle presents several transiently associated enzymes that catalyze the deubiquitination of the targeted substrate. The 19S complex is divided into a ring-like base, and a lid-like structure. These two structures are linked through proteasome regulatory particles, Non-ATPase 10 and 13 (*rpn-10* and *rpn-13*), with the participation of *rpn-2* (Marshall and Vierstra 2019; Papaevgeniou and Chondrogianni 2014; Tanaka 2009). The base- and lid-forming *C. elegans* subunits, together with its human orthologs are detailed in **Results**, **Table 3** and their final structure schematized in **Figure 4**.

i) 19S base complex

The role of the 19S base complex consists in (1) the recognition of the ubiquitinated proteins, (2) the ATP-dependent unfolding of the substrates, (3) the allosteric-dependent opening of the 20S core gate and finally, (4) the translocation of the protein inside the 20S catalytic particle. Both ATPases and non-ATPases in this complex have important roles for *C. elegans* development and viability. Non-ATPases subunits have been shown to be involved in germline development, and some are essential for proper animal growth (Green et al., 2011).

ii) 19S lid complex

Non-ATPase subunits from the 19S lid subcomplex play critical roles not only in the deubiquitination and degradation of the substrates, but also in the assembly and maintenance of the structural integrity of the proteasomal machinery (Isono et al., 2004; Yen et al., 2003). All of them share a PCI (C-terminal Proteasome-COP9/CSN-Initiation factor) domain, which serves as a scaffold for the protein-protein interaction. No enzymatic activity has been described for these non-ATPases subunits, except for *rpn-11* which is a proteasome intrinsic deubiquitinating enzyme. ***rpn-9*** part of the lid complex and, despite of being a non-essential subunit for cell viability in yeast, is crucial for proteasome assembly, protein homeostasis

and proper *C. elegans* development (Hu et al., 2015a; Takeuchi et al., 1999; Wang et al., 2010).

5.1.3. 26S proteasome

The 26S proteasome consists of one 20S proteolytic core and two 19S regulatory complexes attached to the α-rings at both ends of the 20S complex (**Figure 4**). Thus, the 26S proteasome is a 2 MDa molecular machine composed by more than 30 different subunits. This large protease complex is ubiquitous in eukaryotic cells and plays a central role in cellular proteostasis. The assembly of the 20S, 19S and 26S structures is a very complex multi-step process and is highly regulated in eukaryotic cells. It involves a set of proteasome-specific chaperones, modulators and other intermediates but the entire process is not fully understood (Marshall and Vierstra 2019; Papaevgeniou and Chondrogianni 2014; Tanaka 2009).

5.2. UPS-associated molecules

5.2.1 Ubiquitin (Ub) molecules

Ubiquitin molecules are small proteins of about 70 aminoacids followed by protruding C-terminal glycine residues and are highly conserved in eukaryotes. The ubiquitin molecules are attached to the target protein through an isopeptidase linkage between its glycine and the cysteine, serine, threonine or, predominantly, lysine residues at the N-terminal of the target protein. *C. elegans* possesses polyubiquitin loci (*ubq-1* and

ubq-2), which produce polyubiquitin proteins that are post-translationally cleaved by ubiquitin C-terminal hydrolases. Once cleaved, Ub can be used for protein targeting. Ubiquitin molecules, existing as a free monomer or being part of a complex, are distributed ubiquitously throughout the cell (Papaevgeniou and Chondrogianni, 2014).

5.2.2. E1-E3 ubiquitin ligases

E1-E3 ligase enzymes act coordinately in a multistep process to attach covalently ubiquitin molecules to the protein to be degraded. First, E1, in an ATP-dependent manner, forms the reactive thioester intermediate E1-Ub by adenylation. Second, the activated ubiquitin is transferred to a ubiquitin conjugating E2 enzyme by transthiolation. Meanwhile, a specific ubiquitin-protein ligase (E3) has recruited the target protein and mediates the transfer of the activated ubiquitin from the E2 enzyme to the substrate. This ubiquitination cycle is successively repeated, thus producing polyubiquitinating chains on the target protein. It has been shown that at least four ubiquitin residues are needed for efficient recognition and processing by the 26S proteasome (Papaevgeniou and Chondrogianni, 2014).

5.2.3. Deubiquitinases (DUBs)

Ubiquitination is a reversible post-translational modification with key roles in various signal transduction cascades and in determining protein stability. DUBs are a large group of proteases that cleave ubiquitin from protein substrates and other molecules, and their function has major effects on the regulation of protein half-life and quality. DUBs have been implicated in important pathways controlling cell growth, differentiation, development, and transcriptional regulation (Reyes-Turcu et al., 2009). DUBs remove the peptide or isopeptide bond between the ubiquitin or ubiquitin chain and the protein substrate.

There are nearly 100 genes encoding deubiquitinating enzymes in humans, and 45 genes in *C. elegans*. DUBs can be classified in 2 classes based on its catalytic core —cysteine proteases and metalloproteases— and 5 subclasses (**Figure 4** and **Results**, **Table 3**). One of these subclasses is ubiquitin C-terminal hydrolases (UCHs), which present relatively small sizes. UCHs catalyze the removal of peptides and small molecules from the C-terminus of ubiquitin, and some of them present additional enzymatic activities (Fang et al., 2010). Human and *C. elegans* UCHs are listed in **Figure 5**.

BRCA1-associated protein 1 (BAP1) and ubiquitin carboxyl-terminal hydrolase 37 (Uch37), also known as UCHL5, are DUBs from the same peptidase family that share a high degree of sequence similarity not only in their catalytic ubiquitin

carboxy-terminal hydrolase domain (UCH) but also in an additional conserved carboxy-terminal region, previously called the Uch37-like domain (ULD) (**Figure 6**) (Misaghi et al., 2009; Yao et al., 2006). UCHL5 and BAP1 are the most studied UCHs because of their relevance in human diseases.

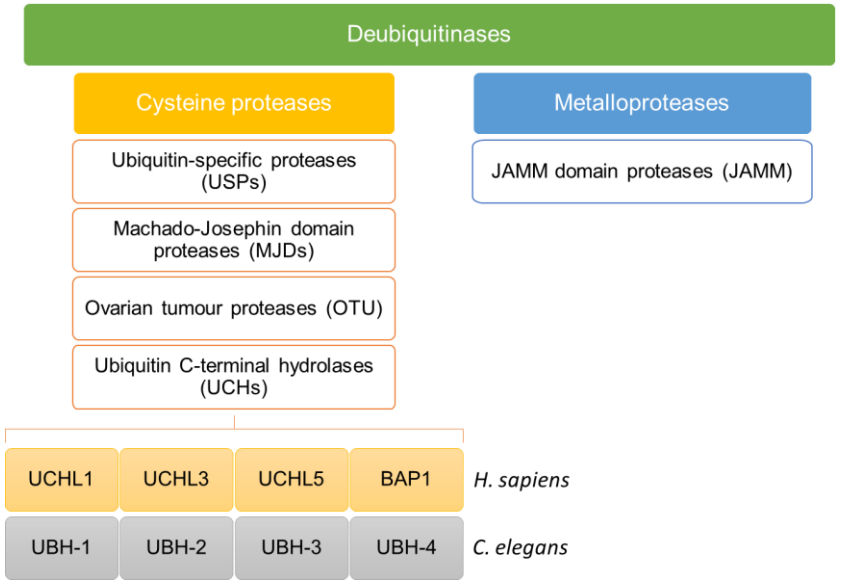

Figure 5: Schematic representation of DUB classes and subclasses. Deubiquitinating enzymes are classified in two classes (cysteine proteases and metalloproteases) and 5 subclasses (USPs, MJDs, OUT, UCH and JAMM). Four UCHs members in H. sapiens and C elegans are shown at the bottom of the Figure.

Figure 6: Schematic representation of BAP1 and UCHL5 protein length and domains. Bars represent coding sequences of both proteins and legend indicates different predicted motifs and domains, classified by colors. Graphical representation was made using ProteinPaint (Zhou et al., 2015).

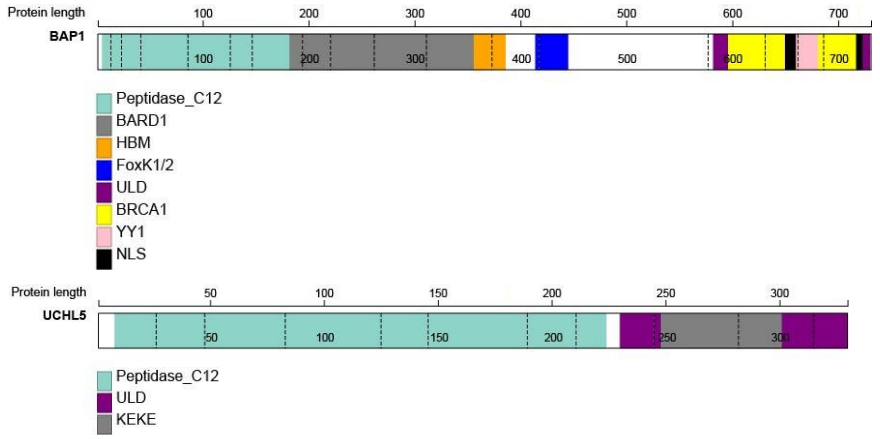

i) UCHL5

Human UCHL5 is one of the DUB enzymes transiently associated to the 26S proteasome. Like BAP1, it has an N-terminal UCH domain and an unusual C-terminal helical extension, called ULD (Misaghi et al., 2009). The ULD domain could mediate protein-protein interactions, including higher-order homo-oligomerization (Burgie et al., 2012; Jiao et al., 2014), and was proposed to act as an autoinhibitory module (Yao et al. 2006). UCHL5 catalytic activity requires its incorporation to the 19S particle, through the interaction between the UCHL5 C-terminal tail and the Rpn13 N-terminal domain. Otherwise, UCHL5 C-terminal tail inhibits its catalytic domain (Fang et al., 2010; Sahtoe et al., 2015). Recent studies have demonstrated that nuclear UCHL5 is also associated, in an inactivated form, to the human Ino80 chromatin-remodeling complex (hINO80). Therefore, association to the regulatory particle 19S is again required for UCHL5 activation. Thus, it is assumed that in the nucleus, UCHL5 is linked to both

proteasome and hINO80 complexes (Yao et al., 2008; Zediak and Berger, 2008) and possibly is involved in nucleosome remodeling by hINO80 (Fang et al., 2010). The closest ortholog to UCHL5 in *C. elegans* is UBH-4 and has been proposed to be involved in the UPS pathway (Matilainen et al., 2013).

ii) BAP1

BAP1 is a nuclear DUB with an N-terminal UCH domain and a C-terminal UDL domain, containing two predicted nuclear localization signals (NLSs). Both UCH and NLSs are considered essential for BAP1 function. Despite being a BRCA1-associated protein, BAP1 does not function in the deubiquitination of BRCA1 (Mallery 2002). BAP1 ubiquitin-interacting residues have been identified (Bhattacharya et al., 2015; Hanpude et al., 2017), although still not all its deubiquitinating targets are known. BAP1 is involved in numerous cellular processes including stem cell pluripotency, DNA damage response and replication, cell cycle progression, histone modification, gluconeogenesis, and myeloid transformation (Balasubramani et al., 2015; Baughman et al., 2016; Dey et al., 2012; Jensen et al., 1998; Ruan et al., 2012; Zarrizi et al., 2014). BAP1 regulates expression of various target genes by deubiquitinating transcription-related proteins such as ASXL1, ASXL2 or HCF-1 (Dey et al., 2012).

6. The role of UPS in disease

6.1. Overview of the proteasome as a therapeutic target

6.1.1. Neurodegenerative disorders and ageing

Given that the proteasome controls many cellular processes, it is not surprising that proteasome misregulation leads to the onset of diverse diseases. Dysfunction of the proteasome contributes to misfolded, mutated, or damaged protein accumulation which can be deleterious to the cell. One of the hallmarks of neurodegenerative diseases is the accumulation of proteins with abnormal conformation in soluble aggregates (Chondrogianni et al., 2014; Marshall et al., 2015). This proteasomal decline in neutralized aggregation-prone proteins is also a sign associated with ageing (Vilchez et al., 2014). Since such aggregates are sometimes too large for ubiquitin-mediated protein degradation, one of the proposed therapies is to increase proteolytic proteasome activity prior to their formation.

6.1.2. Cancer

Age is also one of the greatest risk factors for cancer accumulation of genomic mutations occurs during ageing (Manasanch and Orlowski, 2017). Mutations may change the levels of proteins or protein complexes in turn, causing the accumulation of misfolded or overproduced proteins. This

protein excess probably generates upregulation of proteasome production and assembly, explaining why cancer cells are usually addicted to high levels of proteasome complexes. Exploiting that idea, recent advances in the use of proteasome inhibitors in cancer therapy have been made (Grigoreva et al. 2015; Manasanch and Orlowski 2017).

Although proteasome inhibitors have shown benefits, resistance to the treatment arises in some cases, particularly when the drug targets the 19S regulatory particle. It is hypothesized that the cell may try to adjust the proteasome abundance when it is inhibited, so cells adapt to the reduction of 19S complex activity by increasing proteasome genes expression (Acosta-Alvear et al., 2015). Other studies have shown that mutations in oncogenes, together with additional factors, can activate the transcription of proteasome genes, is the case with, p53 missense mutant in cooperation with NRF2 (Walerych et al., 2016).

These findings highlight the importance of properly understanding the regulation of proteasome assembly in cancer. Thus, novel strategies are trying to find a valuable approach to impede proteasomal assembly alone or in combination with catalytic activity inhibitors, such as bortezomib or platinum pyrithione (Huang et al., 2017; Manasanch and Orlowski, 2017; Rousseau and Bertolotti, 2018).

6.2. Ubiquitin C-terminal hydrolases involvement in cancer

Special attention has been recently paid to the relationship between the UCH family and cancer (Fang et al., 2010). However, the specific role of certain UCH members as oncogene or tumor suppressor still remains controversial, as in the case of UCHL1. UCHs alterations have been related to tumor cell sensitivity to therapeutic modalities influencing several pathways that play crucial roles in cancer onset and development. Here, I briefly review UCH interest as a drug target, particularly focusing on UCHL5 and BAP1.

6.2.1. UCHL5

UCHL5 is mainly considered a tumor promoter. Abnormal protein levels are associated with the poor clinical outcome of certain cancer types. Overexpression of UCHL5 in tumoral tissues has been reported, especially in cervical carcinoma, hepatocellular carcinoma (HCC), esophageal squamous cell carcinoma (ESCC) and epithelial ovarian cancer (EOC) patients. However, UCHL5 knockdown is associated with lung cancer and pancreatic carcinoma, so further investigation is needed in order to unravel the molecular role of UCHL5 in cancer (Cutts et al. 2011; Rolen et al. 2006).

UCHL5 in tumor invasiveness

The clearest relationship between UCHL5 and cancer is via upregulation of transforming growth factor-β (TGF-β) signaling (Cutts et al., 2011; Wicks et al., 2006). High UCHL5 expression avoids the ubiquitination of type I TGF-β receptor, thus rescuing it from proteasomal degradation and producing an upregulation of TGF-β signaling. Consistently, the selective knockdown of UCHL5 reduces the levels of TGF-β-dependent target genes, such as MMP-2 and PAI-1, which are crucial proteins in promoting tumor migration and invasion (Fang and Shen, 2017).

6.2.2. BAP1

In contrast to UCHL5 and probably the other UCH family members, BAP1 has been recognized as a tumor suppressor, first reported in 2010, being somatically mutated in uveal melanoma. More recently, BAP1 has been shown to be implicated in a wide range of malignancies. BAP1 tumor alterations have been associated to BAP1 Cancer Predisposition Syndrome, which increases the risk of mesothelioma, uveal melanoma, cutaneous melanoma, cholangiocarcinoma, non-small-cell lung cancer, clear cell renal carcinoma, breast carcinoma and colorectal cancer (Fang and Shen, 2017). Both UCH and NLSs regions are considered essential for its role as tumor suppressor (**Figure 6**). Both BAP1 complete loss and partial inactivation are associated with cancer-specific mortality and recurrence of

cancer. This connection has been identified in all types of analyzed tumors except for mesothelioma, for which controversial opinions have been reported (Luchini et al., 2016). Hence, additional studies are needed to better understand the prognostic role of BAP1 in mesothelioma.

Homologous recombination and BAP1

Even though BAP1 binds to the wild-type BRCA1 RING finger domain, subsequent studies showed that BRCA1 is not a BAP1 deubiquitination substrate. However, in cellular models, BAP1 mutations impair the DNA damage response deregulating the E3-ligase activity of BRCA1-BRAD1 heterodimer (Nishikawa et al., 2009). In the context of BRCA1-BRAD1, there is a clear implication of BAP1 in homologous recombination participating in DSBs repair (Wadt et al. 2012), where resides the tumor-suppressive function of BAP1.

BAP1 participation on transcription and cell proliferation

BAP1 has also a crucial role in the nucleus interacting with host cell factor 1 (HCF1) and thus, recruiting several transcription factors. In this way, BAP1 regulates transcription and controls cell proliferation (Wang et al. 2016, Forma et al. 2014, Carbone et al. 2013). Its nuclear function requires its HCF1 binding motif (HBM) and its nuclear localization signal (NLS). Additionally, BAP1 is implicated in cell cycle progression through the polycomb group repressive deubiquitinase complex (PR-DUB) and sex combs (ASXL1/2) proteins, maintaining transcriptional

balances through histone 2A ubiquitination (Daou et al., 2015; Wang et al., 2016).

7. The influence of the ubiquitin proteasome pathway in the *C. elegans* germline dynamics

7.1. The proteasome participates in the cellular switch from proliferation to meiotic entry

C. elegans germline development is regulated by a tight balance between the number of cells that proliferate and the number of cells that enter meiosis to later differentiate as gametes. The UPS influences germline development at different levels: it promotes germ cell proliferation, regulates the balance between self-renewal and meiotic differentiation, and limits progression through meiotic prophase (Burger et al., 2013). Few studies demonstrate the link between proteasomal integrity/activity and germline associated phenotypes. For example, certain proteasome subunits are involved in *C. elegans* sex-determination: ubiquitin receptor *rpn-10* knockout sexually transform the gonad by elimination of hermaphrodite spermatogenesis (Shimada et al., 2006); conversely, *α*-subunit 5 (*pas-5*) mutant causes masculinized germlines (MacDonald et al., 2008).

The transition between stem/progenitor cells to meiotic entry and gametogenesis involves degradation of mitotic gene products and upregulation of genes and processes that promote meiotic entry. While GLP-1/Notch signaling promotes

the stem cell fate in the mitotic region, meiotic entry is controlled by three different functionally coordinated pathways: (1) GLD-1 pathway, (2) GLD-2 pathway and (3) ubiquitin-mediated degradation (mainly through the SCF E3 ubiquitin-ligase complex SCF^{PROM-1}) (Mohammad et al., 2018). Meiotic entry (meiotic prophase) includes meiotic S phase and the overt nuclear reorganization processes of homologous chromosome pairing, meiotic chromosome axis and synaptonemal complex[1] (SC) assembly, and the initiation of homologous recombination.

7.2. Ubiquitin-mediated degradation participates in meiotic prophase

7.2.1. DSB repair

Germ cells switch between specific DSB repair pathways depends on their temporal and spatial position in the *C. elegans* germline (Hayashi et al., 2007). During meiotic prophase, DSBs are induced. Among meiotic DBSs, a few are repaired by crossover pathway, which requires SC formation, leading to chromosome recombination; and others by non-crossover pathways when SC is absent. Failure in crossover and repaired of DSBs generated during homologous recombination, result in a battery of phenotypes such as aneuploidy, chromosome non-disjunction, embryonic lethality,

[1] SC is a proteinaceous complex that function as a scaffold mediating the tight association between homologous chromosomes during meiotic prophase.

anomalies in chromosomes and altered levels and distribution of RAD-51 foci at the pachytene stage (essential protein for homologous strand exchange). These aberrations finally lead to apoptotic cell death (Adamo et al., 2008).

As previously mentioned, BAP1 and the BRCA1-BRAD1 complex play a critical role in DNA repair and homologous recombination both in mammals and *C. elegans* (named BRC-1-BRD-1) (Wadt et al., 2012). In the context of meiosis, BRC-1 and BRD-1 location is initially nucleoplasmic and later these proteins are associated to chromosomes as meiosis progresses (Li et al. 2018, Janisiw et al. 2018). *brc-1* and *brd-1* mutants have mild meiotic phenotypes consistent with a role in some aspect of meiotic recombination (Boulton et al., 2004). As examples, *brc-1* mutants produce Him phenotype, which reflects higher frequency of X-chromosome non-disjunction and increased chromosome fragmentation at diakinesis which enhanced the embryonic lethality of mutants defective in chromosome synapsis (Adamo et al., 2008; Li et al., 2018).

7.2.2. Pairing homologs

A crucial step in the pairing of homologs in many organisms is the cytoplasmic dynein-driven chromosome movements that enable the alignment of homologs. In *C. elegans*, pairing centers[2] (PCs) are responsible for attaching chromosome ends

[2] PCs are specific repetitive DNA sequences present near one end of each homolog chromosome.

to cytoplasmic dynein via the SUN-1/ZYG-12 protein complex that spans the inner and outer nuclear envelopes (NEs) (Penkner et al., 2007; Sanford and Perry, 2001; Sato et al., 2009). The pairing event begins when each PC binds to a specific member of a family of zinc-finger proteins (Jagasia et al., 2005; MacQueen et al., 2005; Phillips and Dernburg, 2006). While the PC-binding protein–PC complex binds to SUN-1 at the nuclear periphery, ZYG-12 recruits dynein on the cytoplasmic side (Penkner et al., 2007; Sato et al., 2009). Upon interaction with the PC complex, the SUN-1/ZYG-12 complex aggregates into foci at specific sites on the NE, which is a hallmark of tethering chromosome ends to cytoskeleton (Sato et al. 2009). Recent studies have demonstrated (i) the presence of proteasome on meiotic chromatin in *C. elegans*, yeast and mice (Ahuja et al., 2017; Kumar and Subramaniam, 2018; Prasada Rao et al., 2017) and (ii) the ubiquitin-mediated proteostasis participation in tethering chromosomes during meiotic prophase in the *C. elegans* germline (Kumar and Subramaniam, 2018).

8. Catechol-*O*-methyl transferase (COMT) molecular function and its role in chemotherapy-induced toxicity

8.1. Human catechol-*O*-methyl transferases modulate neurotransmission by the degradation of dopamine

The complexity of dopamine (DA) metabolism becomes evident given the metabolic differences between species, organs and tissues. In the central nervous system (CNS), dopamine and other catecholamine (CA) metabolism is a unique feature of catecholaminergic neurons. Dopamine biosynthesis takes place in the cytosol of dopaminergic neurons by the classical CA biosynthetic pathway or by the alternative DA biosynthetic pathway (Meiser et al., 2013) (**Figure 7**). Once synthesized, DA is rapidly sequestered into synaptic vesicles, by secondary active transport via the vesicular monoamine transporter 2 (VMAT2), where the slightly acidic pH stabilizes DA and prevents its cytosolic oxidation (**Figure 8**). These synaptic vesicles are fused to the dopaminergic neuron membrane (degranulation) upon synaptic excitation and DA is released in the synaptic cleft, to interact with the postsynaptic DA receptors or regulatory presynaptic DA autoreceptors (Glennon et al., 2008; Zhang and Sulzer, 2012). The action of dopamine released in the synaptic cleft mainly ceases by DA reuptake and catabolism

through the activity of monoamine oxidases (MAO) in the dopaminergic neuron or alternatively, by MAO and catechol-*O*-methyltransferases (COMT) in surrounding glial cells and the periphery (**Figure 8**).

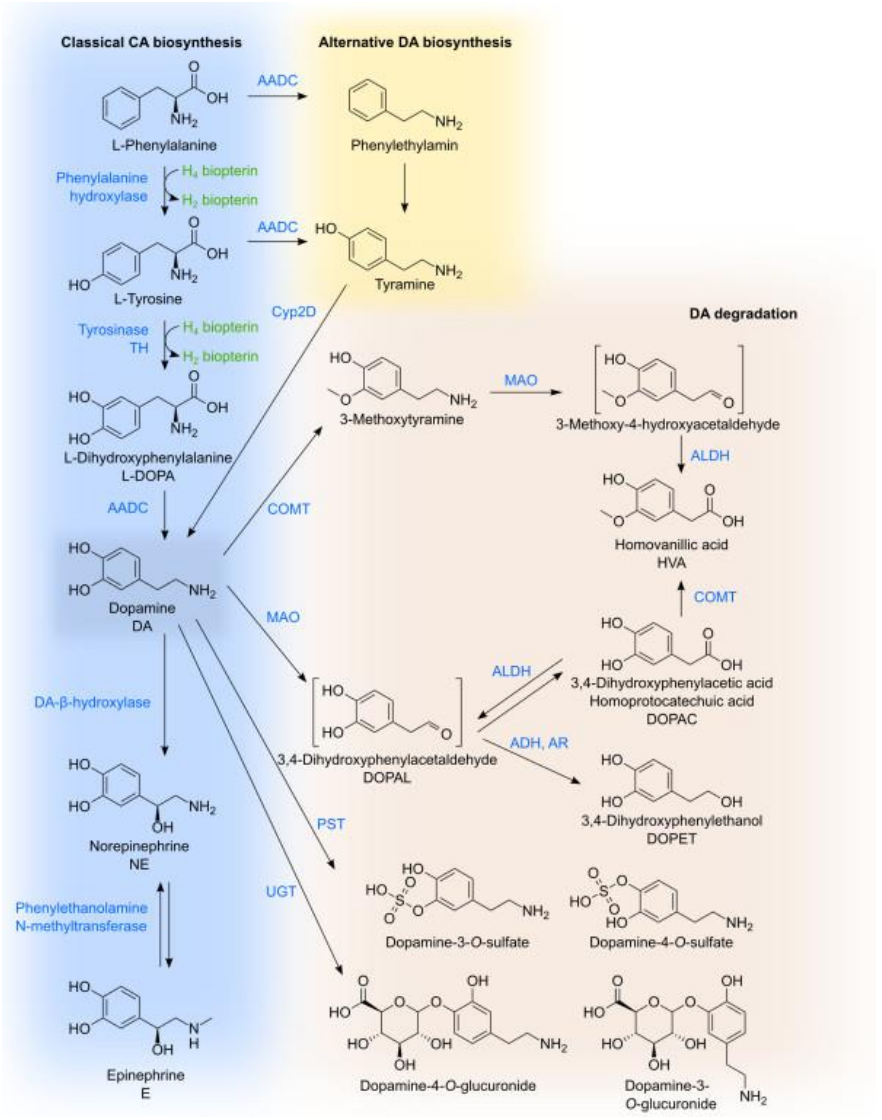

Figure 7: Dopamine biosynthesis and degradation. The classical DA biosynthetic pathway starts by hydroxylating tyrosine or phenylalanine by

phenylalanine hydroxylase to form L-DOPA. This oxidation is strongly regulated and depends on tetrahydrobiopterin (BH4) as a cofactor. L-DOPA is then decarboxylated to DA by aromatic amino acid decarboxylase (AADC, also known as DOPA decarboxylase). In the alternative pathway for DA synthesis, AADC action occurs before the hydroxylation at the aromatic ring. Tyramine is then oxidized to DA by Cyp2D. Besides being a neurotransmitter itself, DA is also the precursor of epinephrine and norepinephrine. DA degradation is performed by COMT, MAO, ADH, ALDH and AR in variable order leading to DOPAC and HVA as the main endproducts. Phenolsulfotransferases and uridine diphosphoglucuronosyltransferases catalyze conjugation reactions with phosphate and glucuronic acid, respectively. The relative contributions of the different enzymes are strongly species-, tissue- and cell type-dependent. The reactions may occur in distinct compartments. Figure adapted from Meiser et al. 2013.

Dopamine metabolism itself is strongly linked to oxidative stress as its degradation generates reactive oxygen species (ROS) in CA neurons. In fact, it is suggested that MAO inhibition might protect DA neurons from oxidative stress (Napolitano et al., 1995). Moreover, DA oxidation can lead to endogenous neurotoxins whereas some DA derivatives show antioxidant effects. Therefore, DA metabolism is especially important for neuronal redox-homeostasis and viability (Meiser et al., 2013)**.** Neurodegenerative disorders such as Parkinson's Disease have been associated with DA metabolism or signaling, emphasizing the importance of a well-balanced DA metabolism (Breier et al., 1999; Heinz and Schlagenhauf, 2010; Tripp and Wickens, 2012).

In the dopamine catabolic pathway, COMT is the rate-limiting enzyme catalyzing the magnesium-dependent transfer of methyl groups from S-adenosyl methionine to a hydroxyl group on dopamine, converting it to 3-methoxytyramine (**Figure 7**). COMT also functions in the parallel monoamine oxidase-limited pathway to convert dopacetic acid (DOPAC) to homovanillic acid (HVA) (**Figure 7**).

Two isoforms are encoded by the sole human COMT gene, located in the chromosome 22. The soluble cytoplasmic form (S-COMT) present in glial cells and the periphery, and the rough endoplasmic reticulum-bound isoform (M-COMT), prevalent in neurons. The latter has a higher catecholamine affinity and is mainly responsible for metabolism of compounds derived from dopamine and norepinephrine neurotransmission, whereas the soluble S-COMT is mainly responsible for catabolism from exogenous catecholamines (Napolitano et al. 1995; Tenhunen et al. 1994). COMT activity is higher in excretory organs such as liver and kidney but is also present in the CNS where is more abundant in microglial cells. Moreover, COMT-dependent catechol methylation has been related with the protection of dopaminergic neurons (Werner *et al.,* 2000) and detoxification of endogenous and exogenous compounds containing catechol groups that may become toxic, mutagenic or carcinogenic.

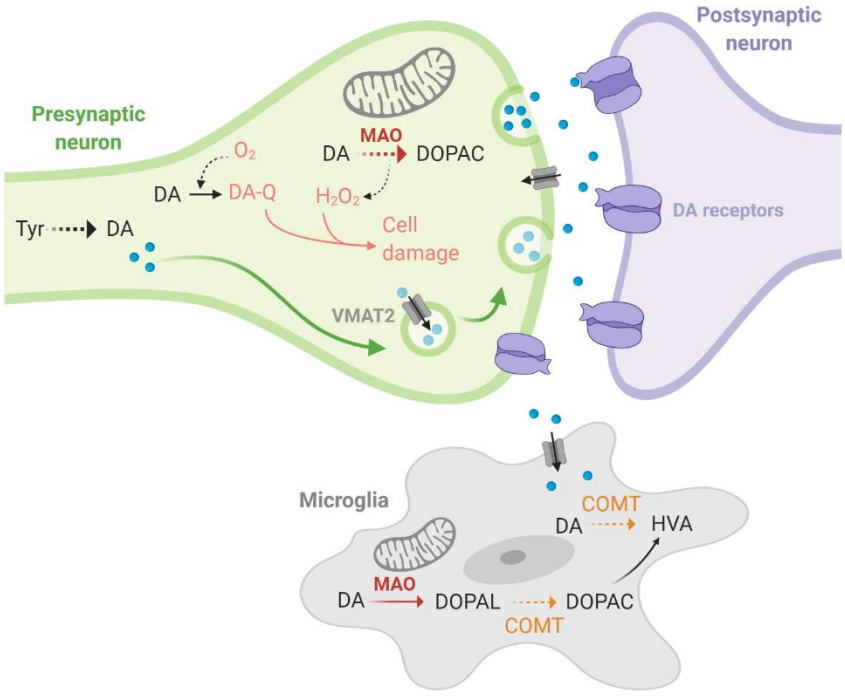

Figure 8: Simplified view of neuronal DA metabolism. DA biosynthesis takes place in dopaminergic cytoplasm and is then immediately imported into synaptic vesicles by VMAT2. DA leaking from the vesicles is deaminated by MAO. Upon neuronal excitation DA is released into the synaptic cleft for signal transduction. DA signaling stops by DA reimport to the presynaptic neuron and recycling or by DA import to surrounding cells and degradation. The main DA degradation products are DOPAC and HVA. In the cytoplasm or cytoplasmatic vesicles (not represented), DA or DOPA can be oxidized to their corresponding reactive quinones (Q) that react further on to form a variety of partly neurotoxic compounds and protein adducts that will cause cell damage and neurodegeneration. Created with BioRender.com.

8.2. Association between COMT genetic variants and cisplatin-induced ototoxicity

As I previously mentioned (**Introduction 2**), the high efficacy and good prognosis of cisplatin are accompanied by a set of severe toxic side-effects and acquired and/or intrinsic resistance. The mechanisms by which cisplatin induces cytotoxicity in normal cells remains still obscure in most of the cases, particularly in the nervous system. Among the dose-limiting side effects for cisplatin antitumor therapies in children, the most common are ototoxicity and nephrotoxicity. More than 60% pediatric cancer patients treated with cisplatin suffer hearing loss, compromising language and cognitive development of these children (Ross et al., 2009). Catechol-*O*-methyltransferase (COMT), acylphosphatase 2 (ACYP2) and thiopurine methyltransferase (TPMT) genetic variants have been related to ototoxicity in children with cancer treated with cisplatin (Thiesen et al., 2017).

TPMT and COMT are methyltransferases that require SAM, a methyl donor substrate in the methionine pathway. Interestingly, it is suggested that not only ototoxicity, but also nephrotoxicity associated with cisplatin may be related to an accumulation of SAM substrate, resulting from a reduction in the activity of TMPT or COMT in the presence of cisplatin (Ross et al., 2009). Other studies show that the transmembrane form of COMT is expressed in the inner and outer hair cells of the cochlea, being essential for proper

auditory function in both mice and humans (Ahmed et al., 2008; Du et al., 2008; Duman et al., 2011; Ross et al., 2009).

Despite evidences supporting that the absence of COMT activity may result in hearing loss (Pussegoda, 2010), there is controversy regarding the relationship between COMT genetic variants and cisplatin-induced ototoxicity (Mukherjea and Rybak, 2011; Olgun et al., 2016; Ross et al., 2009; Teft et al., 2019; Thiesen et al., 2017; Yang et al., 2014).

9. *C. elegans* as a valuable model to study biogenic amine signaling and behavior under drug exposure

In *C. elegans* four biogenic amines -octopamine, tyramine, dopamine and serotonin- act modulating behavior. These neurotransmitters function in both neurons and muscles to affect egg laying, pharyngeal pumping, locomotion, and learning. However, other signaling amines found in vertebrates (histamine, epinephrine, and norepinephrine) appear not to be produced in *C. elegans* cells. Enzymes responsible for these neurotransmitter syntheses, as well as gene products in charge of vesicle loading during synaptic signaling, were identified in *C. elegans* (Chase and Koelle, 2007). Conveniently, many tools are available to study the molecular and cellular mechanisms of signaling by biogenic amines in this nematode.

Moreover, particularly important is that is the only organism for which the complete connectome has been explored, meaning

every single neuron can be tracked and its functionality can be investigated in the living animal (White JG, Southgate E, Thomson JN, 1986). For example, by studying animal behavior. Taking the multiple advantages of this model, many studies have been developed to understand biogenic amine signaling and its implications in other systems such as the human brain (Nass et al., 2002).

Catechol-*O*-methyltransferase enzymes are also present in the nematode and in particular, *comt-4* has been related to dopamine signaling modifying locomotor behavior (Rodríguez-Ramos et al., 2017a). In addition, *C.elegans* is a great model to study signaling pathways in response to drug exposure and especially as a model organism to study effects of genotoxic drugs (Honnen, 2017). Recently, we have proposed a method to investigate the cellular response to cisplatin in *C. elegans* (García-Rodríguez et al. 2017). In that study, we reported transcriptomic upregulation of *comt-4* when animals are exposed to cisplatin suggesting a molecular implication of this enzyme in the drug response.

9.1. Brief overview of *C. elegans* dopaminergic system

Dopamine is synthesized in eight neurons in the hermaphrodite (**Figure 9**) and in six additional neurons located in the tale of the male. These fourteen neurons are thought to be mechanosensory, since ablation of these neurons or

blockage of DA synthesis cause defects in the animals ability to sense and respond to environmental changes (Sawin et al., 2000). The metabolic pathways for catecholamines biosynthesis and catalysis, as well as the enzymes involved in these processes are conserved from human to worm. Moreover, synapsis-related vesicular transporters and DA receptors have orthologs in the nematode (Nass and Blakely, 2003). The **Table 1** contains a description of the main enzymatic key players involved in neuronal DA metabolism in *C. elegans* and its human orthologs.

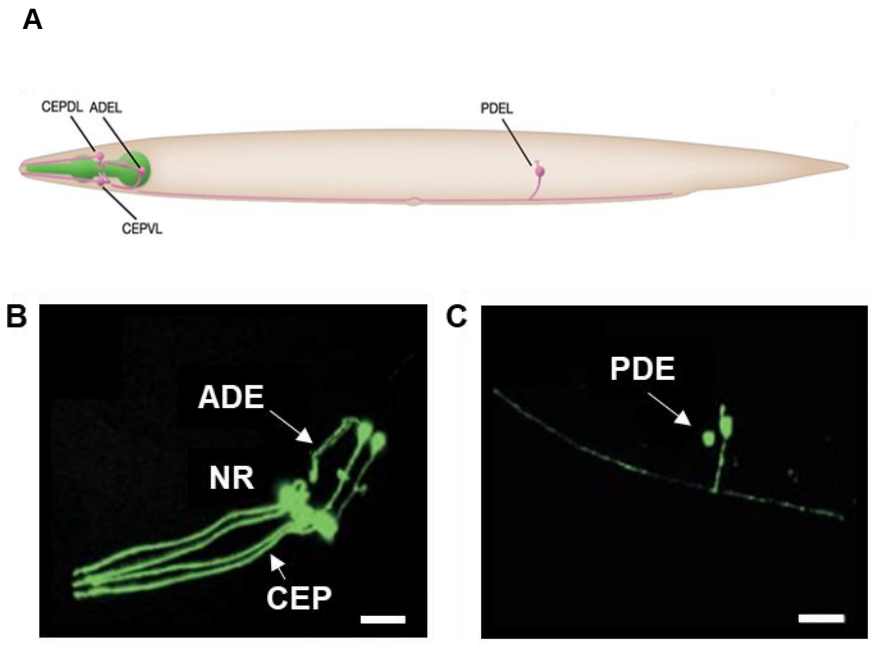

Figure 9: Hermaphrodite dopaminergic neurons. The *C. elegans* hermaphrodite contains eight dopaminergic neurons: four symmetrically arranged cephalic cells (CEPs), two bilateral anterior deirids (ADEs) in the head, and two bilateral posterior deirids (PDEs), which control processes

that run through the main part of the body and tail. **A.** The scheme represents the lateral view of DA neurons (taken from WormAtlas). The bottom panels show two images from the reconstruction of confocal epifluorescence from dopaminergic neurons using adult hermaphrodite DAT-1::GFP transgenic line (Nass and Blakely, 2003). Arrows identify ADE and CEP neurons in the head (**B**) and dorsal PDEs (**C**). NR refers to the nerve ring where synaptic connections from other neurons are found. Scale bars represent 25 µm.

Table 1: Main genes involved in *C. elegans* DA metabolism.

Process	***C.elegans* gene**	**Human gene**	**Enzymatic activity**
Biogenic amine synthesis	*cat-2*	TH	Tyrosine hydrolase (requires BH_4 cofactor)
	cat-4	GTPCH	GTP cyclohydrolase (for BH_4 synthesis)
	bas-1	AAAD	Aromatic amino acid decarboxylase
Monoamine degradation	*comt-1/2/3/4/5*	COMT	Catechol-*O*-Methyltransferase
	amx-2	MAO-A/B	Monoamine oxidase
DA transporters	*cat-1*	VMAT	Vesicular amine transporter
	dat-1	DAT	DA transporter
	dop-1	DOP1	D1-like DA receptor

AIMS

1. To generate and characterize a model of BAP1 cancer-related mutations in *C. elegans*.

2. To explore the impact of glucose and lipid metabolism on cisplatin toxicity.

3. To establish a method to investigate cisplatin neurotoxicity in *C. elegans*.

RESULTS

PART I: UBH-4

1. *ubh-4* is the *C. elegans* ortholog of human BAP1 and UCHL5 ubiquitin C-terminal hydrolases

We were interested in BAP1 because this gene presents germline mutations that have been pointed as predisposing factors for hereditary cancers (Masoomian et al., 2018). In order to identify BAP1 orthologs in *C. elegans*, the protein sequence was used as query to search protein databases by BLASTP (Camacho et al., 2009). Based on protein sequence similarity, UBH-4 was identified as the ortholog of human UCHL5 and BAP1, sharing 47,13% and 33,14% of identity, respectively (**Table 2**). Thus, although the highest percentage identity is shared with UCHL5, we propose UBH-4 as the closer BAP1 homolog in *C. elegans*.

BAP1 and UCHL5 belong to the ubiquitin C-terminal hydrolase (UCH) family, which is part of the ubiquitin cysteine peptidase C12 superfamily. Both proteins contain a conserved N-terminal catalytic domain with cysteine peptidase activity, based on phylogenetic analysis provided by TreeFam v9 program (Schreiber et al. 2014) ans BLASTP analysis (**Figure 10**). Additional members of *C. elegans* UCH family (UBH-1, UBH-2 and UBH-3) also display protein sequence similarities with BAP1 (detailed in **Table 2**). These phylogenetic analyses indicate that UCHL5 and BAP1 would keep the ancestral functional roles of UBH-4.

As I previously mentioned (**Introduction 6.2**), BAP1 is involved in many cellular processes including cell cycle regulation, DNA damage response, and possibly, regulation of ubiquitin-mediated degradation. Many studies have identified BAP1 cancer-related mutations, predominantly throughout its conserved catalytic domain, but the functional consequences of these mutations are still largely unknown. For this reason, and given the sequence similarities, we were interested in investigating the effects of mimicked BAP1 cancer-related mutations in *C. elegans.*

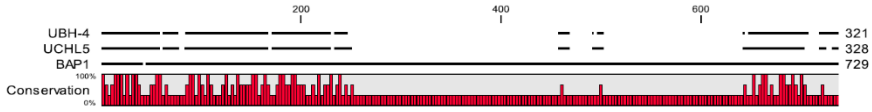

Figure 10: Homology between BAP1, UCHL5 and UBH-4. Scheme of UBH-4, UCHL5 and BAP1 protein sequences (black lines) and conserved residues (red bars), predominantly at the N-terminal and C-terminal domains. The last region is required for BAP1 and UCHL5 protein-protein interactions and regulatory functions (Sanchez-Pulido et al., 2012). Alignments were illustrated by CLC Sequence Viewer 8.0.

Table 2: BLASTP analysis of *C. elegans* UCHs proteins compared to BAP1 and UCHL5.

	Protein	Query cover (%)	Identity (%)
BAP1	UBH-4	56	33,14
	UBH-1	26	25,25
	UBH-2	29	26,6
	UBH-3	25	23,08
UCHL5	UBH-4	95	47,13
	UBH-1	69	23,56
	UBH-2	81	25,31
	UBH-3	88	23,97

2. *ubh-4* missense mutations mimicking BAP1 cancer-related mutations do not display any overt phenotypes

2.1. BAP1 cancer predisposition syndrome and distribution

BAP1 tumor alterations have been associated to BAP1 cancer predisposition syndrome, consisting in the development of melanocytic skin tumors at early age and, later in life, high incidence of mesothelioma, uveal melanoma, cutaneous melanoma and possibly additional cancers (Carbone et al., 2013). According published studies collected by cBioPortal (Cerami et al., 2012), including an average of almost 2.000

tumor samples, the most frequent type of cancer with BAP1 alterations are Pleural Mesotheliomas and Uveal Melanoma (up to 40%), followed by Cutaneous Melanoma (around 3%) (**Figure 11A**). BAP1 involvement in cancer is typically caused by alterations that affect protein functions or cause protein deletion (Harbour et al., 2010; Murali et al., 2013). Among these, missense mutations are the most common alterations affecting, predominantly, the peptidase C12 catalytic domain (**Figure 11B**), which is essential for its cellular functions (Ventii et al., 2008).

2.2. Modeling BAP1 missense mutations in *C. elegans*

Since there are many residues conserved between BAP1 and UBH-4 peptidase C12 domain (**Figure 12A**), we were capable of mimicking missense cancer-related mutations in *C. elegans* to explore its functional implication in a pluricellular organism. For that purpose, we reproduce two missense mutations: F81V, identified in different types of cancer as malignant pleural mesothelioma (MPM) (Bott et al., 2011; Ismail et al., 2014); and A95D. Both residues are situated in the catalytic domain close to C91, a residue functionally relevant at the active site (Jensen et al., 1998), affecting the catalytic activity of BAP1 (Bott et al., 2011; Ventii et al., 2008).

In *C. elegans*, the equivalent residues are located at F73 and A87 aminoacidic positions (**Figure 12A**). CRISPR/Cas9 was

used to generate these missense mutations producing the alleles *cer25*[F73V] and *cer32*[A87D]. Molecular designs are detailed in **Figure 12B**, and reagents used for this purpose are described in **Materials and methods 3**.

BAP1 cancer-related mutations, F73V and A87D, do not cause any obvious phenotype in *C. elegans*. In terms of brood size, only *cer25* produces a slightly decrease in the number of hatched larvae (data not shown). These results allow to further explore the functional relevance of these mutations in a isogenic population of nematodes.

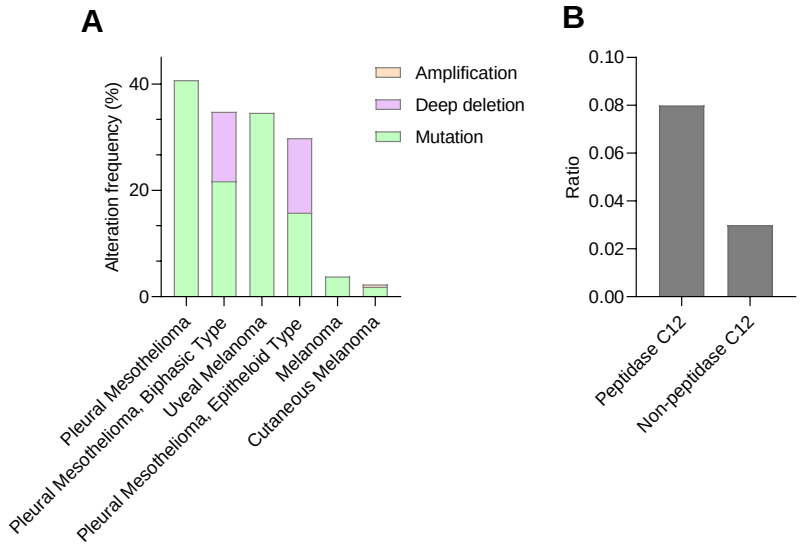

Figure 11: BAP1 alteration frequency in BAP1 cancer predisposition syndrome and cancer distribution. A. BAP1 alteration frequency in BAP1 cancer predisposition syndrome-related cancer types. Percentage of alteration form per cancer type are detailed by colors. **B.** Ratio of missense mutation distribution located or not in the in peptidase C12 BAP1 region. Data were collected from cBioPortal.

Figure 12: CRISPR/Cas9 editing of two conserved BAP1 cancer-related residues in *ubh-4*. A. Alignment of BAP1 and UBH-4 catalytic domain showing high percentage of sequence similarity. Red bars represent the percentage of conservation between species and pink shadows point out residues to mutate (human/*C. elegans* F81/F73 and A95/A87). **B.** Molecular designs to generate the *ubh-4* cancer-related alleles *cer25* and *cer32* by CRISPR/Cas9. Sense strands are represented. PAM sequences are shown in yellow. crRNA sequences are underlined and Cas9 cut sites are indicated by black arrows. Silent mutations are labelled in light blue. Mutated codons are shown in pink, and nucleotide changes, T>G (*cer25*) and C>A (*cer32*) are underlined. Aminoacidic sequences are represented, highlighting in pink the mutated residues.

A

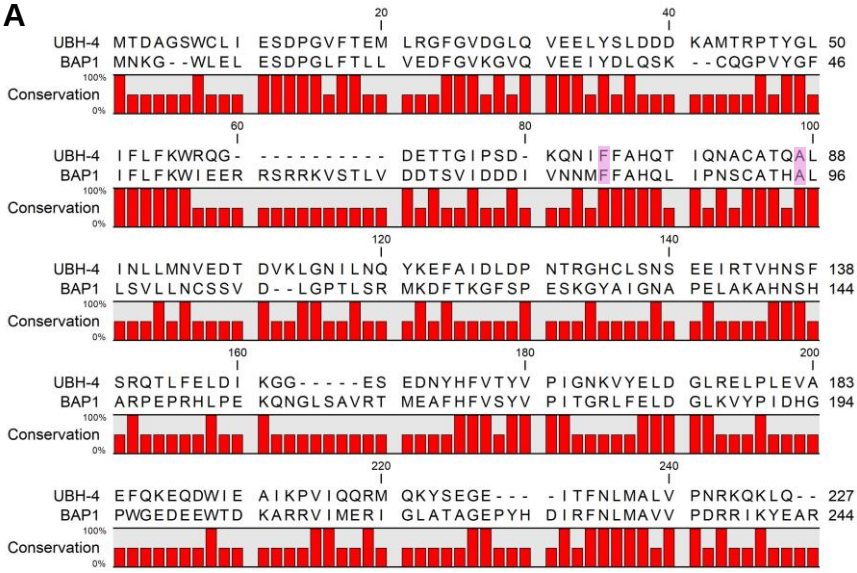

B

F73V

Wild-type allele

5'…ACT-GGG-ATT-CCT-AGT-GAC-AAG-CAA-AAC-ATC-TTT-TTT-GCT-CAT-CAA-ACA-ATT-CAA-AAC-GCT-TGT
Tyr Gly Ile Pro Ser Asp Lys Gln Asn Ile Phe Phe Ala His Gln Thr Ile Gln Asn Ala Cys

Mutant allele: *cer25*

5'…ACT-GGG-ATT-CCG-TCG-GAT-AAA-CAA-AAT-ATA-GTT-TTT-GCT-CAT-CAA-ACA-ATT-CAA-AAC-GCT-TGT
Tyr Gly Ile Pro Ser Asp Lys Gln Asn Ile Val Phe Ala His Gln Thr Ile Gln Asn Ala Cys

A87D

Wild-type allele

5'…CAA-ACA-ATT-CAA-AAC-GCT-TGT-GCT-ACT-CAA-GCT-CTC-ATC-AAC-TTG-CTT-ATG-AAC-GTG-GAA-GAT
Gln Thr Ile Gln Asn Ala Cys Ala Thr Gln Ala Lue Ile Asn Leu Leu Met Asn Val Glu Asn

Mutant allele: *cer32*

5'…CAA-ACA-ATT-CAA-AAC-GCT-TGT-GCT-ACT-CAA-GAT-CTT-ATC-AAC-CTG-CTG-ATG-AAT-GTA-GAA-GAT
Gln Thr Ile Gln Asn Ala Cys Ala Thr Gln Asp Leu Ile Asn Leu Leu Met Asn Val Glu Asn

3. Characterization of UBH-4 expression pattern

3.1. Generation of *ubh-4* translational endogenous reporter by Nested CRISPR

Given the absence of major phenotypic alterations in *cer25* and *cer32*, we wanted to explore the expression of UBH-4 *in* vivo. For this purpose, we generated a fluorescent endogenous reporter by Nested CRISPR (Vicencio et al., 2019). Nested CRISPR is a cloning-free ribonucleoprotein-driven method that allows the efficient generation of endogenous fluorescent reporters in *C. elegans*. In the case of *ubh-4*, we created a translational endogenous reporter with the green fluorescent protein EGFP. We first used a ssDNA donor (≤200 bp) to insert the 5' and 3' fragments of the EGFP at the *ubh-4* 3' end. In the second step, this small fragment, including 35bp homology regions, was used as landing pad to insert the middle fragment (using dsDNA—PCR product— as donor) to complete the EGFP sequence. As a result, we generated the strain CER395: *ubh-4(cer68[ubh-4::EGFP])II.*

3.2. UBH-4 is ubiquitously expressed during *C. elegans* development

Taking advantage of the transparency of *C. elegans*, we clearly visualized UBH-4::EGFP under the fluorescent microscope in living animals from embryo to adult stages. UBH-4 is ubiquitously expressed all developmental stages (**Figure 13**).

Such observation is consistent with the expression profile provided by GExplore 1.4 interface (Hutter and Suh, 2016) (**Figure 14A**). Based on GExplore, *ubh-4* is abundantly expressed in distinct cell types as germ cells, neurons or glia-like cells, with an average of 460, 253 or 220 transcripts per million, respectively (**Figure 14B**).

Deeply observation of UBH-4::EGFP in the adult germline (**Figure 13.4**, **13.5**), revealed that in the meiotic region, the fluorescence signal becomes more intense (**Figure 13.4**, **13.5**, **c**-**e**). After the proliferative region (mitotic zone) of germline, cells go through a gradient of meiotic stages until they get paused at the final stage of prophase (from pachytene (**b**) to diakinesis (**e**)). During these stages, along with oocytes maturation, chromosomes get paired, recombination occurs, and finally condensed chromosomes are prepared to meiotic division I. Then, oocytes are pushed through the spermatheca where sperm entry resumes the first meiotic division followed closely by complete the meiosis II. According to the intensity of UBH-4::EGFP signal throughout the germline, we hypothesize that UBH-4 could have a relevant role during meiotic prophase (pachytene (**c**) and diakinesis (**e**)).

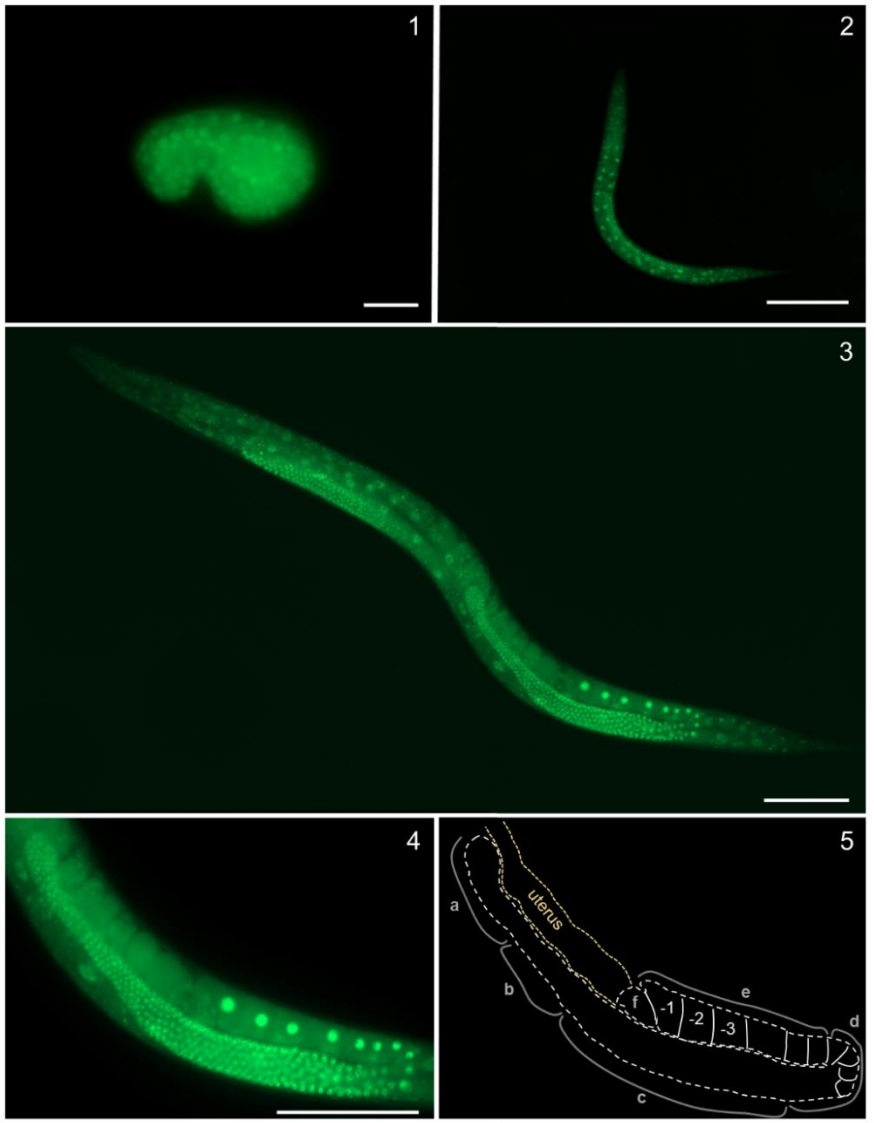

Figure 13: UBH-4 expression *in vivo*. Representative images of EGFP signal in CER395 developing embryo (**1**), L3 (**2**) and adult (**3**). Scale bars represent 10, 100 and 100 µm, respectively. (**4**) Posterior arm of the adult gonad at higher magnification (scale bar means 100 µm). (**5**) Diagram of (**2**) showing distal mitotic (**a**), transition (**b**), pachytene (**c**), diplotene (**d**) and diakinesis (**e**) zones, and spermatheca (**f**).

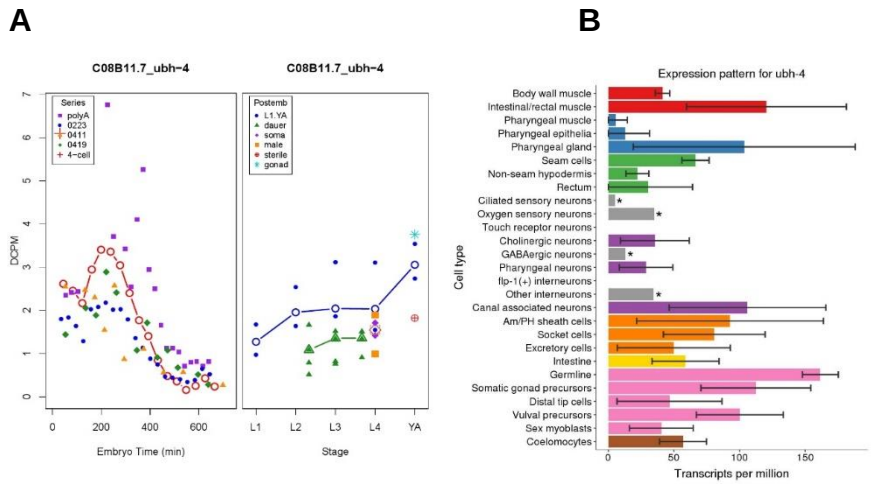

Figure 14: UBH-4 expression profile. Expression pattern by developmental stage, presented as the average depth of coverage per million mapped reads (DCPM) (**A**), and UBH-4 transcripts per million by cell type in L2 larval stage (**B**), provided by GExplore 1.4.

4. *ubh-4* is not essential for development

ubh-4 gene produces two transcripts, C08B11.7.1 and C08B11.7.2, both with a 966-nt coding sequence only differing at their 3' UTR (**Figure 15A**). We generated null alleles for *ubh-4* by non-specific NHEJ (non-homologous end joining) repair of a CRISPR/Cas9-induced DSB (allele *cer27)*, and by HDR (homology directed repair) using a repair template (allele *cer150)*, resulting in the depletion of 1033 (*cer27*) and 1054 (*cer150*) base pairs, respectively. As a result of this editing, the start codon was eliminated in both alleles, and therefore these alleles were considered null or absent of function. Two different gene-specific crRNAs where used for two CRISPR-induced cuts at 5´and 3´ ends of the gene. The molecular design of this editing is illustrated in **Figure 15B.** Furthermore, the

sequences of cRNAs and repair templates needed to generate these alleles are detailed in **Materials and Methods 3.**

Both deletion alleles were functionally characterized to investigate the role of UBH-4 during development. Surprisingly, despite *ubh-4* being expressed ubiquitously and maintained along the *C.elegans* lifecycle, no overt phenotypes were identified. Only slightly reduced brood size was observed in *cer27* compared to N2 (WT) animals (data not shown).

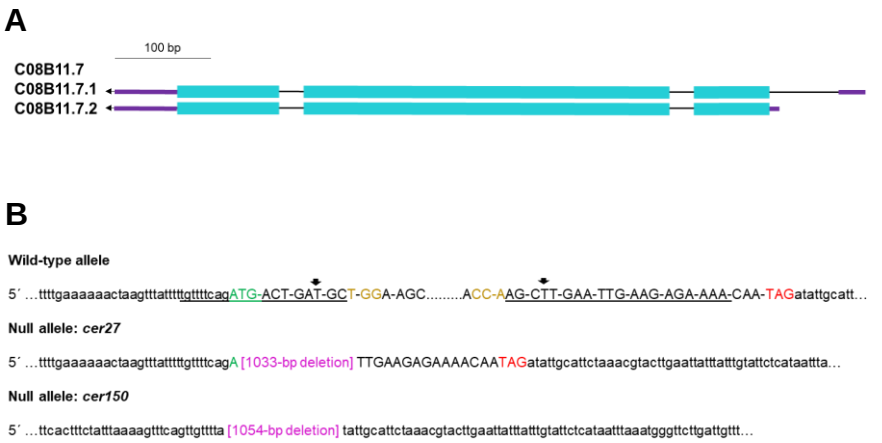

Figure 15: *ubh-4* locus and molecular design for the generation of *cer27* and *cer150* null alleles. A. Schematic representation of both *ubh-4* transcripts, C08B11.7.1 and C08B11.7.2. Introns are shown by black lines, 5´and 3´UTRs (untranslated regions) by purple bars and exons by light blue bars. **B.** Sense strand sequences of wild-type and null alleles produced by nonspecific (*cer27*) and homology (*cer150*) repair after CRISPR/Cas9 edition. Start and stop codons are drawn in green and red, respectively. PAM sequences are shown in yellow. crRNA sequences 3´and 5´are underlined and cut sites are shown by black arrows. The resulting deletion length is represented in pink. 5' UTRs and intron at 3' partial sequences are indicated in lowercase.

5. Identified a genetic interaction between *ubh-4* and *rpn-9* by RNAi screen

Given the absence of overt phenotypes in *ubh-4* null mutants (*cer27* and *cer150*) and cancer-related mutant alleles (*cer25* and *cer32*), an RNAi screen was performed in a *ubh-4* knockout background to search for genetic interactors. The lack of *ubh-4* mRNA was demonstrated by quantitative PCR in *ubh-4*(*cer27)* —the allele used in this screen—showing a relative fold change of 0,008 compared to N2 (WT).

Genes included in the screen were selected taking into account the role of UBH-4 orthologs BAP1 and UCHL5 (**Introduction 5.2.3** and **6.2**). Thus, proteasome-related enzymes, 20S and 19S proteasome particle subunits, and putative and confirmed BAP1 interactors were considered candidates for the screen. Moreover, a collection of genes frequently mutated in cancer (Poulin et al., 2004), and a set of genes related with Malignant Mesothelioma and Melanoma (Kato et al., 2016; De Rienzo et al., 2016; Soura et al., 2016) were selected if they were conserved in *C. elegans* (https://wormbase.org/ and BLASTP (Camacho et al., 2009)). In addition, putative UBH-4-protein interactors were included in the screen based on STRING 11.0 database (Szklarczyk et al., 2019).

Once candidate genes were selected, they were identified in the two genome-wide RNAi libraries available in our lab (from Marc Vidal and Julie Ahringer laboratories) and the clone size

was validated by PCR. Thus, a 150-genes sublibrary was generated the RNAi screen (**Materials and Methods 7.1 and 7.2**). **Table 3** contains the candidate gene list used in the screen, including a gene description, the RNAi library from which they were obtained and the observed phenotype in both WT and *ubh-4(cer27)* backgrounds. Schematic representation of the workflow is shown in **Figure 16**.

The 150-gene RNAi sublibrary was screened, in 24-well plates at 20°C. Clones producing synthetic interactions, were further validated in larger RNAi plates (55 mm of diameter) (**Materials and Methods 7.3**, **Table 16**). As a result of this screen, we observed that partial inactivation of *rpn-9,* a non-ATPase subunit of the 19S proteasome, produced a robust synthetic interaction: significantly reduced brood size in *ubh-4(cer27)* mutants compared to WT (**Figure 17B**). In addition, to a minor extent, *rpn-9(RNAi)* caused embryonic lethality and cuticle abnormalities in the F1 progeny were observed in both *ubh-4(cer27)* and WT animals upon *rpn-9* knockdown. Therefore, *rpn-9* was identified as a *ubh-4* genetic interactor.

Among the proposed role of RPN-9, there are controversies regarding its implication on proteasome assembly. While some consider RPN-9 as a non-essential proteasome subunit in terms of cellular viability (Hu et al., 2015b), others supports that it is essential for proteasome integrity and activity, being required for the assembly of proteasome regulatory particle 19S (D'Arcy, Wang, and Linder 2015; Hu et al. 2015; Takeuchi

et al. 1999; Tanaka 2009). Thus, we hypothesized that *ubh-4* and *rpn-9* may have a cooperating role in proteasome functionality.

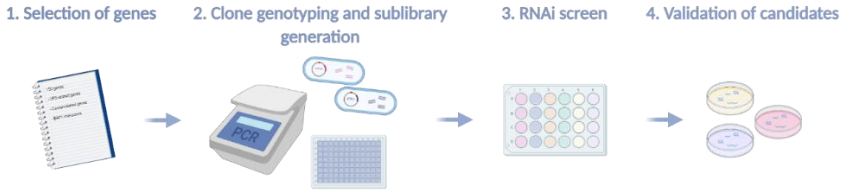

Figure 16: RNAi screen workflow. After candidate genes selection (**1**), clones from RNAi libraries were cherry-picked and genotyped in order to generate 150-gene RNAi sublibrary for the screen (**2**). For the RNAi screen, 150-RNAi cultures were IPTG-induced in RNAi 24-well plates. Synchronized L1 animals were seeded and checked every day during 120 hours at 20°C, to score both WT and *cer27* animals (**3**). Finally, candidate genes were validated in larger (55 mm-diameter) RNAi plates (**4**). Figure created with Biorender.com.

Table 3: Candidate interactors and RNAi screen results.

Gene classification	*C. elegans* locus	Human Ortholog	Description	*C. elegans* clone	RNAi library	WT (N2)	*ubh-4(cer27) II*
Proteasome-related deubiquitinating enzimes	***ubh-1***	UCHL1	Cystein proteases (Cys-His boxes catalytic core). Ubiquitin C-terminal hydrolases (UCHs)	F46E10.8	JA	WT	WT
	ubh-2	UCHL1, UCHL3		Y40G12A.2	JA	Rbs	Rbs
	ubh-3	UCHL1, UCHL3		Y40G12A.2	JA	Rbs	Rbs
	ubh-4	UCHL5/BAP1		C08B11.7	JA	WT	WT
	otub-1	OTUB1, OTUB2	Cystein proteases (Cys-His-Asp catalytic core). Ovarian tumour protesaes (OTUs)	C25D7.8	MV	Ste, Gro	Ste, Gro
	otub-2	OTUD7B		Y50C1A.1	MV	WT	WT
	otub-3	OTUD6A, OTUD6B		F21D5.2	MV	WT	WT
	math-33	USP48	Cystein proteases (Cys-His boxes catalytic core). Ubiquitin specific proteases (USPs)	H19N07.2	JA	WT	WT
	H34C03.2	USP5, USP15, USP11		H34C03.2	JA	WT	WT
	K02C4.3	USP28, USP25		K02C4.3	JA	WT	WT
	K08B4.5	-		K08B4.5	JA	WT	WT
	usp-33	USP33, USP20		K09A9.4	JA	WT	WT
	usp-46	USP46		R10E11.3	MV	WT	WT
	T05H10.1	USP47		T05H10.1	JA	WT	WT
	T22F3.2	USP42		T22F3.2	JA	WT	WT
	usp-5	USP5, USP13		T27A3.2	JA	WT	WT
	duo-3	FBXL4		Y106G6H.12	MV	WT	WT
	usp-3	USP3		Y71A12B.j	MV	WT	WT
	cyk-3	USP23, USP6, USP49, USP44		ZK328.1	MV	WT	WT
	C04E6.5	USP26, USP29, USP37, FBXL4		C04E6.5	JA	WT	WT
	usp-14	USP14		C13B4.2	MV	WT	WT
	C34F6.9	-		C34F6.9	MV	Lva	Lva
	usp-33	USP39		F09D1.1	MV	WT	WT
	usp-50	FBXL17		E01B7.1	MV	WT	WT
	duo-2	USP48		F29C4.5	MV	WT	WT
	usp-48	USP48		F30A10.10	JA	Rbs	Rbs
	F35B3.1	-		F35B3.1	JA	WT	WT
	duo-1	FBXL4, USP26		F38B7.5	JA	WT	WT
	cyld-1	CYLD1		F40F12.5	MV	WT	WT
	atx-3	ATXN3	Cystein protease (Cys-Gln-His-Asp catalytic core). Machado–Josephin domain protease (MJD)	F28F8.6	MV	WT	WT
	csn-5	COP9S5	Metalloproteases (His-Asp-Zn2+ catalytic core). JAMM proteases	B0547.1	MV	WT	WT
	eif-3.H	EIF3H		C41D11.2	JA	Rbs	Rbs
	eif-3.F	EIF3F		D2013.7	MV	Ste, Gro	Ste, Gro
	prp-8	PRPF8		C50C3.6	JA	Lva	Lva
	F37A4.5	PSMD14		F37A4.5	MV	WT	WT
	csn-6	COP9S6		Y67H2A.6	JA	WT	WT
20S proteasome	***pas-1***	PMSA6	α-type subunits	C15H11.7	MV	Lva	Lva
	pas-2	PMSA2		D1054.2	MV	Lva	Lva
	pas-3	PMSA4		Y110A7A.14	MV	Ste	Ste
	pas-4	PMSA7		C36B1.4	MV	Lva	Lva
	pas-5	PMSA5		F25H2.9	MV	Lva	Lva
	pas-6	PMSA1		CD4.6	MV	WT	WT
	pas-7	PMSA3		ZK945.2	MV	Lva	Lva
	psb-2	PSMB7		C47B2.4	MV	Lva	Lva

particle subunits							
	psb-3	PSMB3	β-type subunits	Y38A8.2	MV	Lva	Lva
	psb-4	PSMB2		T20F5.2	JA	Lva	Lva
	psb-5	PSMB5		K05C4.1	MV	Lva	Lva
	psb-6	PSMB1		C02F5.9	MV	Lva	Lva
	psb-7	PSMB4		F39H11.5	MV	Lva	Lva
19S proteasome particle subunits	***rpt-1***	PSMC2	ATPase subunits	C52E4.4	MV	Ste. Rbs, Lva(F1)	Ste. Rbs, Lva(F1)
	rpt-2	PSMC1		F29G9.5	MV	Lva	Lva
	rpt-3	PSMC4		F23F12.6	MV	Lva	Lva
	rpt-4	PSMC6		F23F1.8	MV	Ste, Pva	Ste, Pva
	rpt-5	PSMC3		F56H1.4	MV	WT	WT
	rpt-6	PSMC5		Y49E10.1	JA	Lva	Lva
	rpn-1	PSMD2	Non-ATPase subunits	T22D1.9	JA	Lva	Lva
	rpn-2	PSMD1		C23G10.4	MV	Lva	Lva
	rpn-3	PSMD3		C30C11.2	JA	Lva	Lva
	rpn-5	PSMD12		F10G7.8	JA	WT	WT
	rpn-6.1	PSMD11		F57B9.10	MV	Lva	Lva
	rpn-7	PSMD6		F49C12.8	JA	Lva	Lva
	rpn-8	PSMD7		R12E2.3	MV	Lva	Lva
	rpn-9	PSMD13		T06D8.8	JA	WT	Rbs, Emb, Bli, Lva and Lvl (F1)
	rpn-10	PSMD4		B0205.3	JA	WT	WT
	rpn-11	PSMD14		K07D4.3	MV	Rbs, Ste	Rbs, Ste
	rpn-12	PSMD8		ZK20.5	MV	WT	WT
	rpn-13	Rpn13/Adrm1		C56G2.7	MV	WT	WT
	nfm-1	NF2	FERM domain-containing protein	F42A10.2	MV	WT	WT
	cep-1	TP53	Cystein proteinase superfamily protein. Transcription factor	F52B5.5	MV	WT	WT
	cdk-4	CDK4	Cyclin-dependent kinase 4	F18H3.5	JA	WT	WT
	abl-1	ABL1	Tyrosine-protein kinase	M79.1a	MV	WT	WT
	akt-2	AKT2	Serine/threonine-protein kinase	F28H6.1	MV	WT	WT
	scd-2	ALK	ALK tyrosine kinase receptor homolog	T10H9.2	JA	WT	WT
	swsn-7	ARID2	SWI/SNF nucleosome remodeling complex component	C08B11.3	JA	WT	WT
	atm-1	ATM	Serine/threonine-protein kinase	Y48G1BL.2	JA	WT	WT
	ubh-4	BAP1	BRCA1-associated protein 1 homolog. UCH	C08B11.7	JA	WT	WT
	brc-2	BRCA2	DNA repair protein associated	T07E3.5	MV	WT	WT
	sli-1	CBL	SH3 domain binding activity, receptor tyrosine kinase binding activity and ubiquitin protein ligase activity	M02A10.3	MV	WT	WT
	cye-1	CCNE1	G1/S-specific cyclin-E	C37A2.4	MV	Emb, Rbs	Emb, Rbs
	hmp-2	CTNNB1	β-catenin-like protein	K05C4.6	JA	WT	WT
	let-23	EGFR	Receptor protein-tyrosine kinase	ZK1067.1	JA	WT	WT
	vab-1	EPHA3	Ephrin receptor 1 activity and protein domain specific binding activity	M03A1.1	JA	WT	WT
	sel-10	FBXW7	F-box/WD repeat-containing protein with homodime-rization activity and protein kinase binding activity	F55B12.3	JA	WT	WT
	egl-15	FGFR1	Myoblast growth factor receptor with protein kinase activity	F58A3.2	JA	WT	WT

Malignant mesothelioma-related genes	***daf-2***	IGF1R	Insulin-like receptor subunit β with PTB domain binding activity; SH2 domain binding activity; and protein kinase binding activity	Y55D5A.5	JA	WT	WT
	ver-1	KDR	Is predicted to haveransmembrane receptor protein tyrosine kinase activity	T17A3.1	JA	WT	WT
	ver-3			F59F3.1	JA	Rbs	Rbs
	ver-4			F59F3.5	JA	WT	WT
	set-16	KMT2A	Histone-lysine N-methyltransferase	T12D8.1	JA	WT	WT
	let-60	KRAS	Ras protein. Exhibits GTP binding activity and enzyme binding activity	ZK792.6	MV	WT	WT
	F10D7.5	MDM2	NHR domain-containing protein	F10D7.5a/c	JA	WT	WT
	F11E6.8	MET	Tyrosine kinase	F11E6.8	JA	WT	WT
	mxl-3	MAX	BHLH domain-containing protein. Exhibits DNA-binding transcription factor activity and RNA polymerase II regulatory region DNA binding activity	F46G10.6	MV	WT	WT
	nmy-2	MYH9	Exhibits calmodulin binding activity and protein kinase binding activity	F20G4.3	JA	Rbs, Emb	Rbs, Emb
	gap-2	DAB2IP	Ras GTPase-activating protein	ZK899.8	JA	WT	WT
	aap-1	PIK3R2	Phosphoinositide kinase AdAPter subunit	Y110A7A.10	MV	WT	WT
	ptc-1	PTCH	SSD domain-containing proteins	ZK675.1	JA	WT	WT
	ptc-3			Y110A2A_54.d	JA	Ste	Ste
	rho-1	RHOA	Ras-like GTP-binding protein rhoA	Y51H4A.3	MV	Lva, Lvl, Ste	Lva, Lvl, Ste
	rict-1	RICTOR	RICTOR-V domain-containing protein. Is predicted to have enzyme activator.	F29C12.3	MV	WT	WT
	sox-2	SOX2	HMG box domain-containing protein	K08A8.2	MV	WT	WT
	trt-1	TERT	Telomerase reverse transcriptase	DY3.4	JA	WT	WT
	vhl-1	VHL	Is predicted to have ubiquitin protein ligase activity	F08G12.4	MV	WT	WT
	klf-2	WT1	Kruppel-Like Factor (zinc finger protein). Is predicted to have DNA-binding transcription factor activity, RNA polymerase II-specific	F53F8.1	JA	WT	WT
	fust-1	EWSR1	Is predicted to have RNA binding activity and metal ion binding activity	C27H5.3	JA	WT	WT
	chr-1	CREB1	Exhibits transcription coactivator binding activity	Y41C4A.4	MV	WT	WT
	sftb-1	SF3B1	Essential for developmentIs predicted to have mRNA binding activity. Is involved in negative regulation of gene expression	T08A11.2	JA	Ste, Lva	Ste, Lva
	apr-1	APC	Adenomatous polyposis coli protein-related protein 1. Exhibits beta-catenin binding activity and protein N-terminus binding activity	K04G2.8	MV	Emb	Emb
	brc-1	BRCA1	Exhibits ubiquitin protein ligase activity	C36A4.8	MV	WT	WT
	him-6	BLM	Exhibits 3'-5' DNA helicase activity and enzyme binding activity	T04A11.6	JA	WT	WT
	daf-16	BMPR1A	Exhibits 14-3-3 protein binding activity; DNA-binding transcription factor activity; and enzyme binding activity	F29C4.1	MV	Emb	Emb
	xpd-1	ERCC2	Helicase ATP-binding domain-containing protein. Is predicted to contribute to RNA polymerase II CTD heptapeptide repeat kinase activity	Y50D7A.2	JA	Rbs	Rbs
	xpb-1	ERCC3	Is predicted to contribute to RNA polymerase II CTD heptapeptide repeat kinase activity	Y66D12A.15	JA	Ste	Ste
	xpf-1	ERCC4	ERCC4 domain-containing protein. Exhibits enzyme binding activity	C47D12.8	JA	WT	WT

Cancer-related genes	***xpg-1***	ERCC5	Is predicted to have 5'-3' exodeoxyribonuclease activity; 5'-flap endonuclease activity; and crossover junction endodeoxyribonuclease activity.	F57B10.6	MV	WT	WT
	egrh-2	EGR1, EGR3	Is predicted to have DNA-binding transcription factor activity, RNA polymerase II-specific	Y55F3AM.7	JA	WT	WT
	egrh-1			C27C12.2	JA	WT	WT
	rib-1	EXT1	Exhibits enzyme binding activity	F12F6.3	JA	WT	WT
	rib-2	EXT2	Exhibits enzyme binding activity and heparan sulfate N-acetylglucosaminyltransferase activity	K01G5.6	MV	WT	WT
	fcd-2	FANCD2	Is predicted to have DNA polymerase binding activity	Y41E3.9	MV	WT	WT
	fum-1	FH	Probable fumarate hydratase. Is predicted to have fumarate hydratase activity	H14A12.2a	MV	WT	WT
	flcn-1	FLCL	Folliculin C domain-containing protein. Is predicted to contribute to GTPase activator activity.	F22D3.2	JA	WT	WT
	cdc-73	HRPT2	Cell division cycle protein 73. Is predicted to have RNA polymerase II complex binding activity	F35F11.1	MV	WT	WT
	sma-4	MADH4	Dwarfin sma-4;MH2 domain-containing protein. Is predicted to have DNA binding activity and metal ion binding activity	R12B2.1	MV	Emb	Emb
	mlh-1	MLH1	DNA mismatch repair protein. Is predicted to have ATPase activity	T28A8.7	JA	WT	WT
	msh-2	MSH2	DNA mismatch repair protein. Is predicted to contribute to DNA binding activity and MutLα complex binding activity	H26D21.2	MV	WT	WT
	msh-6	MSH6	DNA mismatch repair protein. Is predicted to contribute to DNA binding activity and MutLα complex binding activity	Y47G6A.11	MV	WT	WT
	pms-2	PMS1, PMS2	PMS (Post Meiotic Segregation) family. Is predicted to have ATPase activity	H12C20.2a	MV	WT	WT
	kin-2	PRKAR1A, PRKAR1B	cAMP-dependent protein kinase regulatory subunit. Is predicted to have 3',5'-cyclic-GMP phosphodiesterase activity and cAMP-dependent protein kinase regulator activity	R07E4.6	JA	Dpy, Bli, Egl, Ste	Dpy, Bli, Egl, Ste
	daf-18	PTEN	Phosphatidylinositol 3,4,5-trisphosphate 3-phosphatase and dual-specificity protein phosphatase. Exhibits protein tyrosine phosphatase activity	T07A9.6	MV	WT	WT
	lin-35	RB1, RB2	Exhibits protein C-terminus binding activity	C32F10.2	JA	WT	WT
	sbds-1	SBDS	Ribosome maturation protein	W06E11.4	MV	WT	WT
	sdhb-1	SDHB	Succinate dehydrogenase [ubiquinone] iron-sulfur subunit. Is predicted to have iron-sulfur cluster binding activity and ubiquinone binding activity	F42A8.2	MV	Emb	Emb
	mev-1	SDHC	Succinate dehydrogenase cytochrome b560 subunit. Is predicted to have electron transfer activity; heme binding activity; and succinate dehydrogenase (ubiquinone) activity.	T07C4.7	MV	Emb	Emb
	cey-1	SDHD	CSD1 domain-containing protein Is predicted to have nucleic acid binding activity.	F33A8.5	MV	WT	WT
	snfc-5	SMARCB1	SNF chromatin remodeling Complex component. bfamily b, member 1). Is predicted to have transcription coactivator activity	R07E5.3	MV	Ste, Pva	Ste, Pva
	smo-1	SUMO1	Small ubiquitin-related modifier	K12C11.2	MV	Rbs, Emb	Rbs, Emb
	fshr-1	FSHR, LHCGR	Is predicted to have G protein-coupled peptide receptor activity	C50H2.1	JA	WT	WT
	wrn-1	WRN	Exhibits 3'-5' DNA helicase activity.	F18C5.2	MV	WT	WT
	xpa-1	XPA	XPAC domain-containing protein. Is predicted to have damaged DNA binding activity	K07G5.2	MV	WT	WT
	xpc-1	XPC	Is predicted to have damaged DNA binding activity and single-stranded DNA binding activity	Y76B12C.2	JA	WT	WT

	paxt-1	NKRF	Partner of xrn-2 protein 1	R05D11.6	MV	WT	WT
Putative BAP1 interactors	***zip-11***	BATF3	BZIP domain-containing protein. Is predicted to have RNA polymerase II proximal promoter sequence-specific DNA binding activity	W08E12.1	MV	WT	WT
	fos-1	FOSL1, FOSL2	Exhibits several functions, including enzyme binding ctivity; identical protein binding activity; and transcription factor binding activity	F29G9.4	MV	Ste, Pva	Ste, Pva
	brd-1	BARD1	BRCA1-associated RING domain protein 1. Exhibits ubiquitin protein ligase activity	K04C2.4	MV	WT	WT
	T16G1.9	EIF3K	ANK_REP_REGION domain-containing protein	T16G1.9	MV	WT	WT
	hat-1	HAT1	Hat1-N domain-containing protein. Is predicted to have H4 histone acetyltransferase activity and histone binding activity.	M03C11.4	JA	WT	WT
	hcf-1	HCF1	Exhibits transcription factor binding activity	C46A5.9	JA	WT	WT
	itr-1	IP3R1	Inositol 1,4,5-trisphosphate receptor	F33D4.2	JA	Ste	Ste
	amx-1	KDM1B	Amine oxidase family member 1. Exhibits histone demethylase activity (H3-dimethyl-K4 specific)	R13G10.2	JA	WT	WT

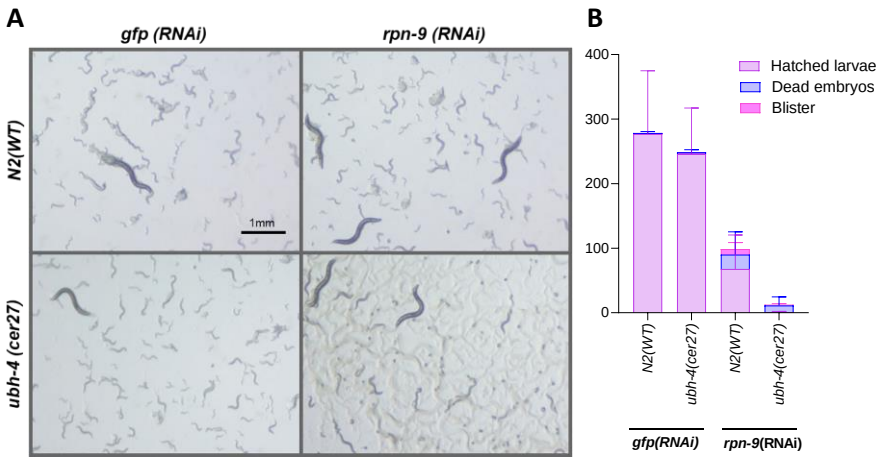

Figure 17: Phenotypic effect of *rpn-9(RNAi)* treatment. A. Representative images of reduced brood size in *ubh-4(cer27)* background after 120 hours *rpn-9(RNAi)* treatment (20°C). **B.** Graph shows the quantification of hatched larvae, dead embryo and blister animals under different RNAi conditions. Statistics were performed by one-way ANOVA (Krustal-Wallis and Dunn's tests). $p<0.01$ comparing hatched larvae between WT and cer27 under *rpn-9(RNAi)*. No significant differences were found among the other observed phenotypes. An average of 20 animals were scored. Experiment was performed once.

6. Characterization of RPN-9 expression using a translational endogenous reporter

6.1. Generation of *rpn-9* endogenous reporter by one-shot Nested CRISPR

The synthetic interaction between *ubh-4* and *rpn-9* suggested a cooperation role between both genes, probably on proteasome-dependent proteostasis. Given the ubiquitous UBH-4 expression through *C. elegans* body, we wondered in

which tissues both UBH-4 and RPN-9 signals could co-detected. For that purpose, we introduced the wrmScarlet fluorescent tag in the *rpn-9* C-terminus by one-shot Nested CRISPR, meaning that the ssODN from step 1 and the PCR product from step 2, were injected together in a single step. With this strategy, PCR product insertion is resulted at lower efficiencies (5% editing efficiency in this case). Scoring was performed by visual screening under fluorescence microscope. Microinjection was made in the UBH-4::EGFP background, thus generating the double endogenous translational reporter CER620: *ubh-4(cer68[ubh-4::EGFP]) rpn-9(cer203[rpn-9::wrmScarlet]) II*.

6.2. *ubh-4* and *rpn-9* are ubiquitously expressed during *C. elegans* development

Once generated the double reporter, *in vivo* observation under fluorescence microscopy was performed to describe the expression pattern of *rpn-9*. **Figure 18** shows *ubh-4::EGFP* (top panel), *rpn-9::wrmScarlet* (middle panel) and merge (bottom panel). As could be expected, both *ubh-4* and *rpn-9* are ubiquitously expressed, showing similar expression patterns at both cellular and tissue levels.

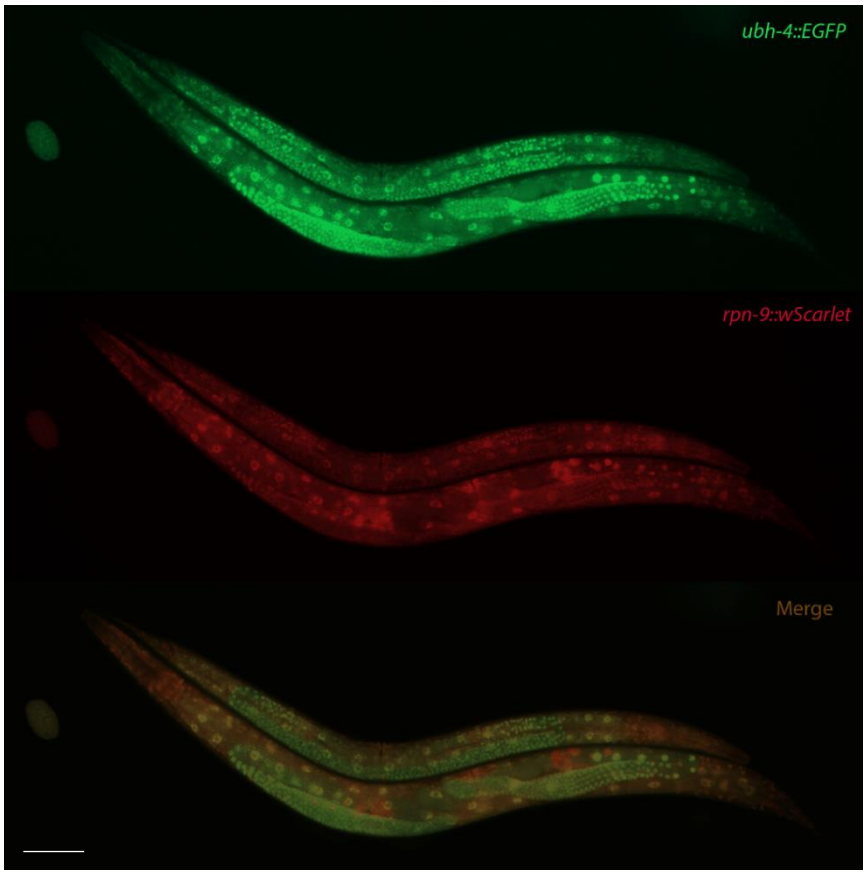

Figure 18: Expression pattern of *ubh-4* and *rpn-9*. Representative images of animals co-expressing *ubh-4::EGFP* and *rpn-9::wrmScarlet* at different stages (young adult, adult and embryo). *ubh-4::EGFP*, *rpn-9::wrmScarlet* and merge signals can be visualized in top, middle and bottom panels, respectively. Scale bar represents 100 µm.

7. Generation of *rpn-9* and *ubh-4* double mutants

To further investigate the genetic interaction between *rpn-9* and *ubh-4* in a more robust way, we generated double mutants

for each of the *ubh-4* mutant alleles in a *rpn-9* mutant background. The *rpn-9* mutant was provided by the Caenorhabditis Genetics Center (CGC). Since *rpn-9* and *ubh-4* locus are both located at the chromosome II, the double mutants were produced by CRISPR/Cas9 on *rpn-9(gk401)* background. *cer140*, *cer198* and *cer195* alleles were generated by using same CRISPR/Cas9 reagents as employed for *cer27*, *cer32* and *cer25*, respectively (**Materials and Methods 3**). Since *rpn-9(gk401)* causes sterile hermaphrodites, only heterozygous animals were microinjected to generate the new *ubh-4* alleles (**Figure 19**). Heterozygous animals are balanced with *mIn1* construct, carrying an integrated pharyngeal GFP element, allowing the identification of dim GFP-positive pharynx for microinjection and for strain maintenance. To simplify, we will refer to *cer150, cer198* and *cer195* alleles as (-), A87D and F73V, respectively.

Figure 19: Double mutants' diagrams. Schematic representation of *C. elegans* chromosome II, showing *rpn-9(gk401)* (black) and *ubh-4(-)* (colored) mutant alleles (*gk401*, *cer140*, *cer198* and *cer195*) and mIn1 construction (grey). Green shadow marks heterozygous animals used for microinjection and double mutants' generation. Genotypes are detailed below each chromosomal scheme, and phenotypes (given by either gk401 or mIn1 construction) are detailed at the bottom of the Figure. Figure created with Biorender.com.

7.1. *ubh-4* deletion and A87D substitution cause additively reduced body length in *rpn-9* mutant background

Once double mutants were generated, phenotypical characterization at different temperatures was performed to further study *ubh-4* and *rpn-9* genetic interaction. Interestingly, although *rpn-9* simple mutant is statistically smaller than wild-type animals, this phenotype is additively stronger in combination with both *ubh-4* deletion and A87D (**Figure 20A** and **B**). In both cases, animals reach adulthood and all the body structures seems to be properly developed (microscopically visualized), except for the intestine and the germline. One of the reason for *rpn-9* displaying a reduced body length may be an undeveloped germline, and such effect might be incremented in double mutants.

A

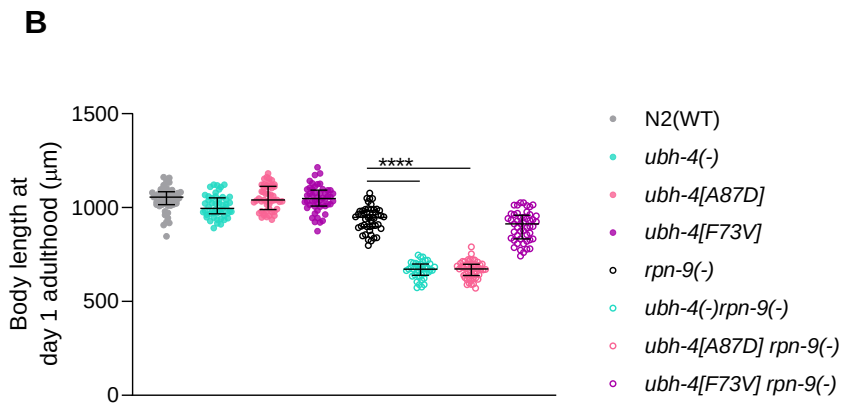

Figure 20: Double and simple mutants' body length. A Representative images showing reduced body length in simple and double *ubh-4 rpn-9* mutants. Pictures were taken at day 1 of adulthood growth at 15°C. Scale bar represents 0.5 mm. **B.** Graph shows the body length quantification in WT, simple and double mutants. Bars represent median and interquartile range and dots the length values of individual animals. The same experiment was performed three times, measuring an average of 100 animals per replicate. **** mean p<0,0001. Statistics were analyzed by one-way ANOVA (Krustal-Wallis and Dunn's tests).

7.2. *ubh-4* deletion and A87D substitution present a significant decline in *C. elegans* survival

To further describe the *ubh-4 rpn-9* functional interaction, double mutants were carefully monitored through its lifespan at 15ºC and 20ºC. Surprisingly, there was a dramatically decrease in the double mutant's median survival compared to controls in both *ubh-4(-)* and *ubh-4[A87D]* genetic backgrounds (**Figure 21**). Bigger differences were observed at 15ºC rather than at 20ºC. These data suggest an *ubh-4 rpn-9* synthetic lethal effect on *C. elegans* lifespan, which is strongly

pronounced at 15ºC, meaning that the cooperative role is temperature dependent. In addition, these data support that cancer-related substitution A87D has a detrimental effect on protein function in *rpn-9* KO background.

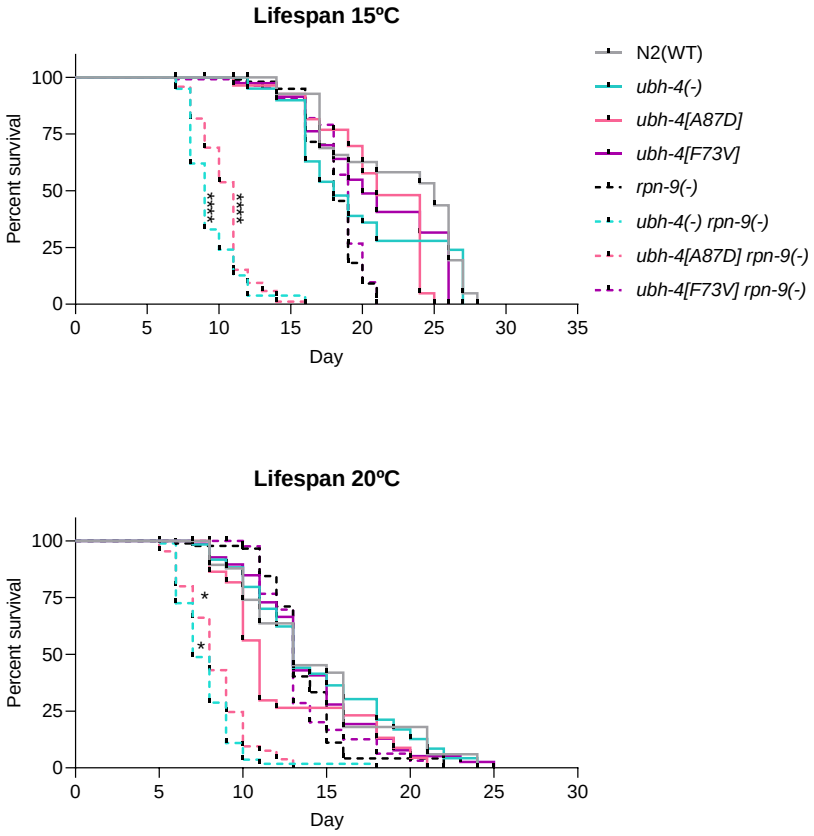

Figure 21: Survival curves at 15ºC and 20ºC. Survival curves of WT, *ubh-4* and *rpn-9* simple and double mutants. Percent survival is indicated for each allele. An average of 80 animals were censored through two independent experiments for lifespan analysis at both temperatures. Statistical analysis by Log-rank (Mantel-Cox) test were performed to compare *rpn-9(gk401)* and double mutants. * and **** mean $p<0.1$ and $p<0.0001$, respectively.

8. *ubh-4 rpn-9* double mutants display germline developmental arrest

Since distinct *ubh-4* mutants (- and A87D) together with *rpn-9(-)* displayed developmental abnormalities and sterility, we asked whether any additive or synergistic effect on germline development occur on those animals.

To further analyze the functional interaction between *ubh-4* and *rpn-9* in the germline, nuclei were observed after DAPI staining in *ubh-4* simple and double mutants. Gonads were dissected out gonads followed by DAPI staining at day one of adulthood at 15ºC (**Material and Methods 18**). Comparing *rpn-9(-)* and double mutants with WT and *ubh-4* simple mutants, we can stand out: (i) differences in germline sizes, due to fewer germline nuclei, being noticeably exacerbated in *ubh-4(-)* background, (ii) an absence of the regular nuclei-phase hallmark through the germline (**Figure 22B**) and, (iii) the impossibility to reach diakinesis meiotic phase thus preventing oocyte production (**Figure 22A** and **B**). All these features that evidence a germline developmental arrest in *rpn-9* knockout are emphasized particularly in combination with *ubh-4* deletion allele, and probably, germ cell proliferation is also affected in these double mutants.

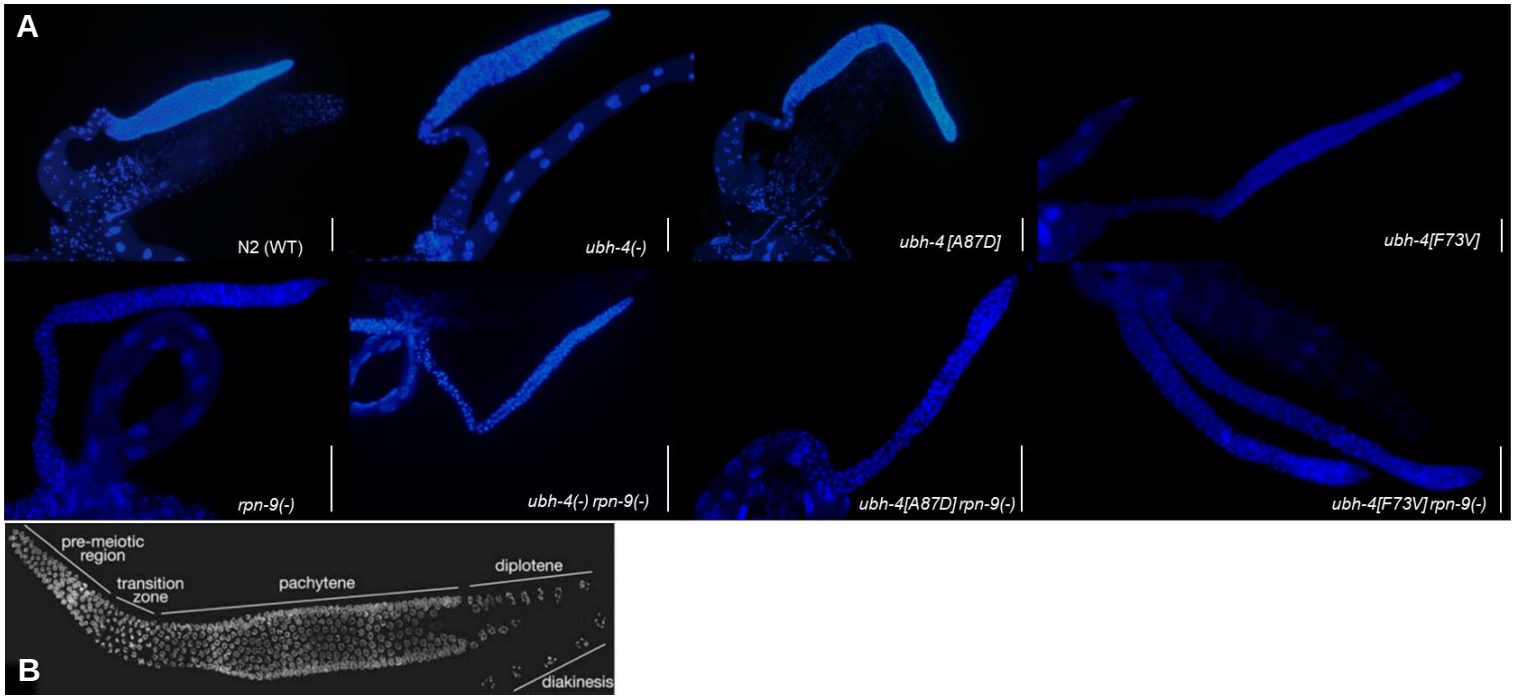

Figure 22: DAPI-stained nuclei in gonads at day one adulthood. A. Dissected out and DAPI-stained gonads from WT, simple and double *ubh-4* and *rpn-9* mutants. Scale bars represent 125 µm. **B.** WT DNA marked in gonad stained with DAPI allows the identification of meiotic prophase stages by the chromatin morphology (modified from Phillips, McDonald, and Dernburg 2009).

9. UBH-4 participation in the ubiquitin-mediated proteostasis in the germline

9.1. Chromosomes fail to attach to the cytoskeleton in *ubh-4* mutants

A hallmark of chromosomal tethering is the formation of foci on the nuclear envelope through ZYG-12, by association to microtubule-associated dynein in the cytoplasm. Proteasome has been related to this chromosomal movements in the meiotic prophase (Introduction 7.2.2). To investigate if UBH-4 is implicated in chromosomal tethering we examined the localization pattern of the dynein heavy chain DHC-1 in alive worm germlines using a GFP reporter fusion. For that purpose, we genetically crossed single mutants for ubh-4 with DHC::GFP reporter. DHC-1::GFP formed distinct foci on the nuclear envelope in transition and early pachytene regions of wild-type (Figure 23, top panel). Interestingly, no foci are formed in none of the *ubh-4* mutants, indicating that chromosome ends fail to attach to the cytoskeleton and suggesting an abnormal proteasome activity in these worms. This is intriguing and further experiments will be required to clarify this phenotype since *dhc-1* is an essential gene, but *ubh-4* mutants do not display severe phenotypes in terms of progeny.

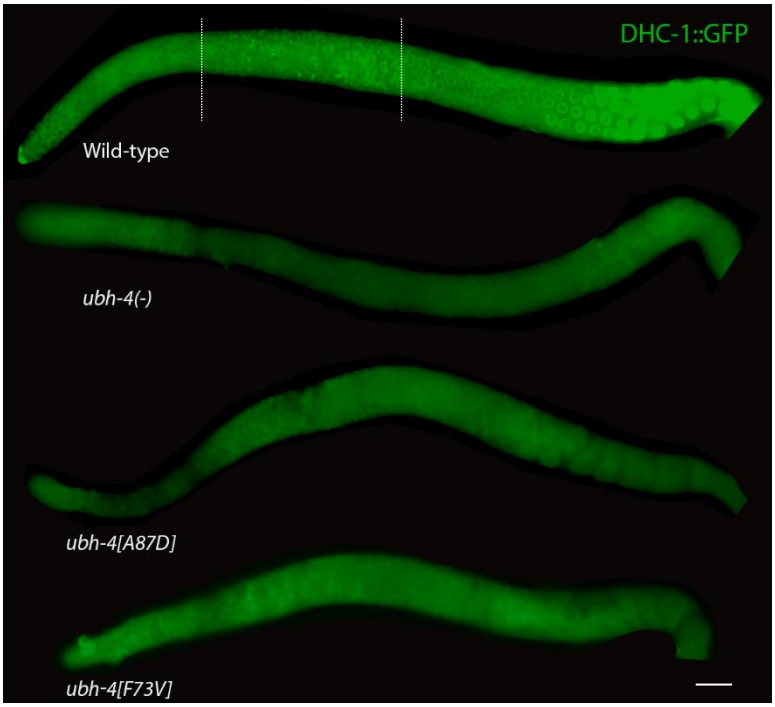

Figure 23: Chromosome ends fail to attach to the cytoskeleton in *ubh-4* mutants. Representative images showing DHC-1::GFP expression pattern in distinct genetic backgrounds. Vertical lines delineate regions of distinct foci, only visible in wild type. The same exposure time was applied when imaging all the animals. Scale bar represents 20 µm.

9.2. *ubh-4* compromises proteasome activity throughout the germline

Since UBH-4 is a deubiquitinating-related enzyme associated to UPS, we decided to evaluate the proteasome activity in the *C. elegans* germline. To do so, we used a transgenic line that expresses a non-hydrolysable version of ubiquitin fused to a

GFP reporter and histone H2B (UbG76V::GFP::H2B) in the germline. The UbG76V mutant form of ubiquitin has been extensively used as a reliable sensor of proteasome activity in both *C. elegans* somatic and germ cells (Hamer et al., 2010; Kumar and Subramaniam, 2018).

Here, we used UbG76V::GFP::H2B expressed in the germlines under the *pie-1* promoter and *drp-1* 3′ UTR (Kumar and Subramaniam, 2018). We first crossed *ubh-4* mutants with the UbG76V::GFP::H2B strain and fluorescent signal was observed in living animals under the microscope. In wild-type germlines, UbG76V::GFP::H2B tag was practically absent, and the only low signal that could be detected was in the proximal gonad due to the absence or low proteasome activity in the oocyte nuclei (Kumar and Subramaniam, 2018) (**Figure 24**). Interestingly, *ubh-4* depletion leads to an accumulation of UbG76V::GFP::H2B throughout the germline, including in the first embryonic stages. Curiously, this observation is more prevalent in animals grown at 25ºC, suggesting that proteasome-based protein degradation may be temperature dependent (data not shown). However, no increment in UbG76V::GFP::H2B signal was observed in A87D or F73V mutants. These data suggest that complete depletion of *ubh-4* negatively affects ubiquitin-mediated protein degradation in the *C. elegans* germline. More experiments are necessary to obtain quantitative data of this reporter in the distinct backgrounds including the double mutants.

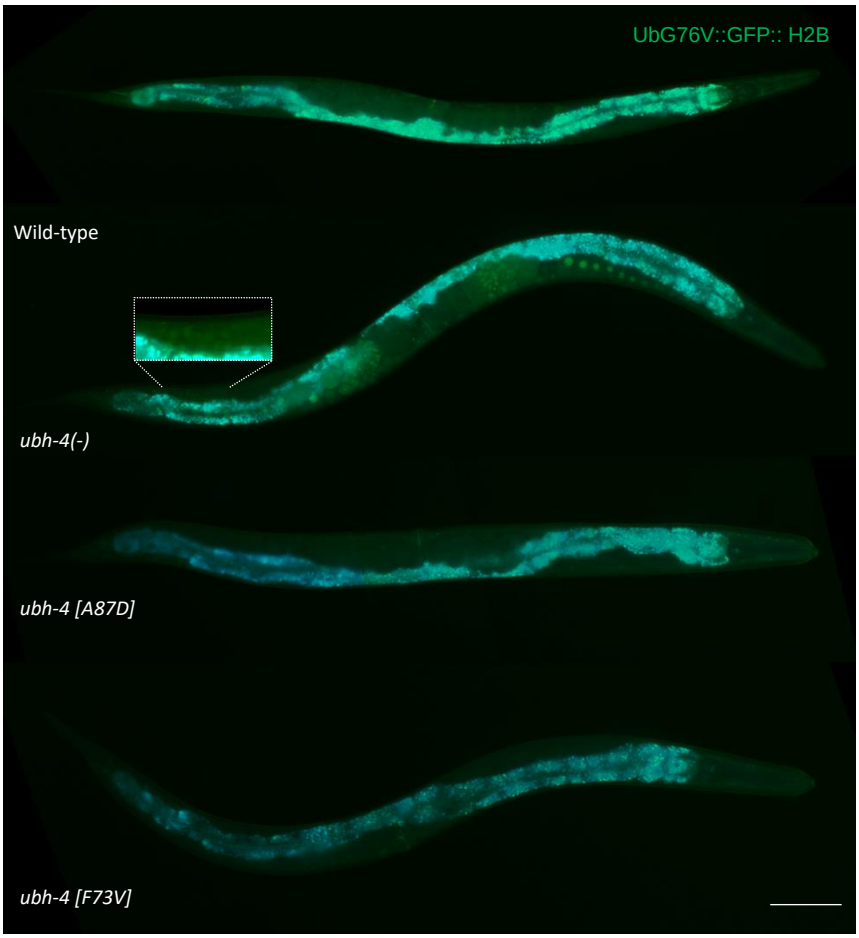

Figure 24: UBH-4 is required for ubiquitin-mediated protein degradation in the germline. Representative images of adult animals grown at 25ºC showing absence or presence of UbG76V::GFP::H2B in different genetic backgrounds. The white square stands out a magnification of the distal germline in *ubh-4(-).* Scale bar: 100 µm.

RESULTS

PART II: Cisplatin and metabolism

1. High glucose diet sensitizes *C. elegans* to cisplatin in a dose-dependent manner

With the aim to investigate whether hyperglycemic conditions influence the cisplatin-based chemotherapy in diabetic patients (Bergamino et al., 2019), we adapted the glucose-mediated toxicity method in *C. elegans* established in Schlotterer et al., 2009. We treated synchronized wild-type L1 population with cisplatin and different glucose concentrations to achieve diabetic hyperglycemic levels in *C. elegans* (10-15 mM) (Schlotterer et al., 2009). Our data show that high glucose diet does not affect *C. elegans* development but when co-administered with cisplatin, higher glucose concentrations sensitizes the animals to the drug arresting them at initial larval stages. Interestingly, low glucose supplementation slightly protects the animal from the drug effects (**Figure 25**).

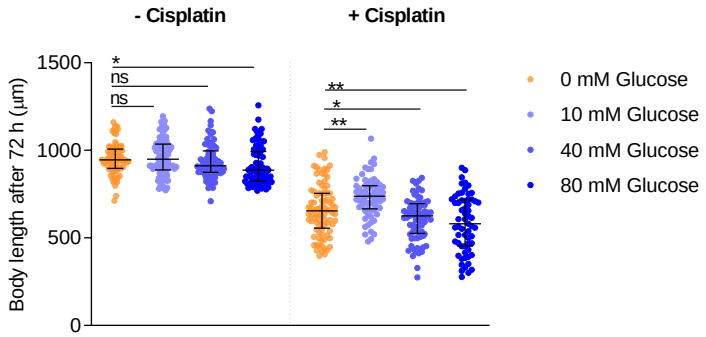

Figure 25: Glucose supplementation in. Graph plots animals body length 72-hours post seeding L1 animals at 20ºC, fed with different glucose concentrations, and exposed to either 0 or 60 µg/mL cisplatin. Bars indicates median and interquartile range and dots bod length values of

individual animals. Two independent experiments were performed, and each condition was measured in duplicates, analyzing 50 animals per condition. *, ** and ns mean $p<0.1$, $p<0.01$ no significant, respectively. Statistics were analyzed by ordinary one-way ANOVA (Holm-Sidak's test).

2. Lipid metabolism is implicated in the systemic response to cisplatin

Intricated metabolic networks tightly coordinate the flow of sugars and fats through synthesis, storage, and breakdown pathways. Interestingly, our published transcriptomic data from cisplatin-exposed population (García-Rodríguez et al. 2018), highlighted a set of deregulated genes indicating metabolic, carboxylic acid concentration and skin physiology abnormalities. Classification of these genes based on GO terms (Ashburner et al., 2000) shows that most of them overlap in these three categories, suggesting a possible connection between carboxylic acid metabolism, cuticle composition and cisplatin toxicity (data not shown).

To investigate the link between cisplatin and fat metabolism we first performed lipid staining of treated or untreated worms with Sudan Black. We observed that cisplatin treatment produced a huge increase of fatty acid droplets in wild-type cisplatin-exposed animals (**Figure 26A**). Then, to check if such metabolic alteration confers some systemic protection to the drug, we disrupted one of the key fatty acid synthesis regulatory factors, *C. elegans sbp-1* (SREBP-1c in humans), using two different alleles *sbp-1(ep176)* and *sbp-1(ep79).* The

weak allele *ep176* carries an unknown genomic alteration while the strong allele *ep79* is a 2181-bp deletion. Both alleles produce reduced body length in adulthood and low-fat content compared to wild-type animals (Nomura et al., 2010). Synchronized L1 populations exposed to 60 µg/mL cisplatin for 72 hours showed a significant reduction of *sbp-1(ep79)* body length compared to both wild-type and weak *sbp-1* allele (**Figure 26B**). All these data indicate that fatty acid synthesis and storage is stimulated by cisplatin and that such metabolic switch confers protection to the animal.

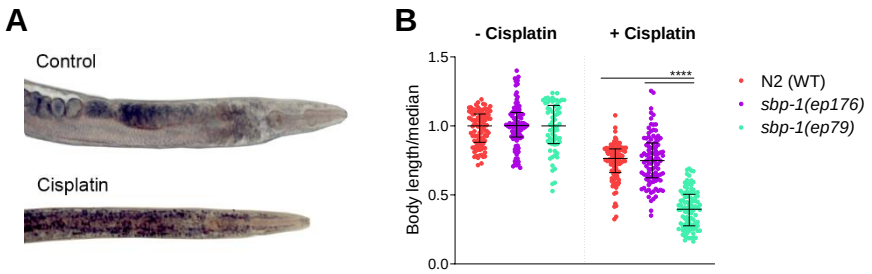

Figure 26: Systemic response of *sbp-1* mutants against cisplatin. A. Representative images of Sudan Back staining of wild-type animals in the absence or presence of 60 µg/mL cisplatin. Bigger amount of lipid droplets (back dots) is observed in cisplatin-treated worm compared to control one (untreated). **B.** Effect of cisplatin on the body length of wild-type and *sbp-1* mutant animals. Dots represents normalized body length of individual animals with respect to the median of each control group. Experiments were performed in triplicates. **** indicates $p<0.0001$. Statistics was performed by one-way ANOVA (Krustal-Wallis and Dunn's tests).

3. Cisplatin instigates mitochondrial dysfunction

3.1. The alternative BH3-only protein CED-13 protects from the consequences of mitochondrial dysfunction presumably produced by cisplatin-induced mtROS

In García-Rodríguez et al. 2018, we described that the BH3-only protein CED-13 has a protective role from cisplatin exposure during *C. elegans* larval development suggesting that and alternative role of CED-13 in this context. Similarly, a protective response to mitochondrial ROS (mtROS) through BH3-only CED-13 protein, instead of promoting apoptosis, has been previously described in *C. elegans* by Yee and colleges in 2014. To unravel if such protective effect of CED-13 against cisplatin was due to cisplatin-induced mitochondrial ROS, we exposed two different *ced-13* mutant alleles to both cisplatin and superoxide generator paraquat (PQ) (as positive control to mtROS inductor).

For that purpose, we used a PQ dose (0.1 mM) high enough to provoke a significantly reduced body length but allowing the detection of a possible cisplatin-modulator effect. Interestingly, we noted that low doses of PQ in wild-type animals (0.01 and 0.05 mM) seem to confer a protective response to PQ-induced mtROS (**Figure 27A**). Subsequently, using a mild toxic PQ dose (0.1 mM), we observed shorter animals in a *ced-13* mutant background, being *ced-13(tm536)* the most sensitive

(**Figure 27B**). In addition, PQ induced an additive detrimental effect to cisplatin, and such effect was further increased in both *ced-13* deletion alleles (**Figure 27B**). Based on these results and taking into account that CED-13 expression is relevant in response to mtROS (Yee et al., 2014), we suggest a protective role of CED-13 in cisplatin-induced mtROS. However, the additive effect of cisplatin and paraquat may reflect distinct mechanisms by which CED-13 induces a protective response.

3.2. Cisplatin stimulates mitochondrial unfolded protein response (mtUPR)

To corroborate if cisplatin therapy affects mitochondria we quantified the expression of *hsp-6,* one of the chaperones induced in response to misfolded or unasembled proteins within the mitochondria or when mitochondrial respiratory complexes are imbalanced. GFP fused to the *hsp-6* promoter is commonly used to evaluate the activation of the mitochondrial unfolded protein response (mtUPR) pathway (Jovaisaite et al., 2014). Thus, we quantified the relative fluorescence intensity (RFI), with respect to the background, of animals exposed or not to cisplatin during 48 hours from 34 hours after hatching. Our data showed a significant increase in the RFI in cisplatin-treated animals compared to untreated (**Figure 28**), suggesting that cisplatin is stimutaling mtUPR in *C. elegans*.

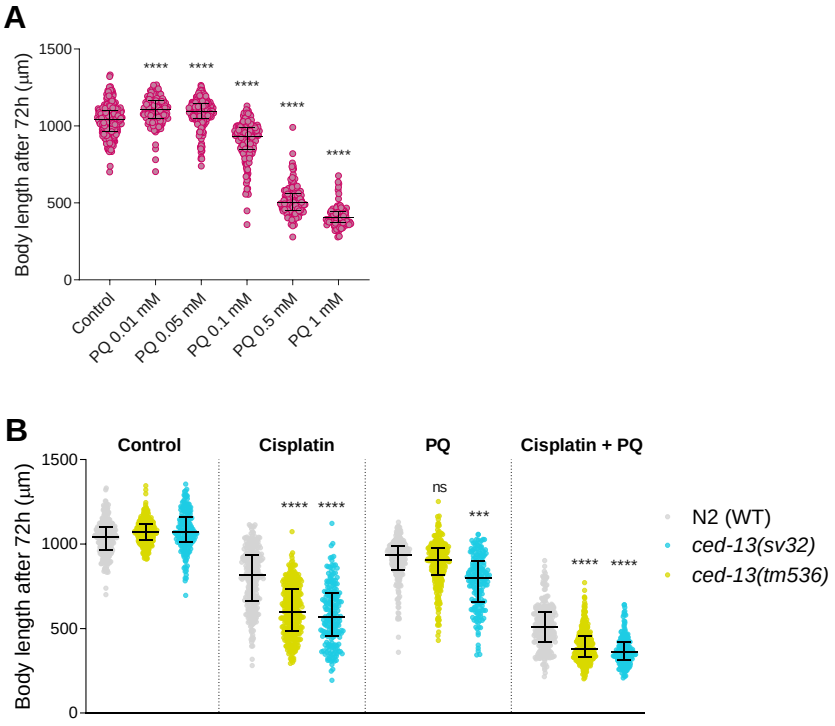

Figure 27: Effect of cisplatin and paraquat on *ced-13* mutants. A. Dose-response curve showing paraquat effect on wild-type animals' body-length. **B.** The additive effect of cisplatin and PQ is further increased in *ced-13* mutants (*sv32* and *tm536*). Statistics were analyzed by one-way ANOVA (Krustal-Wallis and Dunn's tests). ***, **** and ns mean, $p<0.001$, $p<0.0001$ and non-significant, respectively, compared to wild-type in the same drug condition.

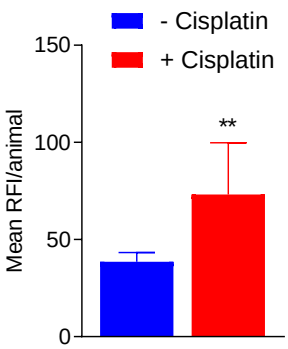

Figure 28: HSP-6p::GFP intensity in cisplatin-treated and untreated animals. Columns represent the RFI mean of two independent experiments (twenty animals per experiment) and bars the standard deviation. Statistics were performed using Student's t-test, ** means $p<0.01$.

4. Cisplatin induces abnormal mitochondrial respiration

The disruption of stoichiometric balance between components of mitochondrial respiratory complexes (OXPHOS complexes I, III, IV and V) is one of the inputs that causes UPR^{mt} activation. Since we previously demonstrated that cisplatin induces the UPR^{mt} pathway, we hypothesized that OXPHOS complexes imbalance could be one of the consequences from cisplatin-induced toxicity.

To check this, we proceed to assess mitochondrial respiration using the Seahorse eXF96 respirometer. First, following the protocol described by Koopman et al. 2016, we optimized the procedure to our cisplatin conditions **Materials and Methods 10**. In addition, paraquat and glucose supplementation were used as mitochondrial damaging and mitochondrial respiration decreasing compounds, respectively. Thus, synchronized wild-type L1 animals were seeded in either control or treated plates for 24h at 20ºC, prepared as described in **Materials and Methods 4**. After this time, oxygen consumption rate (OCR) was measured in animals at L3 stage. It is crucial that none of the tested animals exceeded the L3/L4 molt otherwise a substantial difference in mitochondrial load would exist between younger and older animals (Luz et al., 2015; Tsang and Lemire, 2002).

OCR was measured with the Seahorse eXF96 respirometer after disrupting mitochondrial respiration, at different levels, affected by two drug injections: carbonyl cyanide-4-(trifluoromethoxy)phenylhydrazone (FCCP) and sodium azide (**Figure 29** and **30A**). First, FCCP injection disrupts the mitochondrial membrane potential and thus ATP synthesis while still allowing proton pumping, electron transport and oxygen consumption. Consequently, administration of FCCP results in the collapse of the mitochondrial membrane potential, inducing a rapid increase in both energy and oxygen consumption without ATP generation. FCCP injection can be used to calculate the maximal and the spare respiratory capacity of worms, being the last the quantitative difference between the initial basal OCR and the maximal uncontrolled OCR (**Figure 30A**). Finally, injection of sodium azide blocks both cytochrome c oxidase (complex IV) and the ATP synthase (complex V), thereby shutting down the whole electron transport chain. Non-mitochondrial respiration can be distinguished from mitochondrial respiration by injecting sodium azide (**Figure 30A**). Nevertheless, basal respiration provides the most readily interpretable number from an eXF96 experiment.

We observed that cisplatin *per se* significantly decreases basal respiration. Likewise, glucose and paraquat also compromise the basal respiratory capacity (**Figure 30B** and **C**). Interestingly, a higher OCR reduction is observed in cisplatin groups combined with either glucose or paraquat. However,

such differences are not statistically significant, suggesting that these compounds may be affecting mitochondrial respiration through the same target or different one but provoking similar effects (**Figure 30B** and **C**). Is also important to note that FCCP fails in increase OCR in cisplatin groups, being the spare capacity practically non-existent (**Figure 30B and D**). Finally, cisplatin *per se* and in combination with glucose, generates a significant reduction in the mitochondrial respiration compared to non-treated group (**Figure 30E**).

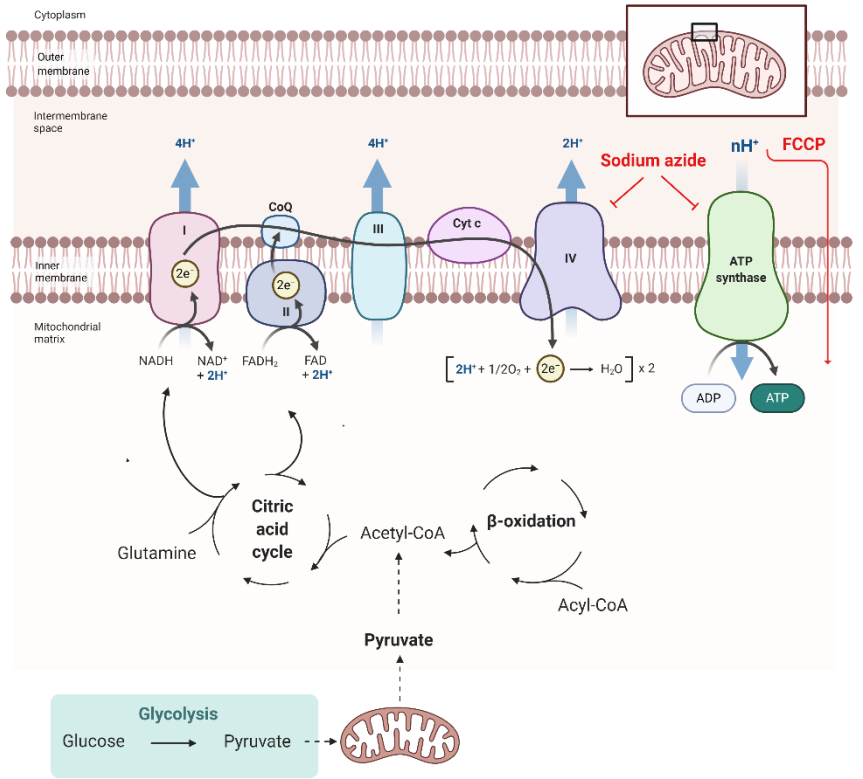

Figure 29: Overview of glycolysis and oxidative phosphorylation. Pyruvate is generated in the cytosol via glycolysis. Then, is translocated through the intermembrane to the mitochondrial matrix. In multiple model

organisms, increasing the glucose content causes a shift from oxidative phosphorylation towards glycolysis. This results in a decreased OCR, as oxidative phosphorylation requires the consumption of O_2. In red, sodium azide which inhibits complexes IV and V in *C. elegans* and FCCP, which is an uncoupler reagent and transfers H+ back to the mitochondrial matrix without generating ATP.

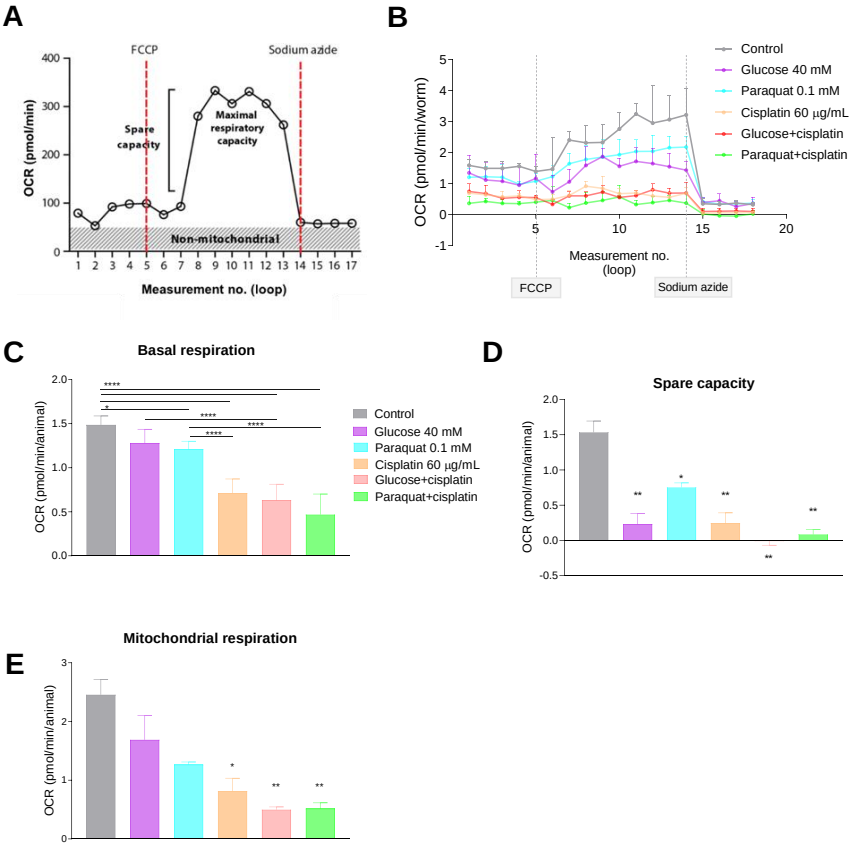

Figure 30: *C. elegans* respirometry in larval stage A. Typical OCR *C. elegans* respirometry profile in adult worms. Modified from Koopman et al. 2016. **B.** OCR profile of *C. elegans* L3. Connected points represent the median of the measures of each condition at a given loop and bars represent standard deviation. Discontinuous lines indicate FCCP and azide injections, respectively. Median and interquartile range are represented by

bars and error bars, respectively, for basal respiration (**C**), spare capacity (**D**) and mitochondrial respiration (**E**). Even if there are statistical differences between control and treated conditions, spare capacity values should not be comparable because differences in basal respiration exist. Experimental details are described in **Materials and Methods 4** and **10**. One-way ANOVA (Holm-Sidak's and Dunn's tests) were used to compare statistical differences between groups **** $p<0.0001$, ** $p<0.01$, * $p<0.1$. Data were analyzed using Agilent Seahorse XFe96 Analyzer, Seahorse Wave Desktop software and GraphPad Prism 8.0.

RESULTS

PART III: Cisplatin and behavior

1. *C. elegans* catechol-*O*-methyltransferase family

1.1. Homology between *C. elegans* COMT members

As I previously introduced (**Introduction 8**), eukaryotic catechol-*O*-methyltransferases (COMTs) is a family of enzymes that catalyze the degradation of catecholamines. *C. elegans* COMT family presents five members (*comt-1* to *comt-5*), all containing the catechol-*O*-methyl transferase domain. Since human COMT gene encodes for two similar isoforms, S-COMT and M-COMT, with 100% sequence similarity but with different subcellular localization, BLAST alignment was performed using the S-COMT reference sequence. BLAST analysis based on protein sequence shows that human COMT shares high sequence similarity with *C. elegans* COMT members (**Figure 31**). Interestingly, most of the binding sites for S-COMT ligands (S-adenosyl-L-methionine, Mg^{2+}, and substrate) are conserved or partially conserved along all the *C. elegans* COMTs, suggesting that human COMT functional role is maintained. COMT-4 possesses the highest percentage identity per query cover (**Table 4**) being the closets homolog of human COMT.

We have recently demonstrated the *C. elegans* feasibility as a model organism to investigate cellular mechanisms to cisplatin chemoresistance (García-Rodríguez, et al. 2018). Interestingly, we found *comt-4* transcript upregulated upon 24-

hour drug exposure thus, suggesting a potential role as modulator of cisplatin response. Moreover, *comt-4* has been related to the degradation of catecholamines, affecting dopamine- and serotonin-dependent effects (Rodríguez-Ramos et al. 2017). Considering all the above, we were interested in further study the catechol methyltransferase activity of *C. elegans* COMT family in cisplatin induced cytotoxicity.

Figure 31: Homology between human S-COMT and *C. elegans* COMT proteins. Scheme of COMT-1 to -5 and S-COMT protein sequences (black lines) and conserved residues (purple bars). Alignments were illustrated with CLC Sequence Viewer 8.0.

Table 4: BLASTP analysis of *C. elegans* COMT family members.

Protein	Query cover (%)	Identity (%)
COMT-4	77	36.9
COMT-3	17	74.47
COMT-2	17	76.60
COMT-5	17	65.96
COMT-1	63	22.45

2. Expression levels of *C. elegans* COMT genes vary upon cisplatin exposure

2.1. Quantitative real-time PCR analyses reveal an increased transcript levels of *comt-3, comt-4* and *comt-5* in animals exposed to cisplatin

In order to investigate the functional role of *C. elegans* COMT members in cisplatin-induced neurotoxicity. Despite the nervous system development is largely complete by the end of the L1 stage, some developmental changes are clearly coordinated with the L4/adult molt. In addition, some behavioral features are sensitive to animal stage. So to avoid life stage bias, we will chose those COMT members higher expressed at postembryonic stages. Based on the expression profile provided by GExplore 1.4 interface (Hutter and Suh, 2016), *comt-3*, *comt-4* and *comt-5* were the genes that met the criteria (**Figure 32A-C**).

Quantitative real-time PCR analysis was performed in animals treated with cisplatin 60 µg/mL for 24 hours. Worms were exposed to the drug at different developmental stages (**Figure 32D**) and the relative fold change compared to non-treated groups was calculated and normalized to control genes (**Materials and Methods 12**). We found that *comt-3*, *comt-4*, and *comt-5* expression levels were slightly increased when animals were exposed to cisplatin in a mix population and

L2/L3 stages. These data suggest that not only *comt-4* would be relevant in cisplatin response, but also *comt-3* and *comt-5*.

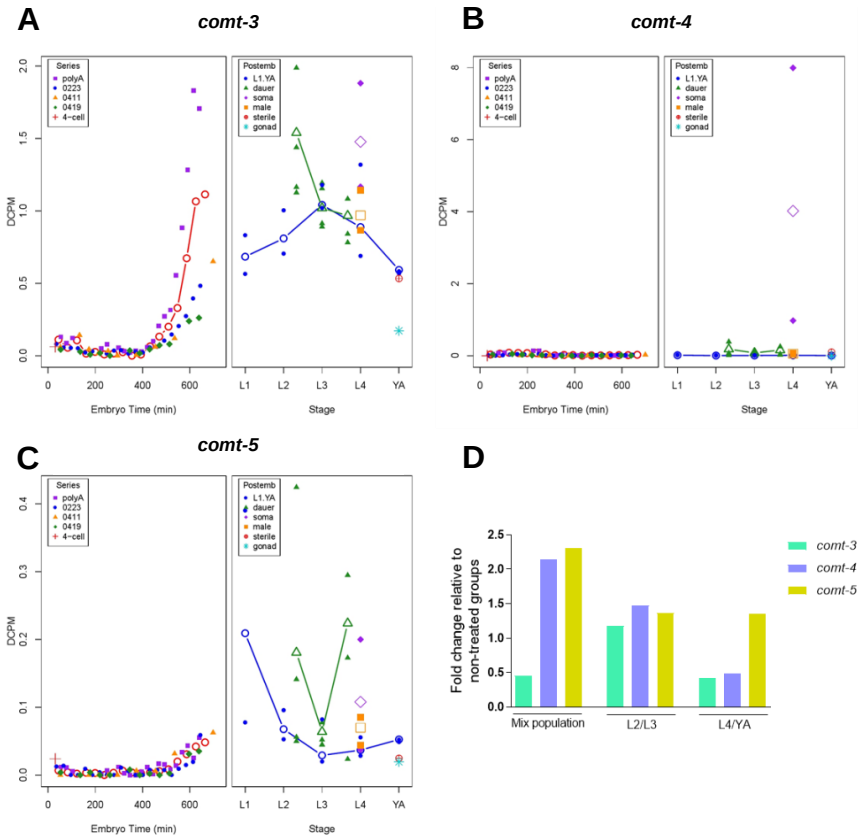

Figure 32: *comt-3*, *comt-4*, *comt-5* expression levels. Expression pattern by developmental stage, presented as the average depth of coverage per million mapped reads (DCPM) (note the different scale values), are shown for *comt-3* (**A**), *comt-4* (**B**), and *comt-5* (**C**) (data provided by GExplore 1.4.). **D.** Fold-change expression of indicated genes in animals exposed to cisplatin relative to non-treated groups at different time points.

2.2. Generation of *comt-4* transcriptional endogenous reporter by Nested CRISPR

In order to further investigate the COMT-4 localization and expression pattern *in vivo*, we generated two different transcriptional endogenous reporters by Nested CRISPR (Vicencio et al., 2019). With this method, as we previously mention for translational endogenous reporter generation (**PART I**, **Results 3**), we were capable of efficiently insert long DNA fragments, such as mCherry and EGFP::H2B sequences, in two steps. In this case, in the first step, we used an ssDNA donor (≤200 bp) to simultaneously remove the *comt-4* coding sequence and insert the 5' and 3' fragments of the corresponding fluorescent sequence in the *comt-4* endogenous locus. The second step was performed in the same manner as for translational reporters. (**Materials and Methods 3**). As a result, we generated the strains CER423: *comt-4(cer101[comt-4p::mCherry]) V* and CER554: *comt-4(cer157[comt-4p::EGFP::H2B]) V***.**

Based on the COMT-4 expression profile provided by GExplore platform, COMT-4 is expressed in non-seam hypodermis and socket cells at L2 stage (**Figure 33A**) which is consistent with the fluorescent signal observed in *comt-4(cer157[comt-4p::EGFP::H2B])* adults (**Figure 33B**). Additionally, we also observed signal in the intestinal cells. However, *comt-4(cer101[comt-4p::mCherry])* does not display a clear, reproducible nor stable signal throughout the animal

life cycle in different generations. Only mild florescent signal in the head could be detected (data not shown). Differences between both approaches suggest that the accumulation of the fluorescent signal in the nuclei, forced by the H2B tag, is necessary to study expression pattern of genes expressing at low level as *comt-4*.

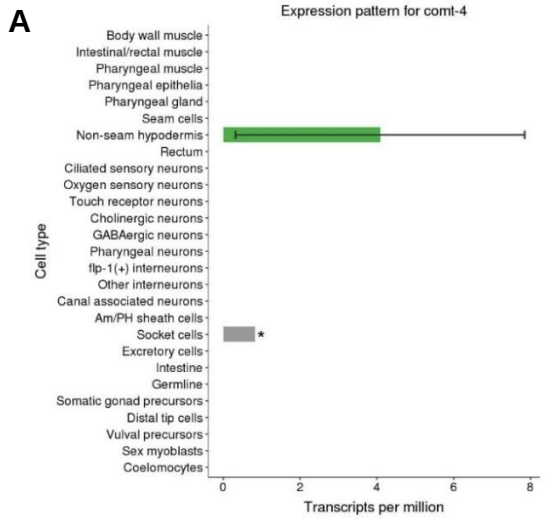

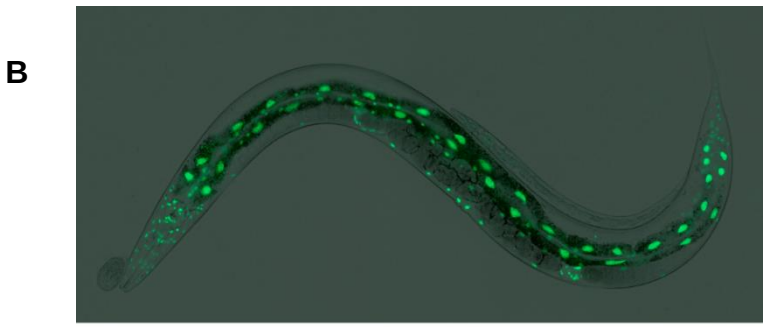

Figure 33: COMT-4 expression pattern. A. Expression pattern for COMT-4 at L2 stage based on GExplore. **B.** *comt-4(cer157[comt-4p::GFP::H2B])* nuclear signal in an adult animal.

3. Using CRISPR/Cas9 to generate *comt-3*, *comt-4* and *comt-5* null alleles

comt-4 and *comt-5* encode a single transcript, Y40B10A.6 and Y40B10A.7, respectively. In contrast, two different transcripts are encoded by *comt-3*, Y40B10A.2a.1 and Y40B10A.2b.1, differing in 247-nucleotides (**Figure 34A**). After the successful deletion and editing of *comt-4* mentioned above (from Nested CRISPR step 1), we decided to follow a similar strategy for *comt-3* and *comt-5* (**Results 2.2**, **Material and Methods 3**). Molecular designs for these edits are illustrated in **Figure 34B,** and sequences needed to generate these alleles are detailed in **Materials and Methods 3**. Thus, three null mutants (*comt-3 (cer130[comt-3p::egfp::h2b 1-3)V*, *comt-4(cer128[comt-4p::egfp::h2b 1-3])V and comt-5(cer126 [comt-5p::egfp::h2b 1-3])V*) were produced, and none of them displayed overt phenotypic defects.

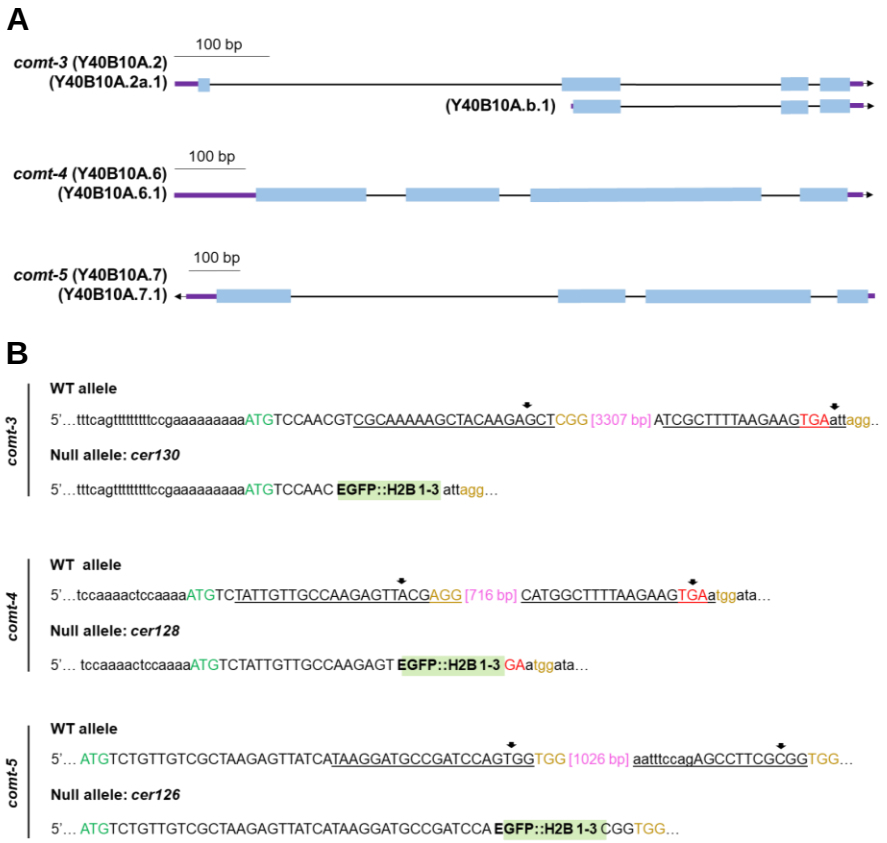

Figure 34: *comt-3*, *comt-4* and *comt-5* loci and null allele molecular designs. A. Schematic representation of *comt-3*, *comt-4* and *comt-5* transcripts. Introns are shown by black lines, 5´and 3´UTRs (untranslated regions) by purple bars and exons by light blue bars. **B.** Sense strand sequences of wild-type and null alleles (*cer130, cer128* and *cer126*) produced by homology-directed repair after CRISPR/Cas9 edition for each locus. Start and stop codons are represented in green and red letters, respectively. PAM sequences are shown in yellow. 3´and 5´crRNA sequences are underlined and cut sites are shown by black arrows. The resulting deletion lengths are represented in pink and EGFP::H2B fragments 1 and 3 are represented by green shadow. Partial 5' and 3' UTR sequences are indicated in lowercase.

4. Characterization of dopamine-dependent effects in COMT null mutants

The CRISPR/Cas9-generted alleles, *cer130*, *cer128* and *cer126*, were subjected to different analyses in order to evaluate their influence in dopaminergic and serotoninergic signaling. It has been previously demonstrated that some dopamine- and serotonin-dependent effects are altered when *comt-4* is overexpressed in neuroligin-deficient mutants (Osuna-Luque et al. 2018; Rodríguez-Ramos et al. 2017). **Table 5** shows the phenotypic responses analyzed in this study classified according to the type of neurotransmitter signaling.

Table 5: Analyzed phenotypes classified by neurotransmitter signaling.

Dopamine-dependent	Serotonin-dependent
Body length	Egg laying
Brood size	Pharyngeal pumping
Egg laying	
Basal slowing resposnse (BSR)	
Gentle touch response	

4.1. *comt-5* deletion allele present reduced body length

It is known that body length is negatively regulated by dopamine (Nagashima et al., 2016). Here, we used the null *cat-2* allele *n4547* as positive control for dopamine altered effects. *cat-2* encodes a tyrosine hydroxylase required for dopamine synthesis, and its depletion causes reduced levels of dopamine but still keeping some dopaminergic signaling activity (Sanyal et al., 2004).

Synchronized animals were grown for 96h at 20ºC and the body length of individual animals were measured. As we expected, *cat-2(n4547)* dopamine-defective animals were significantly longer than wild-type animals. In contrast, *comt-5(cer126)* and triple mutant, which combines *comt-3*, *comt-4* and *comt-5* deletion alleles, were significantly shorter than wild-type (**Figure 35**). However, no significant differences were observed between those. These observations suggest that *comt-5* has a relevant role in dopamine catabolism, to a greater extent than both *comt-3* and *comt-4*, since in mutants for these genes we observed the opposite effect to animals with low dopamine levels.

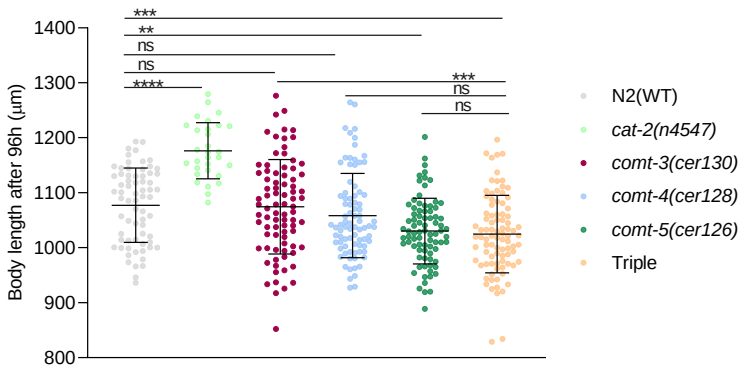

Figure 35: Effect on body length of the catechol-*O*-methyl transferase mutants. Dots represent measurement of individual animals from three independent experiments, and black lines depict median and interquartile range. Strains used in these experiments are simple deletion alleles for *comt-3*, *comt-4*, *comt-5*, triple mutant for those, and deletion allele for *cat-2*. Statistical significances was assessed by one-way ANOVA (Krustal-Wallis and Dunn's tests). **, ***, **** and ns mean $p<0.01$, $p<0.001$, $p<0.0001$ and no significant, respectively.

4.2. *comt-3(cer130), comt-4(cer128)* and *comt-5 (cer126)* have reduced brood size and egg laying rates

To further investigate if our COMT alleles modify phenotypes depending on dopamine signaling, brood size and egg laying rates were analyzed. In both assays, *cat-2(n4547)* was again used as control for altered dopamine levels. In brood size experiments, total viable progeny was counted in animals grown at 20ºC. Slightly reduced brood size was observed in *cat-2(n4547).* Interestingly, significantly reduced brood size was observed in *comt-3(cer130),* which was further reduced in

cat-2(n4547) background (**Figure 36A**). These data indicate a synergistic detrimental effect on dopamine signaling when *cat-2(n4547)* is combined with the absence of *comt-3*.

As indicated above (**Table 5**), egg laying rate in *C. elegans* is a catecholamine-dependent effect that may requires both dopaminergic and serotonergic signaling pathways (Sawin et al., 2000; Weinshenker et al., 1995). Interestingly, serotonin can bind the catechol substrate site of catecholamine-*O*-methyltransferase inhibiting its activity in humans (Tsao et al., 2012), and in *C. elegans comt-4* modulates serotonin-dependent effects when this protein is overexpressed (Rodríguez-Ramos et al. 2017). A slight reduction in egg laying rate was observed in *cat-2* mutant background, both alone and combined with *comt-3, -4* and *-5* null alleles, suggesting that disruption of dopamine signaling by catechol-*O*-methyltransferases is not sufficient to significantly affect egg lay phenotype. However, minor impairments, not statistically significant, in egg lay rate were observed in null mutants for *comt-3*, *comt-4* and *comt-5*, even in *cat-2(n4547)* background (**Figure 36B**).

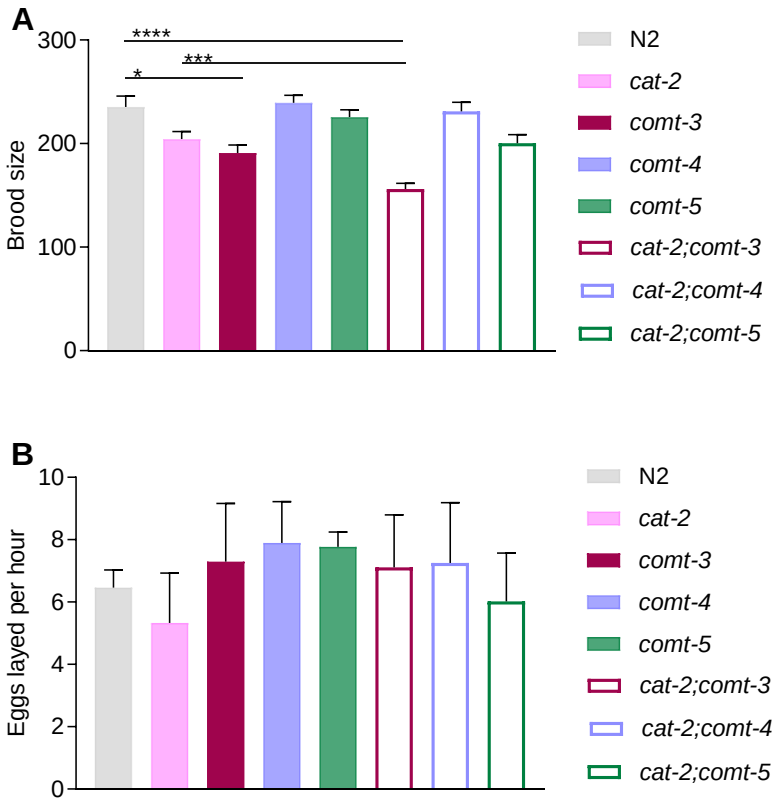

Figure 36: Characterization of brood size and egg lay phenotypes. A. Bars represent the brood size median and black lines interquartile range for each genotype. Significant reduced brood size is observed in *cat-2(n4547)* when combined with *comt-3* null allele. *, *** and **** mean $p<0.1$, $p<0.001$ and $p<0.0001$, respectively. **B.** Bars represent the median of eggs layed per hour and black lines indicates interquartile range. No significant differences were found. Statistics was performed one-way ANOVA (Krustal-Wallis and Dunn's tests).

4.3. Neither pharyngeal pumping rate, nor BSR, nor gentle touch response is affected in catechol-*O*-methyl transferase family mutants

Behavioral traits such as mechanosensation, pharyngeal pumping and locomotory rate of the nematode are also controlled by dopaminergic or serotonergic signaling (**Table 5**). Particularly, COMT-4 wild-type levels are needed to restore the mentioned behaviors in neuroligin-deficient mutants (Rodríguez-Ramos et al. 2017). We wanted to test, in our COMT mutant backgrounds, if these catecholamine-dependent effects are impaired and if there is a neurotoxic effect of cisplatin in this context.

For that purpose, gentle touch response, pharyngeal pumping rate and BSR were tested in the absence or presence of cisplatin. These experiments were scored by manual counting. No significant differences were found in *comt-3(cer130)*, *comt-4(cer128)* or *comt-5(cer126)* neither in control nor in cisplatin-exposed groups (data not shown).

5. Automated tracking of behavioral phenotypes

5.1. Multi-Worm Behavior Tracker

After many failed attempts to find an efficient method to study cisplatin-induced neurotoxicity in *C. elegans* using manual counting, we optimized a protocol with the aim to automatically track worms using the Multi-Worm Behavior Tracker (Javer et

al., 2018a). Such project combines the throughput of multi-worm tracking with the resolution of single worm tracking, allowing the extraction of detailed phenotypic fingerprints from a population. After recording animals at high resolution by a tracking hardware, the outline and skeleton of each animal are extracted, and then head-tail orientation is determined. The algorithm identifies dark particles on a lighter background or light particles on a darker background using adaptative thresholding and filtering particles by size. Finally, Tierpsy Tracker 2.0 was used to extract behavioral features data. Detailed information about this software can be found in the following repository:

http://ver228.github.io/tierpsy-tracker/docs/EXPLANATION.html

5.2. Cisplatin treatment produces dose-dependent reduction of path range in wild type animals

We started by optimizing which cisplatin condition led to an altered behavioral phenotype in adult wild-type animals. Since cisplatin causes larval arrest and sterility in a dose-dependent manner (García-Rodríguez et al. 2018), animals were exposed to different drug concentrations (100, 250 and 500 µg/mL) from L4 larval stage during different exposure times (4, 12 and 24 hours). After drug exposure, worms were transferred to tracking plates and recorded for 15 minutes (**Materials and Methods 8**). For each condition, triplicates were tested

analyzing a total of 30 animals per experiment. After processing the files, we looked for differential behavioral features.

Among all the tested conditions, only 24-hour cisplatin treatment leads to a significant decrease in the overall path range[3] compared to non-treated animals. This phenotype was dependent on drug-concentration, being the strongest at 500 µg/mL (**Figure 37**). However, most of the animals exposed to the highest cisplatin concentration died the day of the experiment so for successive tracking experiments, 24-hour of cisplatin 250 µg/mL were used. Thus, we stablished catechol.

5.3. *comt-4(cer128)* and comt-*5(cer126)* possess reduced path range mimicking dopamine-deficient mutants

With the aim to further characterize our catecholamine-*O*-methyltransferase mutant alleles we subjected them to the Multi-Worm Tracker System, proceeding with the stablished condition described in the previous section (**Results 5.2**), and looked for behavioral alterations. As a positive control of either dopamine-affected and locomotion-affected mutant, we used *cat-2(n4547)*.

[3] Path range is the distance of the worm's midbody from the path centroid measured in microns. Thus, it is a metric of worm displacement.

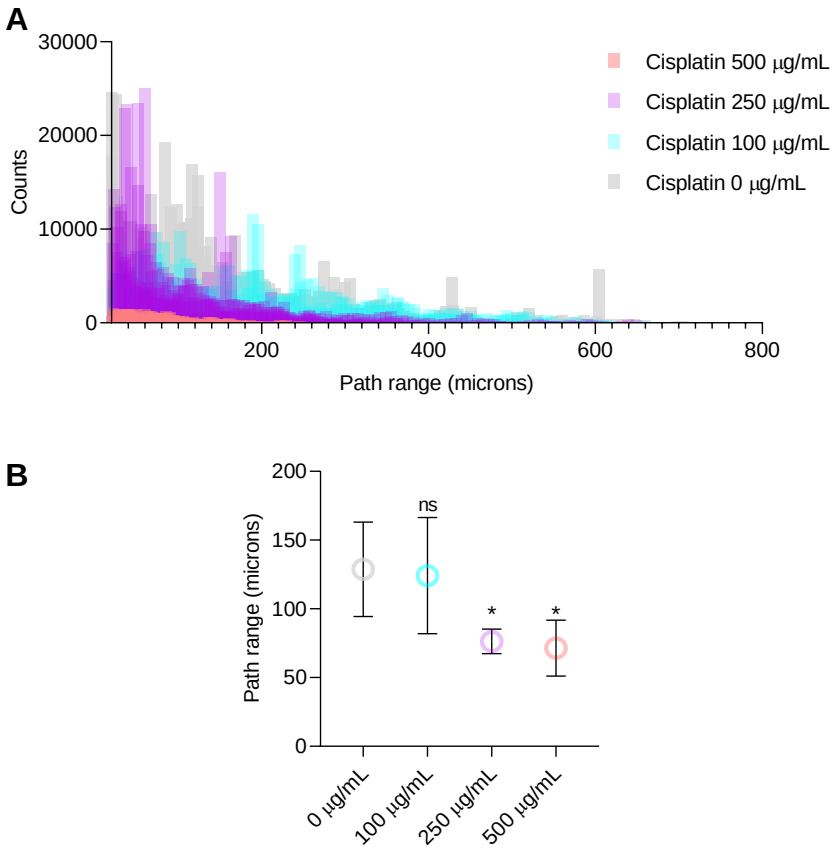

Figure 37: Dose-dependent effect of cisplatin on *C. elegans*' path range. A. Histogram of path range in wild-type animals treated with different cisplatin concentrations. **B.** Circles represent the mean path range of animals exposed to cisplatin; back lines represent standard deviation. The experiment was performed once. * and ns stand for p<0.01and not significant, respectively. Statistics was performed by one-way ANOVA (Krustal-Wallis and Dunn's tests).

Omura and colleges published that *n4547* showed impaired speed fluctuations compared to wild-type animals, evidencing that dopamine signaling is required for precise rates of locomotion in *C. elegans* (Omura et al., 2012). However, the 1007-nt deletion in *n4547* also affects the UTR of an additional locus, *pqn-85*. In fact, alterations of animal behavior when *pqn-85* is affected have been reported in the Open Worm Movement Database (Yemini et al., 2013). Therefore, in order to avoid genetic noise, we generated a new deletion allele for *cat-2, cer181[cat-2p::egfp::h2b1-3]]*, by CRISPR/Cas9 similarly as previously detailed for *comt-3* to *-5* (**Results 3**). In any case, we also included the *n4547* allele in the experiments.

For the tracking experiment, both *cat-2* alleles (*n4547* and *cer181*), catechol-*O*-methyltransferases mutants (*comt-3, comt-4, comt-5* and triple mutant) and N2 were subjected to path range analysis in control and cisplatin conditions. On the one hand, a significant reduction in covered distance compared to wild-type was evidenced in untreated conditions not only for *cat-2* mutants, but also for *comt-4* and *comt-5* deletion alleles (**Figure 38A** and **B**). However, minor decrease in path range were observed in *comt-3(cer130)* and triple mutant. On the other hand, path ranges were not altered in any mutant line under cisplatin exposure (**Figure 38B**).

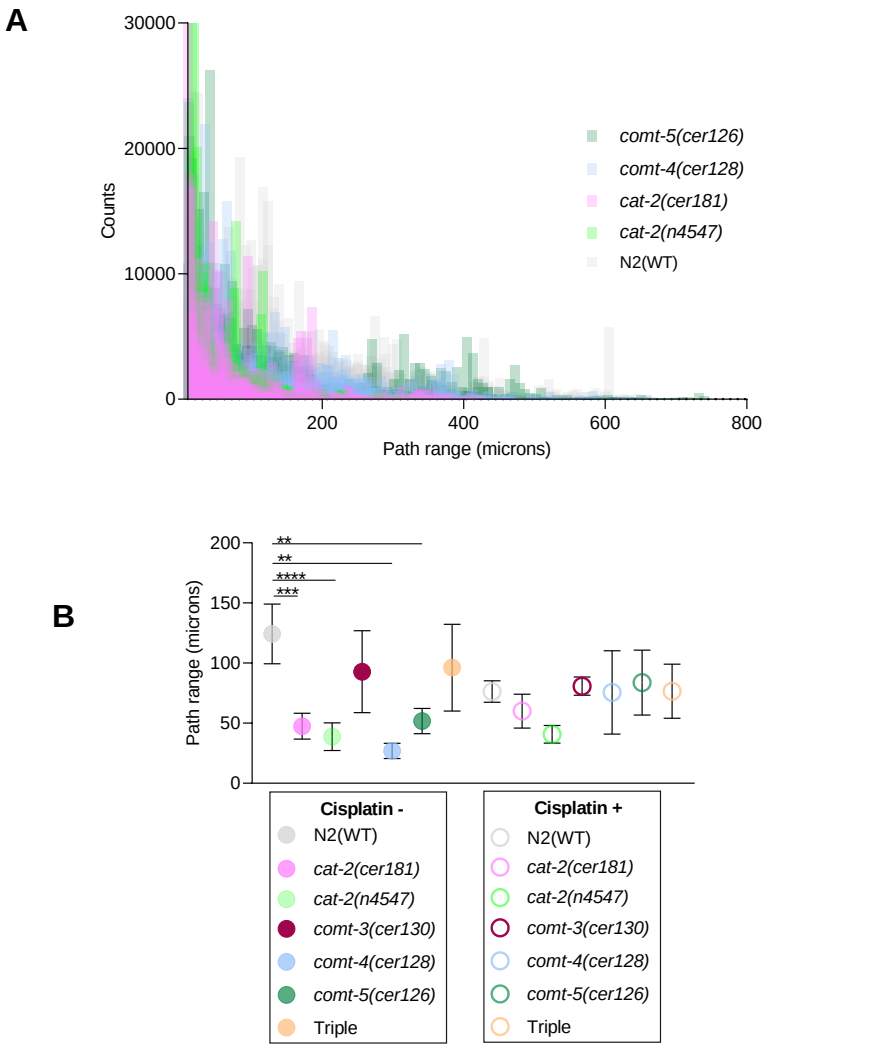

Figure 38: Path range analysis of catecholamine-*O*-methyltransferase and *cat-2* mutants. A. Histograms representing path range profile of wild-type, *comt-4*, *comt-5* and *cat-2* mutants in untreated conditions. **B.** Circles represent the mean path range of animals exposed to 250 µg/mL cisplatin or not (clear or filled circles, respectively), back lines represent standard deviation of two independent experiments. **, ***, **** mean $p<0.01$, $p<0.001$ and $p<0.0001$. Statistics was performed by one-way ANOVA (Krustal-Wallis and Dunn's tests).

5.4. Exogenous dopamine rescues cisplatin-induced path range alterations in wild-type animals and *cat-2* mutants

We have previously shown that dopamine-deficient mutants travelled shorter distances than animals with normal levels of this neurotransmitter (**Figure 38**). Such finding supports that dopamine metabolism may influence animal locomotion. Thus, we wondered if dopamine supplementation could rescue path range values in *cat-2* mutants to wild-type levels. To that end, we added to the worm culture media 0, 5 and 10 mM DA, for 24h before recording the tracking videos (**Materials and Methods 8**). Low dopamine supplementation (5 mM) was enough to increase *cat-2* mutants' path ranges up to wild-type values (**Figure 39**). However, 10 mM dopamine caused a significant reduction in path range values compared to non-supplemented animals in all genetic backgrounds (**Figure 39**).

In parallel, we co-treated animals with cisplatin and DA for 24h. Interestingly, 10 mM DA supplementation rescued cisplatin-induced neurotoxicity in wild-type animals (**Figure 39**). In addition, *cat-2* mutants recovered normal values of path range under 10 mM DA (**Figure 39**). Those findings suggest that cisplatin affects dopamine metabolism in *C. elegans*.

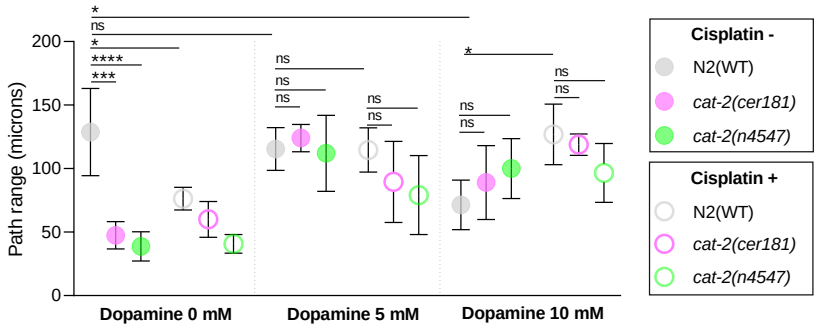

Figure 39: Dopamine influences path range animal behavior. Circles represent the mean path range of animals exposed or not to 250 µg/mL cisplatin, colored or clear circles respectively; black lines represent standard deviation. Dopamine concentration used in each data set is indicated at the bottom of the graph. Two biological replicates were performed. * ***, **** and ns means p<0.01, p<0.001, p<0.0001 and not significant, respectively. Statistics was performed by one-way ANOVA (Kruskal-Wallis and Dunn's tests).

5.5. Cisplatin alters *cat-2* mutant' posture

The Multi-worm Tracking System not only recovers locomotory features but also the range of shapes adopted by nematodes. In this section, we benefit from its high spatial and temporal resolution to extract the two-dimensional shape of *C. elegans* individuals from images of freely moving worms over long periods of time. The posture of the worm can be reconstructed as a summation of eigenworms or eigen projections. We consider six eigen projections (α_1- α_6) which can almost completely describe the natural worm posture by measuring the worm curvature (**Figure 40**). The dynamics along these eigenworms offer both a quantitative characterization of

classical worm movement such as forward crawling and measurement of more subtle behaviors such as pause states at particular postures.

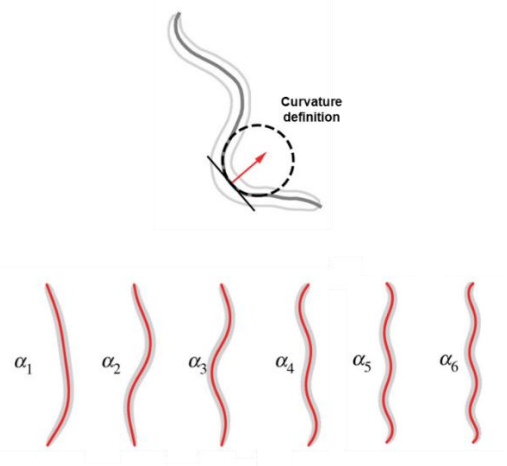

Figure 40: Describing the worm' shape. On top of the Figure, a worm diagram is illustrated, crossed by a line describing the shape. Curvature definition is given by the arc length function, represented by the red arrow. On the bottom, schematic representation of six eigen projections accounting for almost the entire variance in body shape (Modified from Javer, Ripoll-Sánchez, and Brown 2018).

Previously (**Results 5.3**), we have described that even if *cat-2* mutants *cer181* and *n4547* presented a reduced path range, they did not show further alterations under cisplatin exposure. Interestingly, 250 µg/mL cisplatin generates a dramatic postural change (**Figure 41**). In this line, eigen projections α_1-α_6 were analyzed to quantify and compare changes in the body curvature in different genetic backgrounds. Eigenworm profiles in **control** and **cisplatin** conditions can be found in **Figure 42A-F**, and the projected amplitudes (arbitrary units) for each eigenworm are graphically represented in **Figure 43A-F**. Even

if fluctuations in projected amplitudes could be observed through α_1 to α_6, major differences are present in both α_1 and α_2 for *cer181* when exposed to cisplatin. Curiously, we observed that cisplatin treated wild-types did not show eigenworm alterations. Suggesting that postural changes depend on dopamine. While α_1 and α_2 amplitudes are approximately 0 in N2, *cer181* possesses much larger amplitudes (α_1 ~ 2 and α_2 ~ 1). These values resemble projected amplitudes caused by neuronal injuries (Kunert et al., 2017). Thus, we stablished a model of neuronal damage induced by cisplatin based on *C. elegans* posture.

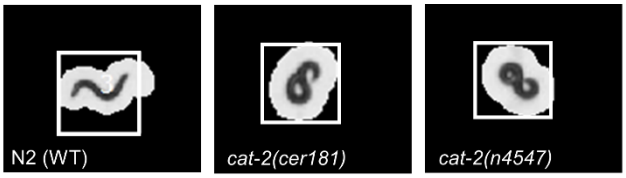

Figure 41: Posture alteration induced by cisplatin. Representative images of animals exposed to cisplatin visualized by Tierpsy Tracker 2.0.

5.6. Dopamine supplementation rescues wild-type-like postures in *cat-2* mutants exposed to cisplatin

We next tried to alleviate or even restore worm posture of cisplatin-exposed *cat-2* mutants by adding exogenous dopamine (**Materials and Methods 8**). We realized that 5 mM DA is sufficient to rescue the cisplatin-induced alteration on worm posture (**Figure 42** and **43**). In addition, in the absence

of cisplatin, DA cause minor fluctuations in α_2, α_3, α_4 and α_6 projected amplitudes in wild-type, and α_2, α_3, and α_6 in *cat-2* mutants. We deduce that (i) cisplatin is affecting worm curvature through fluctuations in dopamine signaling and (ii) that dopamine is a modulator of worm posture.

Figure 42: Eigenworm feature profile for dopamine-defective mutants. Eigen projections α_1 to α_6 (**A**-**F**) for wild-type and *cat-2* mutants (*cer181* and *n4547*) are represented by colored bars (grey, pink and green bars indicate wild-type, *cat-2(cer181)* and *cat-2(n4547)*, respectively), under different conditions detailed on the top of each graph. Bars represent the number of times a given projected amplitude value were counted during de record. Experiment was performed in two independent times.

Figure 43: Projected amplitude α_1- α_6 in dopamine-defective mutants. Graphs **A-F** show projected amplitudes for eigenworms 1-6, respectively. Circles represent the mean of two independent experiments and bars represent standard deviation. In A, color code is detailed. Yellow shadows point out the projected amplitude for wild-type animals in the absence of cisplatin nor dopamine. *, **, ns mean $p<0.1$, $p<0.01$ and not significant, respectively. Statistics were analyzed by one-way ANOVA (Krustal-Wallis and Dunn's tests).

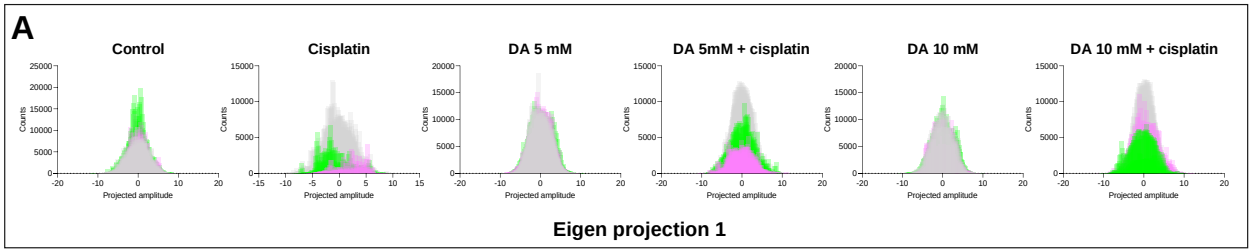
A
Control
Cisplatin
DA 5 mM
DA 5mM + cisplatin
DA 10 mM
DA 10 mM + cisplatin
Counts
Projected amplitude
Eigen projection 1

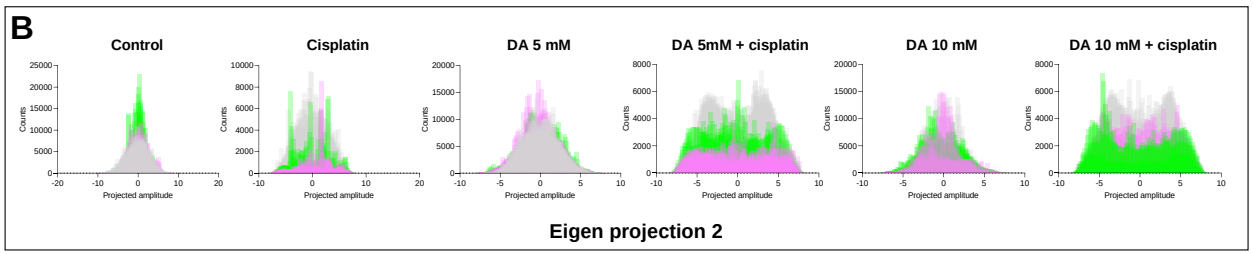
B
Control
Cisplatin
DA 5 mM
DA 5mM + cisplatin
DA 10 mM
DA 10 mM + cisplatin
Counts
Projected amplitude
Eigen projection 2

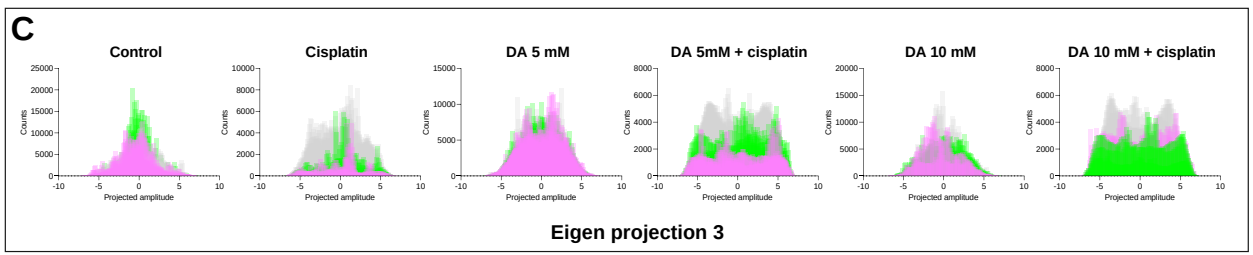
C
Control
Cisplatin
DA 5 mM
DA 5mM + cisplatin
DA 10 mM
DA 10 mM + cisplatin
Counts
Projected amplitude
Eigen projection 3

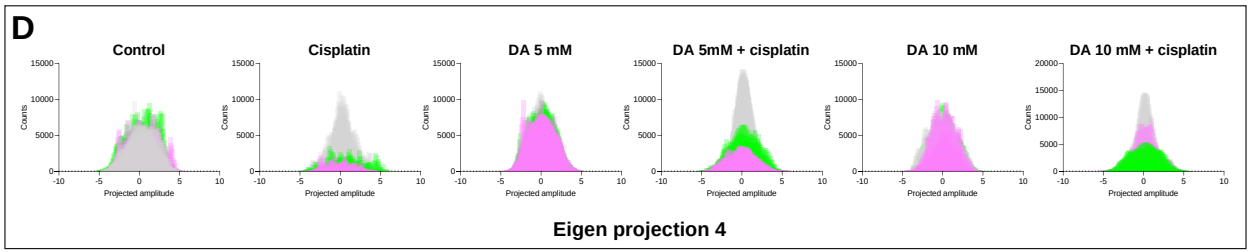
D
Control
Cisplatin
DA 5 mM
DA 5mM + cisplatin
DA 10 mM
DA 10 mM + cisplatin
Counts
Projected amplitude
Eigen projection 4

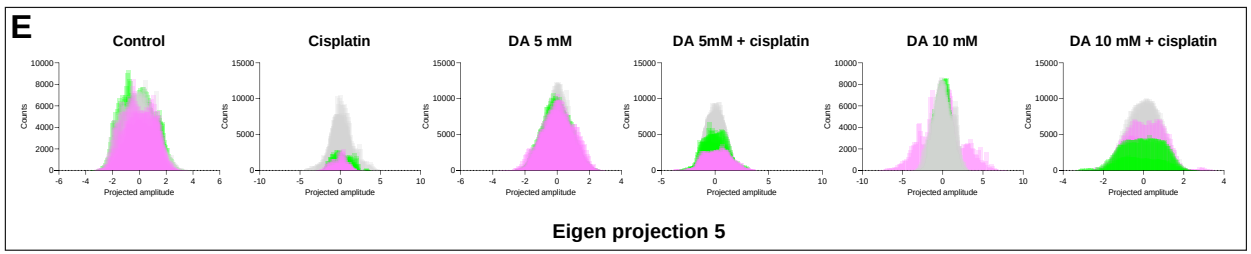
E
Control
Cisplatin
DA 5 mM
DA 5mM + cisplatin
DA 10 mM
DA 10 mM + cisplatin
Counts
Projected amplitude
Eigen projection 5

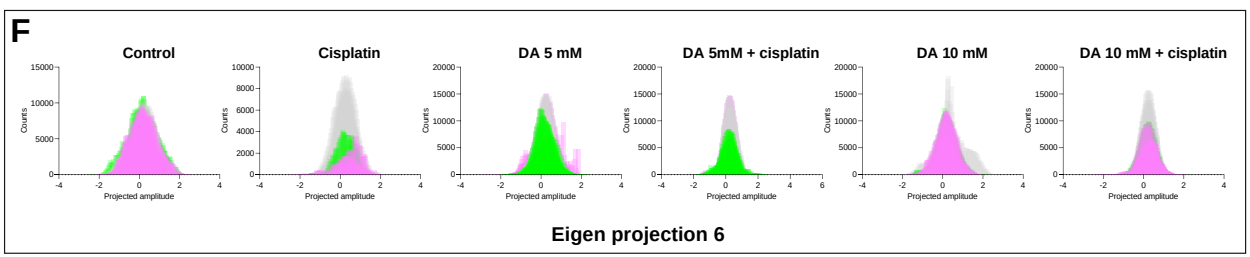
F
Control
Cisplatin
DA 5 mM
DA 5mM + cisplatin
DA 10 mM
DA 10 mM + cisplatin
Counts
Projected amplitude
Eigen projection 6

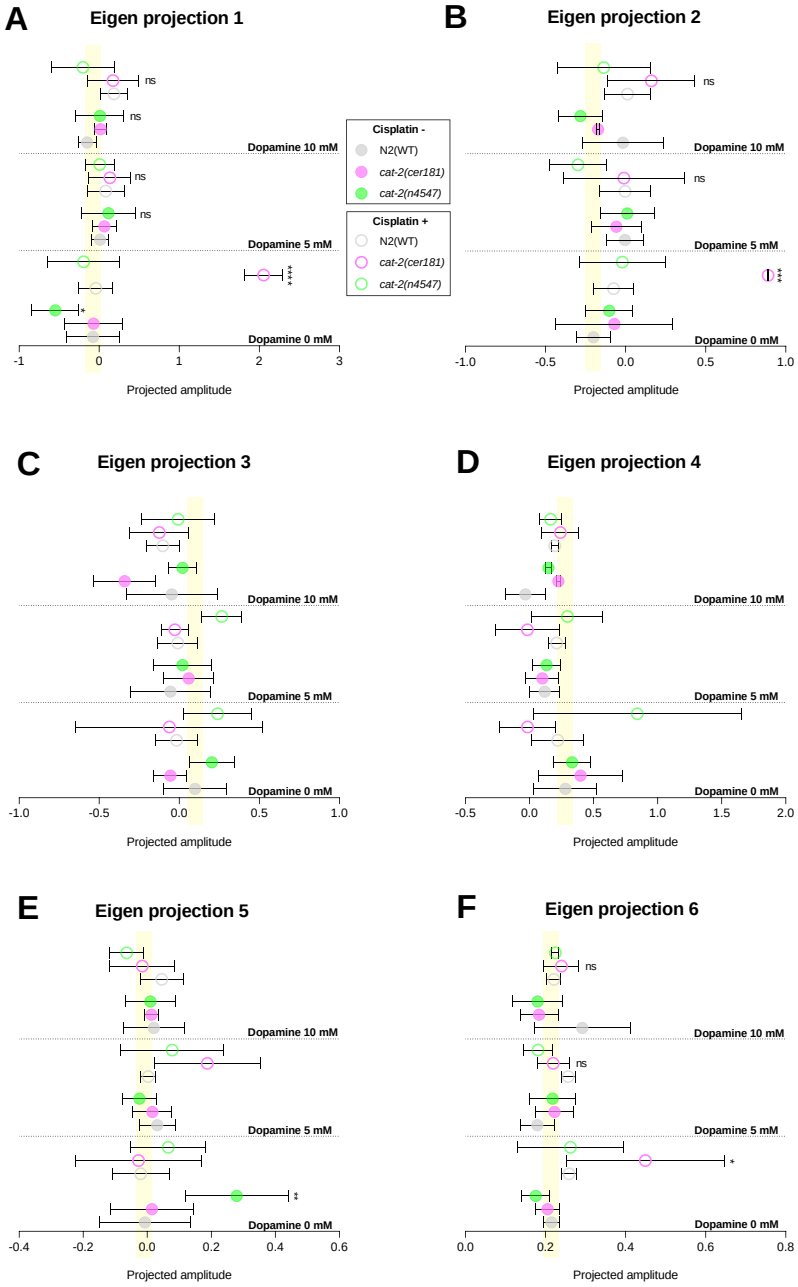
A
Eigen projection 1
B
Eigen projection 2
C
Eigen projection 3
D
Eigen projection 4
E
Eigen projection 5
F
Eigen projection 6
Cisplatin -
N2(WT)
cat-2(cer181)
cat-2(n4547)
Cisplatin +
N2(WT)
cat-2(cer181)
cat-2(n4547)
Dopamine 10 mM
Dopamine 5 mM
Dopamine 0 mM
ns
Projected amplitude

DISCUSSION

1. A model of BAP1 cancer predisposition syndrome-related mutations

Germline BAP1 mutations have been reported in families affecting a wide range of tumors. Most of these alterations are in its catalytic domain, compromising protein stability and activity. However, molecular basis has not been fully elucidated. Here, we have successfully modelled two cancer-related mutations in *C. elegans* BAP1/UBH-4: A95D/A87D and F81V/F73V, both affecting catalytic BAP1 activity in different cancer-types (Bhattacharya et al., 2015; Bott et al., 2011; Ismail et al., 2014; Ventii et al., 2008). Additionally, two different UBH-4 knockouts were generated to ensure the fully inactivation of the protein.

2. Unraveling the functional role of UBH-4 in *C.elegans*

2.1. *rpn-9* perturbations confer vulnerabilities on *ubh-4* KO and missense mutation A87D

We found *rpn-9* as a synthetic *ubh-4* interactor by RNAi and double KO mutant generation. *rpn-9* partial inactivation by RNAi caused reproductive defects on *ubh-4* deletion mutant. In double *ubh-4 rpn-9* KO, the synthetic interaction was evidenced on body length and reduced lifespan. Interestingly, A87D substitution negatively contributes to the same extent as *ubh-4* deletion suggesting an important role of this residue to

protein function or even UBH-4-RPN-9 interaction. Given that *rpn-9* is essential for proteasome assembly, without compromised cellular viability in other models (Hu et al., 2015a; Takeuchi et al., 1999; Wang et al., 2010), and that *ubh-4* contribute to ubiquitin-mediated proteostasis in *C. elegans* germline, we hypothesized that there is a cooperating role between *rpn-9* and *ubh*-4, presumably linked to the ubiquitin proteasome system.

2.2. *ubh-4* genetic alterations impact in meiotic prophase

A clear implication in the initial steps of meiotic prophase of both BAP1, in the context of BRCA1-BRAD1/BRC-1-BRD-1 complex, and the ubiquitin-mediated proteostasis has been demonstrated in different species (Ahuja et al. 2017; Kumar and Subramaniam 2018; Prasada Rao et al. 2017). Accordingly, our findings evidence the UBH-4 participation on chromosomal pairing in *C. elegans* meiosis, since UBH-4 KO negatively affects both chromosomal tethering and proteasome-mediated degradation throughout the germline. Interestingly, cancer-related inactivating mutants (*ubh-4(A87D)* and *ubh-4(F73V)*) also fails in this trait. Conversely, these missense mutations did not affect proteasome activity suggesting that some UBH-4 function remains. In addition, we suggest that UBH-4 activity is not only affecting meiotic prophase, but also oocyte maturation and embryo proliferation, since accumulation of UbG76V::GFP::H2B were observed in

maturing embryos. Nevertheless, UBH-4 is not essential in meiotic germline since no reproductive affections beyond slight reduced brood size, are observed in the KO. Thus, further efforts are needed to unravel the molecular mechanism by which UBH-4 is affecting chromosome tethering and ubiquitin-mediated proteostasis without generating major alterations on *C. elegans* reproduction. Related to this matter, we included putative BAP1 interactors (such as HCF1 or BARD1) in our RNAi screen, but not overt phenotypes were found by partially silencing those genes. Therefore, it would be interesting to perform UBH-4 protein-protein interaction assays to find out UBH-4 interactors that help us to understand new insights on its molecular function.

3. *C. elegans* as a valuable model to explore vulnerabilities of cells with BAP1 cancer-related mutations

Since UPS is involved, with increasing importance during ageing, in several key cellular pathways, is not surprising that misregulation of proteasome function leads aged-related disorders in humans (cancer and neurodegenerative diseases) (Rousseau and Bertolotti 2018) and *C. elegans* (reduced lifespan) (Liu et al. 2011). Here we discovered that combining 19S-regulatory subunit, PSMD13/RPN-9 partial or complete silencing with BAP1/UBH-4 genetic affections, additive detrimental effect is generated in our system. Hence, we

present *C. elegans* as a valuable model to explore vulnerabilities of cells with BAP1 cancer-related mutations.

Furthermore, we propose to pharmacologically target PSMD13/RPN-9 or even 19S regulatory complex to impede proteasomal assembly in presence of UBH-4/BAP1 mutations compromising the proteasome catalytic activity. This combined strategy could impede the adaptation of the tumoral cell to the reduction of proteasome-mediated activity (Huang et al. 2017; Manasanch and Orlowski 2017; Rousseau and Bertolotti 2018) given by UBH-4/BAP1 alterations.

4. Investigating cisplatin toxicity in *C. elegans* metabolism and mitochondrial respiration

In the part II of this study, we have taken the advantage of *C. elegans* as valuable model to explore the toxicity of cisplatin at both systemic and cellular levels. First, we found cisplatin-induced toxic effects through fat and sugar metabolism at systemic level. Additionally, we showed that mitochondrial damage is conferred upon cisplatin exposure.

4.1. Modulating animal response to cisplatin through fat and sugar metabolism

Our previously published transcriptomes (García-Rodríguez, et al. 2018) and the recent discoveries linking hyperglycemics to cisplatin adverse effects on cancer patients (Bergamino et

al., 2019), suggest a functional connection between carboxylic acid metabolism and cisplatin toxicity.

4.1.1. Hyperglycemics modulates systemic cisplatin response in *C. elegans*

To go deeply into this assumption, we started developing a high-glucose model for cisplatin therapy evaluation based on Schlotterer et al. 2009. A observed in clinical studies (Bergamino et al., 2019), we found in our model a relevant detrimental association between intracellular glucose levels and cisplatin-based through alterations in worms' body length.

On the one hand, reduced body length when cisplatin was added in both moderate and high-sugar supplementation environments were found. Interestingly, lower-glucose supplements showed a kind of protective effect on cisplatin therapy, emulating a hormetic stress response[4] in combination with the drug. In several animal models, adaptative responses have been previously shown to be produced by other oxidative agents or even by reducing the activity of core biological processes (Shore et al., 2012; Ventura et al., 2009), finding application in studies of aging (Gems and Partridge, 2008; Jovaisaite et al., 2014; Yee et al., 2014).

[4] Refers to the beneficial effects of a treatment that at a higher intensity is harmful. In one form of hormesis, sublethal exposure to stressors induces a response that results in stress resistance.

On the other hand, neither low nor moderate glucose supplements *per se* instigated any effect on the nematode body length. However, the highest concentration significantly affects the worm's length, which is not surprising because glucose-enriched diets cause a broadly set of phenotypes (such as reproductive alterations and aging) and metabolic changes (such as glucose content and lipid composition) (Alcántar-Fernández et al., 2019).

4.1.2. A model to predict cisplatin-based chemotherapy efficacy

Accordingly, based on the observation that cisplatin raised fat content in *C. elegans*, we found that genetically targeting *sbp-1*/SREBP-1c transcription factor, animals get sensitive to the drug. This finding is interesting since, in similar high glucose conditions, increased *sbp-1* transcripts (up to 176%), signs of oxidative stress (such as increased expression of mtSOD and CAT), and accelerated aging were observed (Alcántar-Fernández et al., 2018). Thus, we could hypothesize a synergistic role between cisplatin and hyperglycemia through promoting oxidative stress. Further study is necessary to unravel additional factors involved in fat metabolic changes induced by cisplatin in *C. elegans*. As an example, *lilp-3* (implicated in lipid catabolic process) was pointed out in our RNA-seq analyses, suggesting a relevant role in cisplatin response.

It would be of great interest to examine fat composition (by inhibiting key players in its regulation under toxic conditions since hypersensitivity inferred from fatty acid downregulation could reflect changes on cuticle composition (Liang et al. 2010) which in turn, may affect cisplatin absorption. All together evidence a cisplatin involvement on lipid accumulation, metabolism and content which is additively incremented in a high-glucose cellular context.

Our contribution may help explore how to predict cisplatin-based chemotherapy's adverse effects on cancer patients presenting metabolic disorders. In this sense, screening antidiabetic drugs (such as metformin) on our model should help find therapies to alleviate cisplatin adverse effects. Conversely, affecting lipid metabolism through SREBP-1c may function as a strategy to resensitize tumour refractory to cisplatin, which is one of the major clinical limitations of cisplatin-based chemotherapies.

4.2. Cisplatin triggers mitochondrial damaging responses

4.2.1. Cisplatin elicits mitochondrial damage

A protective response to mitochondrial ROS through BH3-only CED-13 protein, instead of promoting apoptosis, has been previously described in *C. elegans* by Yee and colleges in 2014. Similarly, we demonstrated a protective role of CED-13 in cisplatin-induced cellular oxidation (García-Rodríguez et al.

2018). Based on these results and taking in account that CED-13 expression is relevant in mtROS-induced mechanism of response (Yee et al., 2014), we suggest a protective role of CED-13 in cisplatin-induced mtROS. However, since paraquat additively sensitizes *ced-13* mutants to cisplatin, distinct mechanisms could be involved in worm's cisplatin and paraquat responses. Moreover, stimulation of mtUPR is also observed under cisplatin exposure, further supporting that cisplatin produces mitochondrial damage.

4.2.2. Cisplatin negatively affects mitochondrial respiration

Mitochondrial respiration is impaired after both glucose and cisplatin pre-treatments. Regarding *C. elegans* respirometry profile, cisplatin simulates the effect of sodium azide, which suggests that it could be explicitly targeting cytochrome c oxidase (complex IV) or the ATP synthase (complex V) (Koopman et al., 2016). OXPHOS complexes damage could also explain the cisplatin-induced mtUPR (Choi et al., 2015). Interestingly, glucose or paraquat conditions provoke similar but milder effects. Basal respiration OCR values provide additional proof of mitochondrial respiration deficiency. Accordingly, it is known that increasing the glucose content causes a shift from oxidative phosphorylation towards glycolysis, which, in turn, causes a reduction in oxygen consumption (Koopman et al., 2001). In other models, cisplatin-induced mitochondrial respiration affection has also

been described (Inapurapu et al., 2017). We possess preliminary data showing that *ced-13* are sensitive to cisplatin in mitochondrial respiration, thus further evidencing cisplatin-induced mitochondrial dysfunction.

Consistently, our previous findings, together with those generated in this work, suggest that a high glucose diet and cisplatin exposure cause signs of oxidative damage in *C. elegans*. Moreover, involving common metabolic pathways, such as insulin signaling, lipid content, and metabolism result affected in these conditions (Alcántar-Fernández et al. 2019; García-Rodríguez, et al. 2018). Moreover, recent observations support that mitochondrial accumulation of cisplatin triggers mtROS and alters glycolysis-, TCA cycle- and mitochondrial stability-related genes and in addition, affects mtDNA encodes for OXPHOS complexes I, III, IV and V (Choi et al., 2015). In clinics, mitochondrial content has been proposed as a biomarker for platinum-based therapies response and, in counterpart, as a cisplatin resensitizing anticancer strategy (Cocetta et al., 2019). All the above supports our findings regarding cisplatin-induced abnormal lipid metabolism and mitochondrial respiration.

5. Automated method to evaluate cisplatin neurotoxicity in *C. elegans*

Here, we reinforce the use of this nematode to particularly investigate cisplatin induced neurotoxicity by analysing different behavioral features: path range and worm posture.

5.1. Generation of dopamine signaling-related strains by CRISPR/Cas technology

First at all, we generated a set of mutants related to dopamine metabolism, based on our previous hypothesis that catechol-*O*-metyltransferase could be involved in cisplatin-induced toxicity in *C. elegans* (García-Rodríguez et al. 2018). Exploiting the power of CRISPR/Cas9 technology I have generated deletion alleles for those COMT family members. These genes present higher transcriptional activity at post-embryonic stages, which make them suitable for functional studies of worm behavior and locomotion. Additionally, we generated a new allele for the tyrosine hydrolase *cat-2* because the existing alleles may affect other neighbor genes. To unravel the cellular localization and variation in expression levels of these dopamine-related proteins (COMT family), we employed Nested CRISPR, a methodology developed in our lab (Vicencio et al., 2019). So, simultaneously depletion of the desired locus and insertion of the landing pad for a completely fluorescent can be produced. In that way, the nuclear endogenous reporter for *comt-4* was generated. Here we

emphasized the advantage of nuclear reporters to study low-expressed genes. However, further efforts are needed to describe COMT members *cat-2* through development:

- Nuclear endogenous reporter generation.
- Cellular location characterization.
- Reveal the fluorescence dynamics under toxic cisplatin scenario or even when dopamine signaling is disturbed.

5.2. Establishing the method for cisplatin neurotoxicity evaluation

Conveniently, using an automated tracking system (Javer et al., 2018a; Yemini et al., 2013), we investigated the neuronal impairment caused by cisplatin in adult *C. elegans.* Thus, we stablished a method to evaluate cisplatin neurotoxicity in the nematode. One of our findings was that wild-type animals covered reduced distances when they were subjected to toxic dose of the drug. This alteration is probably due to locomotion abnormalities since other related features such as number of body bends were also affected under this condition. The high spatial and temporal resolution of Worm Tracker allow us to discern subtle changes in the worm body shape, by the reconstruction of the six eigenworms. Thus, we found that under toxic conditions (250 µg/mL) dopamine-defective mutants present postural alterations compared to wild-types. In our attempt to alleviate that injury, low-dose dopamine was sufficient to restore normal path range values.

5.3. The role of dopamine signaling on animal behavior

In clinics, cisplatin-induced toxic effects (nephrotoxicity) have been shown to be alleviated by dopamine administration (Somlo et al., 1995). In addition, both in humans and *C. elegans*, certain drugs and toxins have been shown to interfere with, or block, the action of neurotransmitters causing motor abnormalities, parkinsonism[5] in humans and behavioral phenotypes in the nematode (Osuna-Luque et al., 2018; Tolosa et al., 2006). Since cisplatin cause a locomotor phenotype similar to mutations in *cat-2*, and the dopamine supplementation rescue such cisplatin-induced locomotor defects, our data suggest that cisplatin affects the activity of dopaminergic neurons. Nevertheless, it must be needed to further investigate specific cisplatin targets on DA signaling, such as *dat-1*, *dop-1* DA transporter and receptor, respectively.

Regarding our COMT family mutants, in the absence of cisplatin, *comt-4* and *comt-5* mutants present low path range, resembling excess of dopamine when 10 mM DA was supplemented. This result suggests that the excess of dopamine in both scenarios causes an abnormal dopamine neuromodulation of the locomotor circuit. Curiously, dopamine deficient mutants resembled similar path range affection, indicating that not only excess but also reduced levels of

[5] Cluster of motor symptoms (bradykinesia, resting tremor, rigidity, and postural instability) by brain disorders, brain injuries, or certain drugs and toxin.

neurotransmitter could affect neuromodulation in this sense. Similar findings, evidencing the importance of dopamine signaling on *C. elegans* locomotor behavior, have been reported (Omura et al., 2012; Rodríguez-Ramos et al., 2017b; Tolosa et al., 2006; Vidal-Gade et al., 2011).

All together highlight the importance of DA metabolism on neuronal redox-homeostasis and viability. Whereas some DA derivates show antioxidative effects DA oxidation itself can lead to exogenous neurotoxins (Meiser et al., 2013), which can explain similar behavior alteration in two different dopamine signaling backgrounds: high- (DA 10 mM, *comt-4* and *comt-5* mutants) and low-DA signaling (*cat-2* mutants).

Regarding conventional DA-dependent phenotypes studied in this work (**Table 5**), only body length and brood size were found to be significantly affected when *comt-4* and *comt-5* were depleted. Consistently, the contrary phenotype was observed in dopamine-defective mutant (*cat-2(n4547)*), indicating opposite roles on dopamine metabolism. Curiously, we did not find any behavior alteration in *comt-3* mutant background, evidencing none or low DA-linked activity on *C. elegans*. Nevertheless, additional studies are needed to find out sensitivity or resistance regarding cisplatin toxicity in presence or absence of dopamine.

CONCLUSIONS

1. Homozygous *ubh-4* deletion alleles as well as BAP1 cancer-related mutations, A87D and F73V, are tolerated in *C. elegans* thus allows to investigate its functional role on this system.

2. The 19S proteasome non-ATPase subunit RPN-9 is a synthetic interactor of UBH-4 affecting germline development and animal' body length and survival.

3. Cancer-related mutation A87D has a relevant role on UBH-4 function since it mimics the detrimental effects of protein knockout in *rpn-9* mutant background. Thus, we propose to target PSMD13/RPN-9 as anticancer therapy in BAP1 cancer predisposition syndrome when BAP1 activity is compromised.

4. UBH-4 positively modulates ubiquitin-mediated protein degradation in *C. elegans* germline.

5. *C. elegans* chromosomal tethering fails in the presence of *ubh-4* genetic alterations, suggesting that proteasome is required for the pairing process initiation.

6. *C. elegans* cisplatin toxicity can be negatively modulated by rising glucose levels up to diabetic concentration.

7. Affecting lipid metabolism through SBP-1/SREBP-1c wild-type animals turn hypersensitive to cisplatin. Thus, we propose SREBP-1c as a novel target to sensitize cisplatin-resistant tumors.

8. Superoxide generator paraquat additively impacts *C. elegans* systemic response to cisplatin, being more affected in a *ced-13*-defective background. This suggests a protective role of *ced-13* in cisplatin-induced redox imbalance.

9. Cisplatin provokes mitochondrial respiration dysfunction and UPRmt activation similarly but, to a greater extent, than high-glucose and paraquat treatment.

10. Since CRISPR/Cas generated dopamine signaling-related null mutants do not display overt phenotypes, they can be used to study cisplatin neurotoxicity in *C. elegans*.

11. We established a semi-automated method to evaluate cisplatin neurotoxicity in *C. elegans* by analysing different behavioral features: path range and posture.

12. Cisplatin causes abnormal dopamine neuromodulation of the locomotory circuit since drug-exposed wild-type animals mimics dopamine defective mutants' behavioral alterations.

13. Proper levels of dopamine are essential to maintain normal displacements since mutants with altered dopamine levels and exogenous dopamine administration in wild-type animals produce alterations in this behavioral trait.

14. Dopamine is required, not only to maintain normal worm posture but also to rescue altered body curvature induced by cisplatin treatment.

MATERIALS AND METHODS

1. *Caenorhabditis elegans* strains

C. elegans strains were maintained using standard procedures (Stiernagle, 2006). Before conducting the experiments, strains were grown for at least two generations at the experimental temperature. Worms were synchronized using sodium hypochlorite (Porta-de-la-Riva et al., 2012). N2 was used as WT strain. Used strains for this study were generated by CRISPR/Cas (pointed out by grey shadow) or provided by the Caenorhabditis Genetics Center (CGC) (**Table 6**). Mutants generated by CRISPR were outcrossed x2, and all the used strains were genotyped before its use. Pimers used for genotyping are listed in **Table 7**.

2. PCR genotyping

Single or pooled worms were picked into 0.2 ml tubes containing 10 µl 1x MyTaq Reaction Buffer and 66.67 µg/ml proteinase K. In order to lyse the animals, the tubes were incubated at 60^{o}C for 1 hour followed by an incubation at 95^{o}C for 15 minutes to inactivate the proteinase K. 20 µl of water were added to dilute worm lysates and 2 µl were subsequently used as templates for polymerase chain reaction (PCR) amplification using MyTaq^{TM} DNA polymerase (Bioline) according to the manufacturer's instructions. The primers used for genotyping are listed in **Table 7**.

Table 6: Strains used in this study.

Strain	Genotype	Reference
CER323	*ubh-4(cer27) II*	This study
CER250	*ubh-4(cer25 [F73V]) II*	This study
CER344	*ubh-4(cer32)[A87D] II*	This study
CER378	*ubh-4(cer67[UBH-4::EGFP 1-3])II*	This study
CER395	*ubh-4(cer68[UBH-4::EGFP])II*	This study
CER522	*ubh-4 (cer140); rpn-9(gk401)/mIn1 [mIs14 dpy-10(e128)] II*	This study
CER535	*ubh-4(cer150) II*	This study
VC984	*rpn-9(gk401)/mIn1 [mIs14 dpy-10(e128)] II*	CGC
CER616	*ubh-4(cer150)II; dhc-1(ie28[dhc-1::degron::GFP]) I*	This study
CER617	*ubh-4(cer25 [F73V]) II; dhc-1(ie28[dhc-1::degron::GFP]) I*	This study
CER618	*ubh-4(cer32)[A87D] II; dhc-1(ie28[dhc-1::degron::GFP]) I*	This study
IT1187*	*unc-119(ed3) III; kpIs100 [pie1p::Ub(G76V)::GFP::H2B::drp-1 3' UTR; unc-119(+)]*	A gift from Subramaniam lab
CA1215	*dhc-1(ie28 [dhc-1::degron::GFP]) I; ieSi38 [sun1p::TIR1::mRuby::sun-1 3'UTR + Cbr-unc-119(+)] IV*	This study
CER625	*ubh-4(cer150) II; Ub(G76V)::GFP::H2B*	This study
CER626	*ubh-4(cer32)[A87D] II; Ub(G76V)::GFP::H2B*	This study
CER627	*ubh-4(cer25 [F73V]) II; Ub(G76V)::GFP::H2B*	This study
CER620	*ubh-4(cer68[ubh-4::EGFP]); rpn-9(cer203[rpn-9::wrmScarlet]) II*	This study
CER494	*comt-5(cer126 [comt-5p::gfp::h2b 1-3]) V*	This study
CER496	*comt-4(cer128[comt-4p::gfp::h2b 1-3]) V*	This study
CER498	*comt-3 (cer130[comt-3p::gfp::h2b 1-3) V*	This study
CER587	*comt-3 (cer166[comt-3p::gfp::h2b 1-3); comt-4(cer128 [comt-4p::gfp::h2b 1-3]; comt-5(cer167 [comt-5p::gfp::h2b 1-3]) V*	This study
CER497	*comt-4(cer128 [comt-4p::gfp::h2b 1-3] comt-3 (cer166[comt-3p::gfp::h2b 1-3) V*	This study
CER554	*comt-4(cer157[comt-4p::GFP::H2B]) V*	This study
CER430	*comt-4(cer98[comt-4p::mCherry 1-3]) V*	This study
CER423	*comt-4(cer101[comt-4p::mCherry]) V*	This study
CER588	*cat-2 (cer181 [cat-2p::gfp::h2b 1-3]) II*	This study
MT15620	*cat-2 (n4547) II*	CGC
CE833	*sbp-1(ep176) III*	CGC
CE541	*sbp-1(ep79) III*	CGC
FX536	*ced-13(tm536) X*	CGC

3. CRISPR generation of strains

Guide RNAs were designed using both Benchling (www.benchling.com) and CCTop (Stemmer et al., 2015) online tools. All CRISPR/Cas9 mutant and reporter strains were obtained following a co-CRISPR strategy (Kim et al., 2014) using *dpy-10* as a marker to enrich for genome-editing events (Arribere et al., 2014). In the case of CER588 *cat-2(cer181[cat-2p::gfp::h2b 1-3])II,* Cas12a (Cpf1) were used instead Cas9. In this case, co-CRISPR was not viable beacause of the inneficient crRNA for *dpy-10*. In all cases, mixes were injected into gonads of young adult P_0 hermaphrodites using the XenoWorks Microinjection System and following standard *C. elegans* microinjection techniques. F_1 progeny was screened by PCR using specific primers and F_2 homozygotes were confirmed by Sanger sequencing.

As we optimized the protocol for CRISPR/Cas9 genome editing in our laboratory in the course of this project, different reagents and conditions were used to produce the distinct mutants, except for strains generated by Nested CRISPR step 1, step 2 and one-shot. For these strains protocols are described and universal sequences for step II are detailed in Vicencio et al. 2019. Only the *ubh-4(cer27)* deletion mutant allele was obtained by nonspecific DSB repair. For all mixes preparation, RNP complexes containing crRNA, tracrRNA and Cas9/Cas12a were annealed at 37°C for 10 minutes and later, the remaining reagents were added. Prior to injection, mixes

were centrifuged 5 minutes at 13000 RCF. All the reagents used in this study are listed in **Table 8** and **9**, and the composition of the injection mixes is specified in **Table 10 a-e.**

Table 7: List of primers used for genotyping.

Gene	Allele		Primer Fwd	Primer Rev
ubh-4	*cer27* *cer140* *cer150*		gCACAATAAATCTCTTTTCGG	caaaaacaatcaagaaccc
	cer25	WT	CCTAGTGACAAGCAAAACATCTT	GCAGTTTCTGTTTGCGGTTTGG
		Mut	CCGTCGGATAAGCAGAATATCGTC	
	cer32	WT	CGTCACAATTATACTCCG	GTTCTCCATCATCTCCTGC
		Mut		CATCAGCAGGTTGATAAGAT
	cer67, *cer68*		CGTCACAATTATACTCCG	caaaaacaatcaagaaccc
rpn-9	*gk401*		gctgtgttgccagctggcgg	cCAATTCTCCGAAGTTGTGCACG
comt-4	*cer58* *cer128* *cer98* *cer101*		TCCAAAGTTCAGTTCGGAAG	CCAGAAATCGGACTTGATTGA
comt-3	*cer130* *cer166*		cttgttctctcggactatctgatag	TGTCTACTTTGCCCCCAATG
comt-5	*cer126* *cer167*		ccctccaaacagctattgaaacg	ACATGAGTTCCATCGCCAAGA
cat-2	*n4547* *cer181*	WT	ctatgtgaagtcacacctgtc	gagatcacggatcacaagag
	cer181	Mut		cttgctggaagtgtacttggtg
ced-13	*tm536*		GTCAGGTGGCCCACGAAAC	CAGTACGTGCTTGATGCAC
sbp-1	*ep176*	WT	GCAGAATAATCGATTACCG	GGAGAAGGAGATGATTCG
		Mut		CGACAAGTTCCTGTAC
L4440*			GTTTTCCCAGTCACGACGTT*	TGGATAACCGTATTACCGCC*

* Primers used to verify RNAi clone insert size in the L4440 plasmid. Lowercase letters indicatenucleotides from UTRs or introns and uppercase letters nucleotides from exons.

Table 8: list of crRNAs used for mutants and endogenous reporters generation.

Name	Generated allele	Sequence
ubh-4 5'	*cer27, cer140, cer150*	TGTTTTCAGATGACTGATGC
ubh-4 3'		TTTTCTCTTCAATTCAAGCT
ubh-4 F73V	*cer25*	AAGATGTTTTGCTTGTCACT
ubh-4 A87D	*cer32*	CATCAACTTGCTTATGAACG
comt-4 5'	*cer58, cer98, cer128*	TATTGTTGCCAAGAGTTACG
comt-4 3'		TTCACTTCTTAAAAGCCATG
comt-3 5'	*cer130, cer160*	CGCAAAAAGCTACAAGAGCT
comt-3 3'		TCGCTTTTAAGAAGTGAATT
comt-5 5'	*cer126, cer167*	TAAGGATGCCGATCCAGTGG
comt-5 3'		AATTTCCAGAGCCTTCGCGG
cat-2 5'	*cer181*	CGTGATCCTCTCCAGAGCCC
cat-2 3'		ACATTGTAATCGATATTTTC
rpn-9 5'	*cer203*	GGAAGGAATCGTCAGCAAAG

Table 9: List of ssODN used for mutants and Nested CRSPR step 1 generation.

Locus	Generated allele	Sequence
ubh-4	*cer25*	GTTCAAGTGGCGCCAGGGAGATGAAACAACTGGGATTCCGTCGGATAAGCAGAATATCGTCTTTGCTCATCAAACAATTCAAAACGCTTGTGCTACTC
	cer32	TCATCAAACAATTCAAAACGCTTGTGCTACTCAAGATCTtATCAACcTGCTgATGAAtGTaGAAGATACCGATGTGAAGCTTGGAAATATCCTGAA
	cer67 (Step I)	AAGAAAAATCCAAGCTGAATACAGACATAACCAAG**TCCAAGCTGAATACAGACATAACCAAGTCCAAGGGAGAGGAGCTCTTCACCGGAGTCGTCCCAATCCTCGTCGAGCTCGACGGAGTCAAGGAGTTCGTCACCGCTGCCGGAATCACCCACGGAATGGACGAGCTCTACAAG**CTTGAATTGAAGAGAAAACAATAGatattgcattct
	cer140, cer150	caaataaataattcaagtacgtttagaatgcaatatgaaaacaaAAATAAACTTAGTTTTTTCAAAATTT
comt-4	*cer98 (Step I)*	caaaactccaaaaATGTCTATTGTTGCCAAGAGTTAC**TCCAAGGGAGAGGAGGACAACATGGCCATCATCAAGGAGTTCATGCGTTTCAAGGCCGAGGGA CGTCACTCCACCGGAGGAATGGACGAGCTC**TGAatggatatttaaatgagaattttattttattgt
	cer128 (Step I)	TTTCAGTTTTTTTTTCCGAAAAAAAAAATGTCCAAC**ccaagtttgtacaaaaaagcaggctccatgagtaaaggagaagaacttttcactggagagggaaccaaggccgtcaccaagtacacttccagcaagtaa**ATTAGGGGCTTTTTTTTTAATTTTGAATTATATTTA
comt-3	*cer130, cer166*	tttcagttttttttccgaaaaaaaaaATGTCCAACccaagtttgtacaaaaaagcaggctccatgagtaaaggagaagaacttttcactggagagggaaccaaggccgtcaccaagtacacttccagcaagtaaattaggggctttttttttaattttgaattatattta
comt-5	*cer126, cer167*	GTTGTCGCTAAGAGTTATCATAAGGATGCCGATCCAccaagtttgtacaaaaaagcaggctccatgagtaaaggagaagaacttttcactggagagggaaccaaggccgtcaccaagtacacttccagcaagtaaCGGTGGCTCCGTAGCTGACGAGAAAAGACGAGAAGA
cat-2	*cer181*	TCGTTGTTGGCGTGGGGACCCCTTGAAAAATTGGAAGAGGAAATGTTTTTGCGGTATATGCGGAGGCGGGGCagtaaaggagaagaacttttcactggagttgtcccaattgccgtgtctgagggaaccaaggccgtcaccaagtacacttccagcaagTGAAACCTAATTTACCTAATACTTTGCTAAACTAT
rpn-9	*cer203*	GAACGATGTCAACTCCATGGAAGGAATCGTCAGCAAA**gtcagcaagggagaggcagttatcaaggagttcatgcgtttcaaggtccacatggaggGatccatgaccgagggacgtcactccaccggaggaatggacgagctctacaag**GAGGCACGCGAGATTCTCACTCAAAATTAAatcat

EGFP fragment 1-3; EGFP::H2B fragment 1-3; **wrmScarlet fragment 1-3**

Table 10: Injection mixes used for transgenic lines generation.

a. Deletion allele	
Reagent	**cf µM**
Cas9	6.57
tracrRNA	48.26
dpy-10 crRNA	5.26
target gene crRNA 1	20.77
target gene crRNA 2	20.77
target gene ssODN	15.51
dpy-10 ssODN	3.87

b. Missense mutation	
Reagent	**cf µM**
Cas9	6,57
tracrRNA	48,26
dpy-10 crRNA	5,26
target gene crRNA	20,77
target gene ssODN	15.51
dpy-10 ssODN	3.87

c. Transcriptional reporter SI	
Reagent	**cf µM**
Cas9	61
tracrRNA	320
dpy-10 crRNA	50
target gene crRNA 1	100
target gene crRNA 2	100
Step 1 ssODN	100
dpy-10 ssODN	32.7

d. Transcriptional reporter SII	
Reagent	**cf µM**
Cas9	61
tracrRNA	320
dpy-10 crRNA	100
Step 2 crRNA	100
Step 1 ssODN	100
dpy-10 ssODN	32.7
PCR product	~ 1

e. Traslational reporter one-shot	
Reagent	**cf µM**
Cas9	61
tracrRNA	320
dpy-10 crRNA	100
target gene crRNA	100
Step 2 crRNA	100
Step 1 ssODN	100
dpy-10 ssODN	32.7
PCR product	~ 1

4. Plates with special requirements

Cisplatin plates: Cisplatin (Accord) 1 mg/mL was used as a stock solution. For solid cisplatin plates preparation, 55 mm NGM plates, with 10 mL agar, were prepared. The next day, 600 µL cisplatin solution stock was added on the surface to reach the desire concentration. When dried, 300 µL overnight OP50 culture were seeded.

High-glucose plates: D-(+)-Glucose powder (Sigma-Aldrich) was diluted in deionized water for stock solutions preparation at the desired concentration. 300 µL from the respective stock solution was added into the plates before been seeded and incubated overnight at room temperature. After incubation, plates were seeded with 300 µL overnight OP50 culture.

Paraquat plates: Paraquat (Sigma-Aldrich) powder was resuspended in DMSO (Dimethyl sulfoxide) to reach 1M as a stock solution. Paraquat solution was added to NGM medium (still melted), mixed, and poured into 55 mm plates. 0.1 mM was used as final paraquat concentration. 300 µL overnight OP50 culture were seeded.

Low peptone plates (tracking plates): Low peptone plates were prepared as follows (for 1 L plates): 3 g sodium chloride, 20 g agar, 0.13 bactopeptone and 1L desionized water were mixed and autoclaved. Then, 3.5 cm plates where prepared with this solution plus standard concentration buffers (Stiernagle, 2006). Plates were seeded with a single droop in the middle of

the surface from an overnight OP50 culture the day before the experiment.

Plates for RNA interference (RNAi):NGM plates supplemented with 3 mM IPTG (AppliChem), 50 µg/ml ampicillin (AppliChem), and 12.5 µg/ml tetracycline (Sigma-Aldrich) were used to conduct RNAi screen and subsequent validation experiments. Bacterial cultures of different RNAi clones were grown overnight at 37ºC in LB with 50 µg/ml ampicillin and 12.5 µg/ml tetracycline. dsRNA synthesis was induced overnight at room temperature.

5. Body length assay

A synchronized population of L1-arrested larvae was cultured on NGM plates containing fresh OP50 and 60 µg/ml of cisplatin. The body length of ≥50 worms for each condition was measured at 72 h or 96 h at 20°C on the stereomicroscope using NIS-Elements 3.2 imaging system. Experiments conducted at 15°C, the body length was measured after 5 days of incubation. Each assay was done in duplicate, and at least two biological replicates were performed.

6. Brood size

A synchronized population of L1-stage worms was grown into NGM plates, with fresh OP50 until L4 stage at 20ºC. An average of 12 animals from each genotype were seeded individually into separated plates. Animals were passed to a

new plate after few days until total progeny were laid. Progeny were counted after each pass.

7. RNA interference

7.1. Gene sublibrary generation

For RNAi screen *ubh-4* knockout (*cer27*) was used and N2 as WT strain. 150-genes sublibrary was generated in order to perform the screen. RNAi clones were obtained from the ORFeome library (Rual et al., 2004) or the Ahringer library (Kamath et al., 2003) and insert size was validated by PCR in all the clones used. Primers for genotyping are listed in **Table 6**. The 150-genes sublibrary includes: proteasome-related enzymes, 20S and 19S proteasome particle subunits, putative and confirmed BAP1 interactors, cancer-related genes and a set of genes related with Malignant Mesothelioma and Melanoma were chosen for the screen (Poulin, Nandakumar, and Ahringer 2004; Kato et al. 2016; De Rienzo et al. 2016; Soura et al. 2016). Genes included in the study were analyzed for *C. elegans* conservation by using Wormbase (https://wormbase.org/) and BLASTP (Camacho et al., 2009). In addition, putative UBH-4-protein interactors included were selected based on STRING 11.0 database (Szklarczyk et al., 2019). The classification and description of these genes are collected in **Table**.

7.2. RNAi screen of 150 genes

For the RNAi screen 24 well plates were prepared as described in **Materials and Methods 4**, **Plates for RNAi**. These plates were seeded with 30 µl of bacterial cultures of different RNAi clones grown overnight at 37ºC in LB with 50 µg/ml ampicillin and 12.5 µg/ml tetracycline. dsRNA synthesis was induced overnight at room temperature. Synchronized L1-arrested worms were placed onto RNAi plates and different phenotypes were scored at every day at 20ºC for 168h. The screen was conducted in triplicate for each condition and was performed two different times, with different batches of RNAi plates and cultures. In all the cases, *gfp* was used as a negative control.

7.3. Validation of candidates

Candidate clones were further validated in 55 mm RNAi plates seeded with 300 µL RNAi clone culture grown overnight at 37ºC in LB with 50 µg/ml ampicillin and 12.5 µg/ml tetracycline. RNAi plates preparation and dsRNA induction were performed as previously described. *gfp* was used as a negative control. Gene validation was conducted at 20ºC, in duplicates at two different experiments with different batches of RNAi plates and cultures. For *rpn-9,* individual animals were plated separately when reached L4 stage and were passed into a new RNAi plate each two days until they stopped lay eggs. Hatched larvae, dead embryos and animals presenting cuticle abnormalities were scored.

8. Cisplatin and dopamine pre-treatment for automated tracking videos

Animals were synchronized and grown at 20ºC in NGM plates from L1 for 34 hours. Then, they 30 animals per well were manually transferred to liquid culture for control, cisplatin (Accord,1 mg/mL), or dopamine (Sigma-Aldrich) treatments for 24 hours (**Table 11**). as source of food, 25 mL overnight culture were centrifuged and diluted in 5 mL M9. 12-well plate were used to plate the animals. Three different biological replicates were prepared per each condition. The day of the experiment, animals were recovered and washed in M9 and finally seeded on tracking plates. Nematodes were let for habituation for 10 min before to be recorded.

Table 11: Liquid medium recipe for tracking videos pre-treatment.

	Condition					
	Control	**Cisplatin**	**5 mM DA**	**10 mM DA**	**Cisplatin + 5 mM Da**	**Cisplatin + 10 mM Da**
OP50 solution	250 µl	250 µl	250 µl	250 µl	250 µl	250 µl
S-medium complete*	250 µl	250 µl	237.5 µl	225 µl	237.5 µl	225 µl
Dopamine	-	-	12.5 µl	25 µl	12.5 µl	25 µl
Cisplatin	-	250 µl	-	-	250 µl	250 µl
H_2O	250 µl	-	250 µl	250 µl	-	-

*As described in (Stiernagle, 2006)

9. Lipid staining

9.1. Worm fixation

Worms were synchronized and grown at 20ºC in NGM plates with the corresponding treatment for 72h. Prior fixation, animals were washed three times in a 15 mL conical tube with M9 to get rid of bacteria. Incubate in 5-6 mL of the same buffer for another 30 min to excrete the bacteria in the gut. Then, worms were transferred to a microfuge tube, leaving them on ice. For fixation, 10% paraformaldehyde stock was added to final concentration of 1%, mixed and frozen in dry ice/ethanol. Samples were melted under stream of 37ºC bath. Consecutive freeze-thaw cycle was repeated 2-3 times. After the final thaw, samples were incubated on ice with occasional agitation for 10 minutes.

9.2. Sudan black staining

Fixed worms were washed in cold M9 at least three times. Then, animals were dehydrated through ethanol series: 25%, 50% and 70%. Worms were kept on each gradient for two minutes. Finally, 2-5 volumes of Sudan Black B saturated solution were added to the worms. Incubation in Sudan Black B solution was made during 30 minutes in agitation. A saturated solution of Sudan Black B (Sigma #S2380) was prepared by diluting 1g in 100 mL 70% ethanol. Stock solution can be kept for prolonged periods. Solution must be filtered with a syringe and a 0.45-micron filter before using.

10. Mitochondrial respiration in *C. elegans*

Mitochondrial respiration was determined by measuring oxygen consumption rate (OCR) by Seahorse XFe96 Analyzer (Agilent). Optimized procedure proposed in Koopman et al. 2016 was followed with minor modifications. Oxygen consumption rate was calculated in N2 and *cer13(tm536)* treated with 5 different conditions: 60 µg/mL cisplatin, 0.1 mM paraquat, 40 µM glucose, paraquat + cisplatin, glucose + cisplatin and H_2O as a vehicle. Performing a XF respirometer experiment with *C. elegans* is a procedure that consists of six main steps:

Day 1

(a) Pre-experimental procedures. Plates with special requirements were prepare freshly as indicated in **Materials and Methods 4**. Animals were synchronized and treated for each condition from L1 for 24 hours at 20ºC.

Day 2

(b) Preparing the XF respirometer. Seahorse XFe96 Analyzer and the software were launched, and the heater was turned at the desired temperature (24ºC). XFe template was designed as Koopman et al. indicates. Probes were hydrated with 200 µL Seahorse XF Calibrant Solution (Agilent) and incubated overnight at 37ºC in a non-CO_2 incubator.

Day 3

(c) Loading compounds and calibration. Drug stock and working solutions were prepared, and working solutions were loaded to ports A and B, as described in Koopman et al., and incubated for 10 minutes at RT. After drug incubation, calibration of the utility plate was run while worms were collected and loading to the cell culture plate.

(d) Collecting and loading worm samples. Worms were collected at L3 stage and washed, with M9 solution, at least 3 times in 14 mL conical tubes. Wash steps took at least 30 minutes to stimulate the elimination of food and compounds from the cuticle and gut. Once finished, worm concentration was calculated by manual counting to reach 2 worms per µL, approximately. 180 µL M9 solution was added to all the cell culture plate wells except for background wells, in which 200 µL were plated. 20 µL from each worm solution were loaded to the wells and 6 replicates for each condition were prepared.

(e) XFe experiment. When calibration ends, cell culture plate containing the samples were replaced by the utility plate and XFe procedure starts.

(f) Post-experimental data analysis. The number of animals were manual counted in a stereomicroscope for each well. Total OCR per well was normalized by the exact number of animals in the Seahorse Wave Desktop software. Wells with atypical worm concentration were eliminated prior to calculate

the median OCR for each condition. Graphpad Prism 8 was used to plot the data and for statistical analysis.

11. Lifespan assay

Lifespan experiments were performed at 15ºC and 20ºC. Synchronized L1 animals were plated on NGM OP50 feeding plates (day 1). Animals were transferred to a new plate every second day and, once they stopped producing offspring, every few days. Animals were checked every day and classified as dead when they failed to respond to gentle touch with a platinum pick. Animals that crawled off the plate, died from an extruded gonad or had internally hatched offspring were censored at the time of their death. Survival assay was repeated three times at 15ºC and once at 20ºC. Log-rank (Mantel-Cox) test with GraphPad Prism 8 was used to calculate p-values between strains.

12. Quantitative Real-Time PCR

For RNA extraction synchronized animals were collected, at different timepoints for experiment A and at young adult for experiment B and washed at least three times. Two different strategies were followed for experiments A and B:

Experiment A: *ubh-4* transcript levels in N2, *ubh-4(cer27)* and *ubh-4(cer25).* Total RNA was extracted using innuPREP RNA Mini Kit 2.0 (Analytic Jena). RT-PCR was done using a Maxima First Strand cDNA Synthesis Kit for RT-qPCR (Fermentas).

Quantitative real-time PCR was done using Maxima SYBR Green/ROX qPCR Master Mix (Fermentas) and LightCycler 480 (Roche) quantitative PCR machine. 1 µl cDNA was used as a template for sqRT-PCR amplification using the primers listed in **Table 12**. At least one of the pair of primers were designed to anneal in an exon-exon junction. Finally, qPCR data were normalized to the geometric mean of reference gene mRNA concentrations (*act-1, cdc-42* and *pmp-3*).

Experiment B: *comt-1*, *comt-2, comt-3*, *comt-4* and *comt-5* transcript levels in N2(WT) animals. *gst-4*, *egl-1* and F27C1.2 were used as positive control genes.Total RNA was extracted using TRI Reagent, followed by phase separation using 1-Bromo-3-chloropropane, and RNA was precipitated with 2 propanol. After treatment with DNase I (Thermo Fisher Scientific), cDNA was synthetized with the H Minus First Strand cDNA Synthesis Kit (Thermo Fisher Scientific). 1 µl cDNA was used as a template for sqRT-PCR amplification using the primers listed in **Table 12**. At least one of the pair of primers were designed to anneal in an exon-exon junction. Finally, qPCR data were normalized to the geometric mean of reference gene mRNA concentrations (*act-1* and *tbb-2*).

Table 12: Primers used for qPCR.

Gene	Primer Fwd	Primer Rev
ubh-4	CCACTGCAACAAAGCTGAC	CAAAAACAATCAAGAACCC
comt-1	GGCTGTAATAAGCTCAACCG	GCTCAGATGGAAGCTCTG
comt-2	CTCAGAGCACACCACTATCG	CGAAGGATCTGATGAAGTTCTGGC
comt-3	CGGAGTTCCGATCATCTCG	GAGCAGAATAGGTACGGTCATCC
comt-4	CCATGCCAATTATCGCAAG	GTTTGTCTAGACTCTCAACCC
comt-5	CCAATTATCACAAGTTCGGAG	CGGCAATCAGTTTGTCTAAAC
gst-4	AGCCAACGACTCCATTTGGC	GAATCAGCGTAAGCTTCTTCCTC
egl-1	ATGCTGATGCTCACCTTTGCC	TGAGACGAGGAGTAGAACATG
F27C1.2	AGAGTGCTTACGCACAAGCTGC	GTGATCCATGAGACGAATGTTC
act-1	CCAGGAATTGCTGATCGTATGCAGAA	TGGAGAGGGAAGCGAGGATAGA
tbb-2	TATGTGCCACGCGCCGTGTT	TTTCCGGCTCCGCTTTGTCCG
cdc-42	CTGCTGGACAGGAAGATTACG	CTCGGACATTCTCGAATGAAG
pmp-3	GTTCCCGTGTTCATCACTCAT	ACACCGTCGAGAAGCTGTAGA

13. DIC and fluorescence microscopy

Worms were anesthetized in 10 mM tetramisole hydrochloride and were mounted on 2% agar pads. Images were acquired in a ZEISS Axio Observer Z1 inverted fluorescence microscope and were processed with ZEISS ZEN 2012 (blue edition) software and Fiji.

14. Gonad dissection and DAPI stainning

Animals were anesthetized with 0.33 mM tetramisole hydrochloride and their heads cut using a pair of 25-gauge needles to extrude gonad arms. Gonads were fixed in 4% paraformaldehyde in PBS for 20-30 minutes and washed with PBS-T for 10 minutes. After 3 washes, gonads were

transferred directly to a microscope slide and mounted using 10 µl DAPI Fluoromount-G® (SouthernBiotech).

15. HSP-6p::GFP imaging and fluorescence quantification

L1 synchronized animals were grown in NGM plates with OP50 until young adult and treated from this stage with 100 ug/mL cisplatin. Pictures were taken the day after at 20X for all the conditions. Fluorescence were measured in ImageJ by measuring intensity of a determine area around the pharynx bulb.

16. Graph plotting and statistical analysis

All the data were graphically represented, and statistical analysis were performed using GraphPad Prism 8.0.

BIBLIOGRAPHY

Acosta-Alvear, D., Cho, M.Y., Wild, T., Buchholz, T.J., Lerner, A.G., Simakova, O., Hahn, J., Korde, N., Landgren, O., Maric, I., et al. (2015). Paradoxical resistance of multiple myeloma to proteasome inhibitors by decreased levels of 19S proteasomal subunits. Elife *4*, e08153.

Adamo, A., Montemauri, P., Silva, N., Ward, J.D., Boulton, S.J., and Volpe, A. La (2008). BRC-1 acts in the inter-sister pathway of meiotic double-strand break repair. EMBO Rep. *9*, 287–292.

Ahmed, Z.M., Masmoudi, S., Kalay, E., Belyantseva, I.A., Mosrati, M.A., Collin, R.W.J., Riazuddin, S., Hmani-Aifa, M., Venselaar, H., Kawar, M.N., et al. (2008). Mutations of LRTOMT, a fusion gene with alternative reading frames, cause nonsyndromic deafness in humans. Nat. Genet. *40*, 1335–1340.

Ahuja, J.S., Sandhu, R., Mainpal, R., Lawson, C., Henley, H., Hunt, P.A., Yanowitz, J.L., and Valentin Börner, G. (2017). Control of meiotic pairing and recombination by chromosomally tethered 26S proteasome. Science (80-.). *355*, 408–411.

Alcántar-Fernández, J., Navarro, R.E., Salazar-Martínez, A.M., Pérez-Andrade, M.E., and Miranda-Ríos, J. (2018). Caenorhabditis elegans respond to high-glucose diets through a network of stress-responsive transcription factors. PLoS One *13*.

Alcántar-Fernández, J., González-Maciel, A., Reynoso-Robles, R., Pérez Andrade, M.E., Hernández-Vázquez, A. de J., Velázquez-Arellano, A., and Miranda-Ríos, J. (2019). High-glucose diets induce mitochondrial dysfunction in Caenorhabditis elegans. PLoS One *14*, e0226652.

Amable, L. (2016). Cisplatin resistance and opportunities for precision medicine. Pharmacol. Res. *106*, 27–36.

Arribere, J.A., Bell, R.T., Fu, B.X.H., Artiles, K.L., Hartman, P.S., and Fire, A.Z. (2014). Efficient marker-free recovery of custom genetic modifications with CRISPR/Cas9 in *Caenorhabditis elegans*. Genetics *198*, 837–846.

Ashburner, M., Ball, C.A., Blake, J.A., Botstein, D., Butler, H., Cherry, J.M., Davis, A.P., Dolinski, K., Dwight, S.S., Eppig, J.T., et al. (2000). Gene ontology: Tool for the unification of biology. Nat. Genet. *25*, 25–29.

Balasubramani, A., Larjo, A., Bassein, J.A., Chang, X., Hastie, R.B., Togher, S.M., Lähdesmäki, H., and Rao, A. (2015). Cancer-associated ASXL1 mutations may act as gain-of-function mutations of the ASXL1-BAP1 complex. Nat. Commun. *6*, 1–15.

Barré-Sinoussi, F., and Montagutelli, X. (2015). Animal models are essential to biological research: Issues and perspectives. Futur. Sci. OA *1*, 4–6.

Baughman, J.M., Rose, C.M., Kolumam, G., Webster, J.D., Wilkerson, E.M., Merrill, A.E., Rhoads, T.W., Noubade, R., Katavolos, P., Lesch, J., et al. (2016). NeuCode Proteomics Reveals Bap1 Regulation of Metabolism. Cell Rep. *16*, 583–595.

Bergamino, M., Rullan, A.J., Saigí, M., Peiró, I., Montanya, E., Palmero, R., Ruffinelli, J.C., Navarro, A., Arnaiz, M.D., Brao, I., et al. (2019). Fasting plasma glucose is an independent predictor of survival in patients with locally advanced non-small cell lung cancer treated with concurrent chemoradiotherapy. BMC

Cancer *19*.

Bhattacharya, S., Hanpude, P., and Maiti, T.K. (2015). Cancer associated missense mutations in BAP1 catalytic domain induce amyloidogenic aggregation: A new insight in enzymatic inactivation. Sci. Rep. *5*.

Bolotin, A., Quinquis, B., Sorokin, A., and Dusko Ehrlich, S. (2005). Clustered regularly interspaced short palindrome repeats (CRISPRs) have spacers of extrachromosomal origin. Microbiology *151*, 2551–2561.

Bott, M., Brevet, M., Taylor, B.S., Shimizu, S., Ito, T., Wang, L., Creaney, J., Lake, R.A., Zakowski, M.F., Reva, B., et al. (2011). The nuclear deubiquitinase BAP1 is commonly inactivated by somatic mutations and 3p21.1 losses in malignant pleural mesothelioma. Nat. Genet. *43*, 668–672.

Boulton, S.J., Martin, J.S., Polanowska, J., Hill, D.E., Gartner, A., and Vidal, M. (2004). BRCA1/BARD1 Orthologs Required for DNA Repair in Caenorhabditis elegans. Curr. Biol. *14*, 33–39.

Breier, A.F., Malhotra, A.K., Su, T.P., Pinals, D.A., Elman, I., Adler, C.M., Lafargue, R.T., Clifton, A., and Pickar, D. (1999). Clozapine and risperidone in chronic schizophrenia: Effects on symptoms, Parkinsonian side effects, and neuroendocrine response. Am. J. Psychiatry *156*, 294–298.

Brenner, S. (1974). The Genetics of Caenorhabditis elegans. Genetics *77*, 71–94.

Burger, J., Merlet, J., Tavernier, N., Richaudeau, B., Arnold, A., Ciosk, R., Bowerman, B., and Pintard, L. (2013). CRL2LRR-1 E3-Ligase Regulates Proliferation and Progression through Meiosis in the Caenorhabditis elegans Germline. PLoS Genet. *9*.

Burgie, S.E., Bingman, C.A., Soni, A.B., and Phillips, G.N. (2012). Structural characterization of human Uch37. Proteins Struct. Funct. Bioinforma. *80*, 649–654.

Camacho, C., Coulouris, G., Avagyan, V., Ma, N., Papadopoulos, J., Bealer, K., and Madden, T.L. (2009). BLAST+: architecture and applications.

Carbone, M., Yang, H., Pass, H.I., Krausz, T., Testa, J.R., and Gaudino, G. (2013). BAP1 and cancer. Nat. Rev. Cancer *13*, 153–159.

Cerami, E., Gao, J., Dogrusoz, U., Gross, B.E., Sumer, S.O., Aksoy, B.A., Jacobsen, A., Byrne, C.J., Heuer, M.L., Larsson, E., et al. (2012). The cBio Cancer Genomics Portal: An open platform for exploring multidimensional cancer genomics data. Cancer Discov. *2*, 401–404.

Chase, D.L., and Koelle, M.R. (2007). Biogenic amine neurotransmitters in C. elegans. WormBook 1–15.

Chen, H.H.W., and Kuo, M.T. (2010). Role of Glutathione in the Regulation of Cisplatin Resistance in Cancer Chemotherapy. *2010*.

Choi, Y.M., Kim, H.K., Shim, W., Anwar, M.A., Kwon, J.W., Kwon, H.K., Kim, H.J., Jeong, H., Kim, H.M., Hwang, D., et al. (2015). Mechanism of cisplatin-induced cytotoxicity is correlated to impaired metabolism due to mitochondrial ROS generation. PLoS One *10*.

Chondrogianni, N., Sakellari, M., Lefaki, M., Papaevgeniou, N., and Gonos, E.S.

(2014). Proteasome activation delays aging in vitro and in vivo. Free Radic. Biol. Med. *71*, 303–320.

Cocetta, V., Ragazzi, E., and Montopoli, M. (2019). Mitochondrial involvement in cisplatin resistance. Int. J. Mol. Sci. *20*.

Cong, L., Ran, F.A., Cox, D., Lin, S., Barretto, R., Habib, N., Hsu, P.D., Wu, X., Jiang, W., Marraffini, L.A., et al. (2013). Multiplex genome engineering using CRISPR/Cas systems. Science (80-.). *339*, 819–823.

Cutts, A.J., Soond, S.M., Powell, S., and Chantry, A. (2011). Early phase TGFβ receptor signalling dynamics stabilised by the deubiquitinase UCH37 promotes cell migratory responses. Int. J. Biochem. Cell Biol. *43*, 604–612.

Daou, S., Hammond-Martel, I., Mashtalir, N., Barbour, H., Gagnon, J., Iannantuono, N.V.G., Nkwe, N. Sen, Motorina, A., Pak, H., Yu, H., et al. (2015). The BAP1/ASXL2 histone H2A deubiquitinase complex regulates cell proliferation and is disrupted in cancer. J. Biol. Chem. *290*, 28643–28663.

DeRenzo, C., Reese, K.J., and Seydoux, G. (2003). Exclusion of germ plasm proteins from somatic lineages by cullin-dependent degradation. Nature *424*, 685–689.

Dey, A., Seshasayee, D., Noubade, R., French, D.M., Liu, J., Chaurushiya, M.S., Kirkpatrick, D.S., Pham, V.C., Lill, J.R., Bakalarski, C.E., et al. (2012). Loss of the tumor suppressor BAP1 causes myeloid transformation. Science (80-.). *337*, 1541–1546.

Donna L. Mallery, Cassandra J. Vandenberg, K.H. Activation of the E3 ligase function of the BRCA1/BARD1 complex by polyubiquitin chains.

Du, X., Schwander, M., Moresco, E.M.Y., Viviani, P., Haller, C., Hildebrand, M.S., Pak, K., Tarantino, L., Roberts, A., Richardson, H., et al. (2008). A catechol-O-methyltransferase that is essential for auditory function in mice and humans. Proc. Natl. Acad. Sci. U. S. A. *105*, 14609–14614.

Duman, D., Sirmaci, A., Cengiz, F.B., Ozdag, H., and Tekin, M. (2011). Screening of 38 Genes Identifies Mutations in 62% of Families with Nonsyndromic Deafness in Turkey. Genet. Test. Mol. Biomarkers *15*, 29–33.

Fang, Y., and Shen, X. (2017). Ubiquitin carboxyl-terminal hydrolases: involvement in cancer progression and clinical implications. Cancer Metastasis Rev. *36*, 669–682.

Fang, Y., Fu, D., and Shen, X.Z. (2010). The potential role of ubiquitin c-terminal hydrolases in oncogenesis. Biochim. Biophys. Acta - Rev. Cancer *1806*, 1–6.

Fire, A., Xu, S., Montgomery, M.K., Kostas, S.A., Driver, S.E., and Mello, C.C. (1998). Potent and specific genetic interference by double-stranded RNA in caenorhabditis elegans. Nature *391*, 806–811.

Forma, E., Jóźwiak, P., Bryś, M., and Krześlak, A. (2014). The potential role of O-GlcNAc modification in cancer epigenetics. Cell. Mol. Biol. Lett. *19*, 438–460.

Friedland, A.E., Tzur, Y.B., Esvelt, K.M., Colaiácovo, M.P., Church, G.M., and Calarco, J.A. (2013). Heritable genome editing in *C. elegans* via a CRISPR-Cas9 system. Nat. Methods *10*, 741–743.

Gems, D., and Partridge, L. (2008). Stress-Response Hormesis and Aging: “That which Does Not Kill Us Makes Us Stronger.” Cell Metab. *7*, 200–203.

Glennon, J., Wadman, W., McCreary, A., and Werkman, T. (2008). Dopamine Receptor Pharmacology: Interactions with Serotonin Receptors and Significance for the Aetiology and Treatment of Schizophrenia. CNS Neurol. Disord. - Drug Targets *5*, 3–23.

Green, R.A., Kao, H.L., Audhya, A., Arur, S., Mayers, J.R., Fridolfsson, H.N., Schulman, M., Schloissnig, S., Niessen, S., Laband, K., et al. (2011). A high-resolution C. elegans essential gene network based on phenotypic profiling of a complex tissue. Cell *145*, 470–482.

Grigoreva, T.A., Tribulovich, V.G., Garabadzhiu, A. V, Melino, G., and Barlev, N.A. The 26S proteasome is a multifaceted target for anti-cancer therapies.

Hamer, G., Matilainen, O., and Holmberg, C.I. (2010). A photoconvertible reporter of the ubiquitin-proteasome system in vivo. Nat. Methods *7*, 473–478.

Hanpude, P., Bhattacharya, S., Singh, A.K., and Maiti, T.K. (2017). Ubiquitin Recognition of BAP1: Understanding its Enzymatic Function. Biosci. Rep. BSR20171099.

Harbour, J.W., Onken, M.D., Roberson, E.D.O., Duan, S., Cao, L., Worley, L.A., Council, M.L., Matatall, K.A., Helms, C., and Bowcock, A.M. (2010). Frequent mutation of BAP1 in metastasizing uveal melanomas. Science (80-.). *330*, 1410–1413.

Hayashi, M., Chin, G.M., and Villeneuve, A.M. (2007). C. elegans Germ Cells Switch between Distinct Modes of Double-Strand Break Repair During Meiotic Prophase Progression. PLoS Genet. *3*, e191.

Heinz, A., and Schlagenhauf, F. (2010). Dopaminergic dysfunction in schizophrenia: salience attribution revisited. Schizophr. Bull. *36*, 472–485.

Hengartner, M.O., and Horvitz, H.R. (1994). Activation of C. elegans cell death protein CED-9 by an ammo-acid substitution in a domain conserved in Bcl-2. Nature *369*, 318–320.

Honnen, S. (2017). Caenorhabditis elegans as a powerful alternative model organism to promote research in genetic toxicology and biomedicine. Arch. Toxicol. *91*, 2029–2044.

Hu, Y., Wu, Y., Li, Q., Zhang, W., and Jin, C. (2015a). Solution Structure of Yeast Rpn9. J. Biol. Chem. *290*, 6878–6889.

Hu, Y., Wu, Y., Li, Q., Zhang, W., and Jin, C. (2015b). Solution structure of yeast Rpn9: Insights into proteasome lid assembly. J. Biol. Chem. *290*, 6878–6889.

Huang, H., Liu, N., Liao, Y., Liu, N., Cai, J., Xia, X., Guo, Z., Li, Y., Wen, Q., Yin, Q., et al. (2017). Platinum-containing compound platinum pyrithione suppresses ovarian tumor proliferation through proteasome inhibition. J. Exp. Clin. Cancer Res. *36*, 79.

Hutter, H., and Suh, J. (2016). GExplore 1.4: An expanded web interface for queries on Caenorhabditis elegans protein and gene function . Worm *5*, e1234659.

Inapurapu, S., Kudle, K.R., Bodiga, S., and Bodiga, V.L. (2017). Cisplatin cytotoxicity is dependent on mitochondrial respiration in Saccharomyces cerevisiae. Iran. J. Basic Med. Sci. *20*, 83–89.

Ishino, Y., Shinagawa, H., Makino, K., Amemura, M., and Nakatura, A. (1987). Nucleotide sequence of the iap gene, responsible for alkaline phosphatase isoenzyme conversion in Escherichia coli, and identification of the gene product. J. Bacteriol. *169*, 5429–5433.

Ismail, I.H., Davidson, R., Gagné, J.P., Xu, Z.Z., Poirier, G.G., and Hendzel, M.J. (2014). Germline mutations in BAP1 impair its function in DNA double-strand break repair. Cancer Res. *74*, 4282–4294.

Isono, E., Saeki, Y., Yokosawa, H., and Toh-E, A. (2004). Rpn7 Is required for the structural integrity of the 26 S proteasome of Saccharomyces cerevisiae. J. Biol. Chem. *279*, 27168–27176.

Jagasia, R., Grote, P., Westermann, B., and Conradt, B. (2005). DRP-1-mediated mitochondrial fragmentation during EGL-1-induced cell death in C. elegans. Nature *433*, 754–760.

Janisiw, E., Dello Stritto, M.R., Jantsch, V., and Silva, N. (2018). BRCA1-BARD1 associate with the synaptonemal complex and pro-crossover factors and influence RAD-51 dynamics during Caenorhabditis elegans meiosis. PLOS Genet. *14*, e1007653.

Javer, A., Currie, M., Lee, C.W., Hokanson, J., Li, K., Martineau, C.N., Yemini, E., Grundy, L.J., Li, C., Ch'ng, Q.L., et al. (2018a). An open-source platform for analyzing and sharing worm-behavior data. Nat. Methods *15*, 645–646.

Javer, A., Ripoll-Sánchez, L., and Brown, A.E.X. (2018b). Powerful and interpretable behavioral features for quantitative phenotyping of *Caenorhabditis elegans*. Philos. Trans. R. Soc. B Biol. Sci. *373*, 20170375.

Jemal, A., Siegel, R., Ward, E., and Hao, Y. (2008). Cancer Statistics , 2008. *58*, 71–96.

Jensen, D.E., Proctor, M., Marquis, S.T., Gardner, H.P., Ha, S.I., Chodosh, L.A., Ishov, A.M., Tommerup, N., Vissing, H., Sekido, Y., et al. (1998). BAP1: A novel ubiquitin hydrolase which binds to the BRCA1 RING finger and enhances BRCA1-mediated cell growth suppression. Oncogene *16*, 1097–1112.

Jiao, L., Ouyang, S., Shaw, N., Song, G., Feng, Y., Niu, F., Qiu, W., Zhu, H., Hung, L.W., Zuo, X., et al. (2014). Mechanism of the Rpn13-induced activation of Uch37. Protein Cell *5*, 616–630.

Jovaisaite, V., Mouchiroud, L., and Auwerx, J. (2014). The mitochondrial unfolded protein response, a conserved stress response pathway with implications in health and disease. J. Exp. Biol. *217*, 137–143.

Kaletta, T., and Hengartner, M.O. (2006). Finding function in novel targets: C. elegans as a model organism. Nat. Rev. Drug Discov. *5*, 387–399.

Kamath, R.S., Fraser, A.G., Dong, Y., Poulin, G., Durbin, R., Gotta, M., Kanapin, A., Le Bot, N., Moreno, S., Sohrmann, M., et al. (2003). Systematic functional analysis of the Caenorhabditis elegans genome using RNAi. Nature *421*, 231–237.

Kanehisa, M. (2019). Toward understanding the origin and evolution of cellular organisms. Protein Sci. *28*, 1947–1951.

Kanehisa, M., and Goto, S. (2000). KEGG: kyoto encyclopedia of genes and genomes - Release 72.1, December 1, 2014 . Nucleic Acids Res *28*, 27–30.

Kanehisa, M., Sato, Y., Furumichi, M., Morishima, K., and Tanabe, M. (2019). New approach for understanding genome variations in KEGG. Nucleic Acids Res. *47*, D590–D595.

Kato, S., Tomson, B.N., Buys, T.P.H., Elkin, S.K., Carter, J.L., and Kurzrock, R. (2016). Genomic landscape of malignant mesotheliomas. Mol. Cancer Ther. *15*, 2498–2507.

Kelland, L. (2007). The resurgence of platinum-based cancer chemotherapy. Nat. Rev. Cancer *7*, 573–584.

Kim, H., Ishidate, T., Ghanta, K.S., Seth, M., Conte, D., Shirayama, M., and Mello, C.C. (2014). A co-CRISPR strategy for efficient genome editing in Caenorhabditis elegans. Genetics *197*, 1069–1080.

Konstantinova, I.M., Tsimokha, A.S., and Mittenberg, A.G. (2008). Role of Proteasomes in Cellular Regulation. Int. Rev. Cell Mol. Biol. *267*, 59–124.

Koopman, M., Michels, H., Dancy, B.M., Kamble, R., Mouchiroud, L., Auwerx, J., Nollen, E.A.A., and Houtkooper, R.H. (2016). A screening-based platform for the assessment of cellular respiration in Caenorhabditis elegans. Nat. Protoc. *11*, 1798–1816.

Koopman, R., Schaart, G., and Hesselink, M.K. (2001). Optimisation of oil red O staining permits combination with immunofluorescence and automated quantification of lipids. Histochem. Cell Biol. *116*, 63–68.

Kumar, G.A., and Subramaniam, K. (2018). PUF-8 facilitates homologous chromosome pairing by promoting proteasome activity during meiotic entry in C. elegans. Dev. *145*.

Kunert, J.M., Maia, P.D., and Kutz, J.N. (2017). Functionality and Robustness of Injured Connectomic Dynamics in C. elegans: Linking Behavioral Deficits to Neural Circuit Damage. PLoS Comput. Biol. *13*, 1–21.

Kuwabara, P.E., and O'Neil, N. (2001). The use of functional genomics in C. elegans for studying human development and disease. J. Inherit. Metab. Dis. *24*, 127–138.

Lai, C.H., Chou, C.Y., Ch'ang, L.Y., Liu, C.S., and Lin, W.C. (2000). Identification of novel human genes evolutionarily conserved in Caenorhabditis elegans by comparative proteomics. Genome Res. *10*, 703–713.

Li, Q., Saito, T.T., Martinez-Garcia, M., Deshong, A.J., Nadarajan, S., Lawrence, K.S., Checchi, P.M., Colaiacovo, M.P., and Engebrecht, J.A. (2018). The tumor suppressor BRCA1-BARD1 complex localizes to the synaptonemal complex and regulates recombination under meiotic dysfunction in Caenorhabditis elegans. PLoS Genet. *14*, e1007701.

Liang, B., Ferguson, K., Kadyk, L., and Watts, J.L. (2010). The role of nuclear receptor NHR-64 in fat storage regulation in caenorhabditis elegans. PLoS One *5*.

Luchini, C., Veronese, N., Yachida, S., Cheng, L., Nottegar, A., Stubbs, B., Solmi, M., Capelli, P., Pea, A., Barbareschi, M., et al. (2016). Different prognostic roles of tumor suppressor gene *BAP1* in cancer: A systematic review with meta-analysis. Genes, Chromosom. Cancer *55*, 741–749.

Luz, A.L., Rooney, J.P., Kubik, L.L., Gonzalez, C.P., Song, D.H., and Meyer, J.N. (2015). Mitochondrial morphology and fundamental parameters of the mitochondrial respiratory chain are altered in caenorhabditis elegans strains deficient in mitochondrial dynamics and homeostasis processes. PLoS One *10*, 1–23.

MacDonald, L.D., Knox, A., and Hansen, D. (2008). Proteasomal regulation of the proliferation vs. meiotic entry decision in the Caenorhabditis elegans germ line. Genetics *180*, 905–920.

MacQueen, A.J., Phillips, C.M., Bhalla, N., Weiser, P., Villeneuve, A.M., and Dernburg, A.F. (2005). Chromosome sites play dual roles to establish homologous synapsis during meiosis in C. elegans. Cell *123*, 1037–1050.

Makarova, K.S., Wolf, Y.I., Alkhnbashi, O.S., Costa, F., Shah, S.A., Saunders, S.J., Barrangou, R., Brouns, S.J.J., Charpentier, E., Haft, D.H., et al. (2015). An updated evolutionary classification of CRISPR-Cas systems. Nat. Rev. Microbiol. *13*, 722–736.

Mali, P., Yang, L., Esvelt, K.M., Aach, J., Guell, M., DiCarlo, J.E., Norville, J.E., and Church, G.M. (2013). RNA-guided human genome engineering via Cas9. Science (80-.). *339*, 823–826.

Maluccio, M., Einhorn, L.H., and Goulet, R.J. (2007). Surgical therapy for testicular cancer metastatic to the liver. 199–200.

Manasanch, E.E., and Orlowski, R.Z. (2017). Proteasome inhibitors in cancer therapy. Nat. Rev. Clin. Oncol. *14*, 417–433.

Marshall, R.S., and Vierstra, R.D. (2019). Dynamic regulation of the 26S proteasome: From synthesis to degradation. Front. Mol. Biosci. *6*, 40.

Marshall, R.S., Li, F., Gemperline, D.C., Book, A.J., and Vierstra, R.D. (2015). Autophagic Degradation of the 26S Proteasome Is Mediated by the Dual ATG8/Ubiquitin Receptor RPN10 in Arabidopsis. Mol. Cell *58*, 1053–1066.

Masoomian, B., Shields, J.A., and Shields, C.L. (2018). Overview of BAP1 cancer predisposition syndrome and the relationship to uveal melanoma. J. Curr. Ophthalmol. *30*, 102–109.

Matilainen, O., Arpalahti, L., Rantanen, V., Hautaniemi, S., and Holmberg, C.I. (2013). Insulin/IGF-1 Signaling Regulates Proteasome Activity through the Deubiquitinating Enzyme UBH-4. Cell Rep. *3*, 1980–1995.

Maurer, K.J., and Quimby, F.W. (2015). chapter 34 - Animal Models in Biomedical Research (Elsevier Inc.).

Meiser, J., Weindl, D., and Hiller, K. (2013). Complexity of dopamine metabolism. Cell Commun. Signal. *11*, 1–18.

Misaghi, S., Ottosen, S., Izrael-Tomasevic, A., Arnott, D., Lamkanfi, M., Lee, J., Liu, J., O'Rourke, K., Dixit, V.M., and Wilson, A.C. (2009). Association of C-

terminal ubiquitin hydrolase BRCA1-associated protein 1 with cell cycle regulator host cell factor 1. Mol. Cell. Biol. *29*, 2181–2192.

Mohammad, A., Vanden Broek, K., Wang, C., Daryabeigi, A., Jantsch, V., Hansen, D., and Schedl, T. (2018). Initiation of meiotic development is controlled by three post-transcriptional pathways in caenorhabditis elegans. Genetics *209*, 1197–1224.

Mojica, F.J.M., and Montoliu, L. (2016). On the Origin of CRISPR-Cas Technology: From Prokaryotes to Mammals. Trends Microbiol. *24*, 811–820.

Mojica, F.J.M., Juez, G., and Rodriguez-Valera, F. (1993). Transcription at different salinities of Haloferax mediterranei sequences adjacent to partially modified PstI sites. Mol. Microbiol. *9*, 613–621.

Mojica, F.J.M., Díez-Villaseñor, C., García-Martínez, J., and Soria, E. (2005). Intervening sequences of regularly spaced prokaryotic repeats derive from foreign genetic elements. J. Mol. Evol. *60*, 174–182.

Mukherjea, D., and Rybak, L.P. (2011). Pharmacogenomics of cisplatin-induced ototoxicity. Pharmacogenomics *12*, 1039–1050.

Murali, R., Wiesner, T., and Scolyer, R.A. (2013). Tumours associated with BAP1 mutations. Pathology *45*, 116–126.

Nagashima, T., Oami, E., Kutsuna, N., Ishiura, S., and Suo, S. (2016). Dopamine regulates body size in Caenorhabditis elegans. Dev. Biol. *412*, 128–138.

Napolitano, A., Cesura, A.M., and Da Prada, M. (1995). The role of monoamine oxidase and catechol O-methyltransferase in dopaminergic neurotransmission. In Journal of Neural Transmission, Supplement, pp. 35–45.

Nass, R., and Blakely, R.D. (2003). THE CAENORHABDITIS ELEGANS DOPAMINERGIC SYSTEM : Opportunities for Insights into Dopamine Transport and Neurodegeneration. Annu. Rev. Pharmacol. Toxicol. *43*, 521–544.

Nass, R., Hall, D.H., Miller, D.M., and Blakely, R.D. (2002). Neurotoxin-induced degeneration of dopamine neurons in Caenorhabditis elegans. Proc. Natl. Acad. Sci. U. S. A. *99*, 3264–3269.

Nishikawa, H., Wu, W., Koike, A., Kojima, R., Gomi, H., Fukuda, M., and Ohta, T. (2009). BRCA1-associated protein 1 interferes with BRCA1/BARD1 RING heterodimer activity. Cancer Res. *69*, 111–119.

Nomura, T., Horikawa, M., Shimamura, S., Hashimoto, T., and Sakamoto, K. (2010). Fat accumulation in Caenorhabditis elegans is mediated by SREBP homolog SBP-1. Genes Nutr. *5*, 17–27.

O'Reilly, L.P., Luke, C.J., Perlmutter, D.H., Silverman, G.A., and Pak, S.C. (2014). C. elegans in high-throughput drug discovery. Adv. Drug Deliv. Rev. *69–70*, 247–253.

Olgun, Y., Aktaş, S., Altun, Z., Kırkım, G., Kızmazoğlu, D.Ç., Erçetin, A.P., Demir, B., İnce, D., Mutafoğlu, K., Demirağ, B., et al. (2016). Analysis of genetic and non genetic risk factors for cisplatin ototoxicity in pediatric patients. Int. J. Pediatr. Otorhinolaryngol. *90*, 64–69.

Omura, D.T., Clark, D.A., Samuel, A.D.T., and Horvitz, H.R. (2012). Dopamine

signaling is essential for precise rates of locomotion by C. elegans. PLoS One *7*, 38649.

Osuna-Luque, J., Rodríguez-Ramos, Á., Gámez-del-Estal, M. del M., and Ruiz-Rubio, M. (2018). Behavioral Mechanisms That Depend on Dopamine and Serotonin in *Caenorhabditis elegans* Interact With the Antipsychotics Risperidone and Aripiprazole. J. Exp. Neurosci. *12*, 117906951879862.

Papaevgeniou, N., and Chondrogianni, N. (2014). The ubiquitin proteasome system in Caenorhabditis elegans and its regulation. Redox Biol. *2*, 333–347.

Penkner, A., Tang, L., Novatchkova, M., Ladurner, M., Fridkin, A., Gruenbaum, Y., Schweizer, D., Loidl, J., and Jantsch, V. (2007). The Nuclear Envelope Protein Matefin/SUN-1 Is Required for Homologous Pairing in C. elegans Meiosis. Dev. Cell *12*, 873–885.

Perera, F.P. (1997). Environment and Cancer: Who Are Susceptible? Science (80). *278*, 1068–1073.

Phillips, C.M., and Dernburg, A.F. (2006). A Family of Zinc-Finger Proteins Is Required for Chromosome-Specific Pairing and Synapsis during Meiosis in C. elegans. Dev. Cell *11*, 817–829.

Phillips, C.M., McDonald, K.L., and Dernburg, A.F. (2009). Cytological analysis of meiosis in Caenorhabditis elegans. Methods Mol. Biol. *558*, 171–195.

Porta-de-la-Riva, M., Fontrodona, L., Villanueva, A., and Cerón, J. (2012). Basic Caenorhabditis elegans methods: Synchronization and observation. J. Vis. Exp. e4019.

Poulin, G., Nandakumar, R., and Ahringer, J. (2004). Genome-wide RNAi screens in Caenorhabditis elegans: Impact on cancer research. Oncogene *23*, 8340–8345.

Pourcel, C., Salvignol, G., and Vergnaud, G. (2005). CRISPR elements in Yersinia pestis acquire new repeats by preferential uptake of bacteriophage DNA, and provide additional tools for evolutionary studies. Microbiology *151*, 653–663.

Prasada Rao, H.B.D., Qiao, H., Bhatt, S.K., Bailey, L.R.J., Tran, H.D., Bourne, S.L., Qiu, W., Deshpande, A., Sharma, A.N., Beebout, C.J., et al. (2017). A SUMO-ubiquitin relay recruits proteasomes to chromosome axes to regulate meiotic recombination. Science (80-.). *355*, 403–407.

Pussegoda, K.A. (2010). Genetic variants associated with cisplatin-induced hearing loss. Clin. Genet. *78*, 33–35.

Remm, M., Storm, C.E.V., and Sonnhammer, E.L.L. (2001). Automatic clustering of orthologs and in-paralogs from pairwise species comparisons. J. Mol. Biol. *314*, 1041–1052.

Reyes-Turcu, F.E., Ventii, K.H., and Wilkinson, K.D. (2009). Regulation and Cellular Roles of Ubiquitin-Specific Deubiquitinating Enzymes. Annu. Rev. Biochem. *78*, 363–397.

De Rienzo, A., Archer, M.A., Yeap, B.Y., Dao, N., Sciaranghella, D., Sideris, A.C., Zheng, Y., Holman, A.G., Wang, Y.E., Dal Cin, P.S., et al. (2016). Gender-specific molecular and clinical features underlie malignant pleural mesothelioma. Cancer Res. *76*, 319–328.

Rodríguez-Ramos, Á., Gámez-del-Estal, M.M., Porta-de-la-Riva, M., Cerón, J., and Ruiz-Rubio, M. (2017b). Impaired Dopamine-Dependent Locomotory Behavior of C. elegans Neuroligin Mutants Depends on the Catechol-O-Methyltransferase COMT-4. Behav. Genet. *47*, 596–608.

Rolén, U., Kobzeva, V., Gasparjan, N., Ovaa, H., Winberg, G., Kisseljov, F., and Masucci, M.G. (2006). Activity profiling of deubiquitinating enzymes in cervical carcinoma biopsies and cell lines. Mol. Carcinog. *45*, 260–269.

Ross, C.J.D., Katzov-Eckert, H., Dubé, M.P., Brooks, B., Rassekh, S.R., Barhdadi, A., Feroz-Zada, Y., Visscher, H., Brown, A.M.K., Rieder, M.J., et al. (2009). Genetic variants in TPMT and COMT are associated with hearing loss in children receiving cisplatin chemotherapy. Nat. Genet. *41*, 1345–1349.

Rousseau, A., and Bertolotti, A. (2018). Regulation of proteasome assembly and activity in health and disease. Nat. Rev. Mol. Cell Biol. *19*, 697–712.

Rual, J.F., Ceron, J., Koreth, J., Hao, T., Nicot, A.S., Hirozane-Kishikawa, T., Vandenhaute, J., Orkin, S.H., Hill, D.E., van den Heuvel, S., et al. (2004). Toward improving Caenorhabditis elegans phenome mapping with an ORFeome-based RNAi library. Genome Res. *14*, 2162–2168.

Ruan, H. Bin, Han, X., Li, M.D., Singh, J.P., Qian, K., Azarhoush, S., Zhao, L., Bennett, A.M., Samuel, V.T., Wu, J., et al. (2012). O-GlcNAc transferase/host cell factor C1 complex regulates gluconeogenesis by modulating PGC-1α stability. Cell Metab. *16*, 226–237.

Sahtoe, D.D., vanDijk, W.J., ElOualid, F., Ekkebus, R., Ovaa, H., and Sixma, T.K. (2015). Mechanism of UCH-L5 Activation and Inhibition by DEUBAD Domains in RPN13 and INO80G. Mol. Cell *57*, 887–900.

Sanchez-Pulido, L., Kong, L., Ponting, C.P., and Valencia, A. (2012). A common ancestry for BAP1 and Uch37 regulators. Bioinforma. Discov. NOTE *28*, 1953–1956.

Sanford, C., and Perry, M.D. (2001). Asymmetrically distributed oligonucleotide repeats in the Caenorhabditis elegans genome sequence that map to regions important for meiotic chromosome segregation. Nucleic Acids Res. *29*, 2920–2926.

Sanyal, S., Wintle, R.F., Kindt, K.S., Nuttley, W.M., Arvan, R., Fitzmaurice, P., Bigras, E., Merzs, D.C., Hébert, T.E., Van Der Kooy, D., et al. (2004). Dopamine modulates the plasticity of mechanosensory responses in Caenorhabditis elegans. EMBO J. *23*, 473–482.

Sato, A., Isaac, B., Phillips, C.M., Rillo, R., Carlton, P.M., Wynne, D.J., Kasad, R.A., and Dernburg, A.F. (2009). Cytoskeletal Forces Span the Nuclear Envelope to Coordinate Meiotic Chromosome Pairing and Synapsis. Cell *139*, 907–919.

Sawin, E.R., Ranganathan, R., and Horvitz, H.R. (2000). C. elegans locomotory rate is modulated by the environment through a dopaminergic pathway and by experience through a serotonergic pathway. Neuron *26*, 619–631.

Schlotterer, A., Kukudov, G., Bozorgmehr, F., Hutter, H., Du, X., Oikonomou, D., Ibrahim, Y., Pfisterer, F., Rabbani, N., Thornalley, P., et al. (2009). C. elegans as model for the study of high glucose- mediated life span reduction. *58*.

Schreiber, F., Patricio, M., Muffato, M., Pignatelli, M., and Bateman, A. (2014). TreeFam v9: A new website, more species and orthology-on-the-fly.

Shimada, M., Kanematsu, K., Tanaka, K., Yokosawa, H., and Kawahara, H. (2006). Proteasomal ubiquitin receptor RPN-10 controls sex determination in Caenorhabditis elegans. Mol. Biol. Cell *17*, 5356–5371.

Shmakov, S., Smargon, A., Scott, D., Cox, D., Pyzocha, N., Yan, W., Abudayyeh, O.O., Gootenberg, J.S., Makarova, K.S., Wolf, Y.I., et al. (2017). Diversity and evolution of class 2 CRISPR-Cas systems. Nat. Rev. Microbiol. *15*, 169–182.

Shore, D.E., Carr, C.E., and Ruvkun, G. (2012). Induction of Cytoprotective Pathways Is Central to the Extension of Lifespan Conferred by Multiple Longevity Pathways. PLoS Genet. *8*, e1002792.

Silk, D.B.A. (1974). Peptide absorption in man. Gut *15*, 494–501.

Simmer, F., Moorman, C., Van Der Linden, A.M., Kuijk, E., Van Den Berghe, P.V.E., Kamath, R.S., Fraser, A.G., Ahringer, J., and Plasterk, R.H.A. (2003). Genome-wide RNAi of C. elegans using the hypersensitive rrf-3 strain reveals novel gene functions. PLoS Biol. *1*, E12.

Somlo, B.G., Doroshow, J.H., Lev-ran, A., Ahn, D.C., Hwang, L., Raschko, J.W., Forman, S.J., Margolin, K.A., Morgan, R.J., Leong, L.A., et al. (1995). Effect of low-dose prophylactic dopamine on high-dose cisplatin-induced electrolyte wasting, ototoxicity, and epidermal growth factor excretion: a randomized, placebo-controlled, double-blind trial. J. Clin. Oncol. *13*, 1231–1237.

Sonnhammer, E.L.L., and Durbin, R. (1997). Analysis of protein domain families in Caenorhabditis elegans. Genomics *46*, 200–216.

Soura, E., Eliades, P.J., Shannon, K., Stratigos, A.J., and Tsao, H. (2016). Hereditary melanoma: Update on syndromes and management Genetics of familial atypical multiple mole melanoma syndrome. J. Am. Acad. Dermatol. *74*, 411–420.

Stemmer, M., Thumberger, T., del Sol Keyer, M., Wittbrodt, J., and Mateo, J.L. (2015). CCTop: An Intuitive, Flexible and Reliable CRISPR/Cas9 Target Prediction Tool. PLoS One *10*, e0124633.

Stiernagle, T. (2006). Maintenance of C. elegans. WormBook 1–11.

De Strooper, B. (2010). Proteases and proteolysis in alzheimer disease: A multifactorial view on the disease process. Physiol. Rev. *90*, 465–494.

Szklarczyk, D., Gable, A.L., Lyon, D., Junge, A., Wyder, S., Huerta-Cepas, J., Simonovic, M., Doncheva, N.T., Morris, J.H., Bork, P., et al. (2019). STRING v11: Protein-protein association networks with increased coverage, supporting functional discovery in genome-wide experimental datasets. Nucleic Acids Res. *47*, D607–D613.

Takeuchi, J., Fujimuro, M., Yokosawa, H., Tanaka, K., and Toh-e, A. (1999). Rpn9 Is Required for Efficient Assembly of the Yeast 26S Proteasome. Mol. Cell. Biol. *19*, 6575–6584.

TANAKA, K. (2009). The proteasome: Overview of structure and functions. Proc. Japan Acad. Ser. B *85*, 12–36.

Teft, W.A., Winquist, E., Nichols, A.C., Kuruvilla, S., Richter, S., Parker, C., Francis, P., Trinnear, M., Lukovic, J., Bukhari, N., et al. (2019). Predictors of cisplatin-induced ototoxicity and survival in chemoradiation treated head and neck cancer patients. Oral Oncol. *89*, 72–78.

TENHUNEN, J., SALMINEN, M., LUNDSTRÖM, K., KIVILUOTO, T., SAVOLAINEN, R., and ULMANEN, I. (1994). Genomic organization of the human catechol O-methyltransferase gene and its expression from two distinct promoters. Eur. J. Biochem. *223*, 1049–1059.

Thiesen, S., Yin, P., Jorgensen, A.L., Zhang, J.E., Manzo, V., McEvoy, L., Barton, C., Picton, S., Bailey, S., Brock, P., et al. (2017). TPMT, COMT and ACYP2 genetic variants in paediatric cancer patients with cisplatin-induced ototoxicity. Pharmacogenet. Genomics *27*, 213–222.

Tolosa, E., Wenning, G., and Poewe, W. (2006). The diagnosis of Parkinson's disease. Lancet Neurol. *5*, 75–86.

Tripp, G., and Wickens, J. (2012). Reinforcement, Dopamine and Rodent Models in Drug Development for ADHD. Neurotherapeutics *9*, 622–634.

Tsang, W.Y., and Lemire, B.D. (2002). Mitochondrial genome content is regulated during nematode development. Biochem. Biophys. Res. Commun. *291*, 8–16.

Tsao, D., Wieskopf, J.S., Rashid, N., Sorge, R.E., Redler, R.L., Segall, S.K., Mogil, J.S., Maixner, W., Dokholyan, N. V., and Diatchenko, L. (2012). Serotonin-Induced Hypersensitivity via Inhibition of Catechol O-Methyltransferase Activity. Mol. Pain *8*, 25.

Ventii, K.H., Devi, N.S., Friedrich, K.L., Chernova, T.A., Meir, E.G. Van, and Wilkinson, K.D. (2008). BAP1 is a tumor suppressor that requires deubiquitinating activity and nuclear localization. *68*, 6953–6962.

Ventura, N., Rea, S.L., Schiavi, A., Torgovnick, A., Testi, R., and Johnson, T.E. (2009). p53/CEP-1 increases or decreases lifespan, depending on level of mitochondrial bioenergetic stress. Aging Cell *8*, 380–393.

Vicencio, J., Martínez-Fernández, C., Serrat, X., and Cerón, J. (2019). Efficient generation of endogenous fluorescent reporters by nested CRISPR in caenorhabditis elegans. Genetics *211*, 1143–1154.

Vidal-Gade, A., Topper, S., Young, L., Crisp, A., Kressin, L., Elbel, E., Maples, T., Brauner, M., Erbguth, K., Axelrod, A., et al. (2011). Caenorhabditis elegans selects distinct crawling and swimming gaits via dopamine and serotonin. Proc. Natl. Acad. Sci. U. S. A. *108*, 17504–17509.

Vilchez, D., Saez, I., and Dillin, A. (2014). The role of protein clearance mechanisms in organismal ageing and age-related diseases. Nat. Commun. *5*, 1–13.

Wadt, K., Choi, J., Chung, J.Y., Kiilgaard, J., Heegaard, S., Drzewiecki, K.T., Trent, J.M., Hewitt, S.M., Hayward, N.K., Gerdes, A.M., et al. (2012). A cryptic BAP1 splice mutation in a family with uveal and cutaneous melanoma, and paraganglioma. Pigment Cell Melanoma Res. *25*, 815–818.

Walerych, D., Lisek, K., Sommaggio, R., Piazza, S., Ciani, Y., Dalla, E., Rajkowska, K., Gaweda-Walerych, K., Ingallina, E., Tonelli, C., et al. (2016).

Proteasome machinery is instrumental in a common gain-of-function program of the p53 missense mutants in cancer. Nat. Cell Biol. *18*, 897–909.

Wang, D., and Lippard, S.J. (2005). Cellular processing of platinum anticancer drugs. Nat. Rev. Drug Discov. *4*, 307–320.

Wang, A., Papneja, A., Hyrcza, M., Al-Habeeb, A., and Ghazarian, D. (2016). BAP1: Gene of the month. J. Clin. Pathol. *69*, 750–753.

Wang, J., Robida-Stubbs, S., Tullet, J.M.A., Rual, J.-F., Vidal, M., and Blackwell, T.K. (2010). RNAi Screening Implicates a SKN-1–Dependent Transcriptional Response in Stress Resistance and Longevity Deriving from Translation Inhibition. PLoS Genet. *6*, e1001048.

Weinshenker, D., Garriga, G., and Thomas, J.H. (1995). Genetic and pharmacological analysis of neurotransmitters controlling egg laying in C. elegans. J. Neurosci. *15*, 6975–6985.

White JG, Southgate E, Thomson JN, B.S. (1986). The structure of the nervous system of the nematode Caenorhabditis elegans. Philos. Trans. R. Soc. London. B, Biol. Sci. *314*, 1–340.

Wicks, S.J., Grocott, T., Haros, K., Maillard, M., Ten Dijke, P., and Chantry, A. (2006). Reversible ubiquitination regulates the Smad/TGF-β signalling pathway. Biochem. Soc. Trans. *34*, 761–763.

Xu, L., Wei, Y., Reboul, J., Vaglio, P., Shin, T.H., Vidal, M., Elledge, S.J., and Harper, J.W. (2003). BTB proteins are substrate-specific adaptors in an SCF-like modular ubiquitin ligase containing CUL-3. Nature *425*, 316–321.

Yang, J.J., Lim, J.Y., Huang, J., Bass, J., Wu, J., Evans, W.E., Pappo, A., Zuo, J., Relling, M. V, and Onar-thomas, A. (2014). The Role of Inherited TPMT and COMT Genetic Variation in Cisplatin-induced Ototoxicity in Children with Cancer. *94*, 1–16.

Yao, T., Song, L., Jin, J., Cai, Y., Takahashi, H., Swanson, S.K., Washburn, M.P., Florens, L., Conaway, R.C., Cohen, R.E., et al. Distinct Modes of Regulation of the Uch37 Deubiquitinating Enzyme in the Proteasome and in the Ino80 Chromatin Remodeling Complex.

Yao, T., Song, L., Xu, W., DeMartino, G.N., Florens, L., Swanson, S.K., Washburn, M.P., Conaway, R.C., Conaway, J.W., and Cohen, R.E. (2006). Proteasome recruitment and activation of the Uch37 deubiquitinating enzyme by Adrm1. Nat. Cell Biol. *8*, 994–1002.

Yee, C., Yang, W., and Hekimi, S. (2014). The intrinsic apoptosis pathway mediates the pro-longevity response to mitochondrial ROS in C elegans. Cell *157*, 897–909.

Yemini, E., Jucikas, T., Grundy, L.J., Brown, A.E.X., and Schafer, W.R. (2013). A database of Caenorhabditis elegans behavioral phenotypes. Nat. Methods *10*, 877–879.

Yen, H.C.S., Espiritu, C., and Chang, E.C. (2003). Rpn5 is a conserved proteasome subunit and required for proper proteasome localization and assembly. J. Biol. Chem. *278*, 30669–30676.

Zarrizi, R., Menard, J.A., Belting, M., and Massoumi, R. (2014). Deubiquitination of γ-tubulin by BAP1 prevents chromosome instability in breast cancer cells. Cancer Res. *74*, 6499–6508.

Zediak, V.P., and Berger, S.L. (2008). Hit and Run: Transient Deubiquitylase Activity in a Chromatin-Remodeling Complex. Mol. Cell *31*, 773–774.

Zhang, H., and Sulzer, D. (2012). Regulation of striatal dopamine release by presynaptic auto- and heteroreceptors. Basal Ganglia *2*, 5–13.

Zhou, X., Edmonson, M.N., Wilkinson, M.R., Patel, A., Wu, G., Liu, Y., Li, Y., Zhang, Z., Rusch, M.C., Parker, M., et al. (2015). Exploring genomic alteration in pediatric cancer using ProteinPaint. Nat. Genet. *48*, 4–6.

LIST OF PUBLICATIONS

Vicencio, Jeremy*, **Carmen Martínez-Fernández***, Xènia Serrat*, and Julián Cerón. 2019. “Efficient Generation of Endogenous Fluorescent Reporters by Nested CRISPR in *Caenorhabditis elegans*.” Genetics 211(4):1143–54.
*These authors contributed equally to this work.

García-Rodríguez, Francisco Javier, **Carmen Martínez-Fernández**, David Brena, Dmytro Kukhtar, Xénia Serrat, Ernest Nadal, Mike Boxem, Sebastian Honnen, Antonio Miranda-Vizuete, Alberto Villanueva, and Julián Cerón. 2018. “Genetic and Cellular Sensitivity of *Caenorhabditis elegans* to the Chemotherapeutic Agent Cisplatin.” DMM Disease Models and Mechanisms 11(6).

Piulats, Josep M., August Vidal, Francisco J. García-Rodríguez, Clara Muñoz, Marga Nadal, Catia Moutinho, María Martínez-Iniesta, Josefina Mora, Agnes Figueras, Elisabet Guino, Laura Padulles, Alvaro Aytes, David G. Molleví, Sara Puertas, **Carmen Martínez-Fernandez**, Wilmar Castillo, Merce Juliachs, Victor Moreno, Purificacion Muñoz, Milica Stefanovic, Miguel A. Pujana, Enric Condom, Manel Esteller, Josep R. Germa, Gabriel Capella, Lourdes Farre, Albert Morales, Francesc Viñals, Xavier GarcíA-Del-Muro, Julian Ceron, and Alberto Villanueva. 2018. “Orthoxenografts of Testicular Germ Cell Tumors Demonstrate Genomic Changes Associated with Cisplatin Resistance and Identify PDMP as a Resensitizing Agent.” Clinical Cancer Research 24(15):3755–66.